FRAZER-NASH
CONSULTANCY
A KBR COMPANY

University of
Strathclyde
Glasgow

The Interaction of Structural Dynamics with the Orbital Mechanics of Solar Power Satellites

Final Report

March 2023

011336

54630R Issue 1

Prepared for: ESA

SYSTEMS • ENGINEERING • TECHNOLOGY

The Interaction of Structural Dynamics with the Orbital Mechanics of Solar Power Satellites

Final Report

Client: ESA

Client Ref.: 4000136011/21/NL/GLC/ov

Date: March 2023

Classification:

Project No.: 011336

Document No.: 54630R

Issue No.: 1

Compiled By: Mike Good and Simão da Graça Marto

Verified By: Mazen Aboushousha

Approved By: Alfie Vibert

Signed:

Distribution

Copy	Recipient	Organisation
1	Massimo Casasco	ESA
2	Laura Lottes	ESA
3	File	Frazer-Nash Consultancy Limited

Originating Office: FRAZER-NASH CONSULTANCY LIMITED
Hill Park South, Leatherhead, Surrey, KT22 7LH
Tel: 0333 032 9500

Contents

List of Figures

List of Tables

1 Introduction

1.1 Background

Space Based Solar Power concepts promise the generation of large amounts of renewable power by launching vast Solar Power Satellites (SPS) into space and beaming the power back to rectennas on Earth. Due to diffraction physics, large scale arrays delivering 2GW of power to the ground will be of the order of a kilometre in length and have masses of between 2,000 and 10,000 tonnes. There is significant and recently renewed interest in pursuing Space Based Solar Power (SBSP) technology, due to the need to decarbonise the energy supply to achieve Net Zero goals and a recent focus on achieving energy security. SBSP offers a number of potential advantages over the majority of terrestrial renewables, including high-capacity, dispatchable power that can be delivered across a large area.

The economics of SBSP is dominated by the launch costs and therefore there is an imperative to reduce the mass of the material transported into orbit. As such, it is likely that SPS will have sparse flexible structures. To design mass-optimised SPS it will be necessary to understand the requirements for the strength, stiffness and damping of their structures.

Given the size of SPS there is a potential for their structural dynamics to couple with their orbit mechanics, leading to the need for orbit correction. In addition to the scale of such structures there is also considerable challenge to be met in maintaining their shape and integrity when in orbit due to the tendency of any large orbiting structure to undergo various statically and dynamically induced deformations. This study, therefore seeks to investigate the magnitude of the coupling between the orbital mechanics and the structural dynamics of Solar Power Satellites and the insight gained will lead to the development of design guidance for optimising SPS structures.

This study has been conducted by Frazer-Nash Consultancy Limited working collaboratively with the University of Strathclyde. The study has been conducted on behalf of the European Space Agency (ESA) through the Open Space Innovation Platform (OSIP).

1.2 Project Scope

The objectives of this study are to:

- Investigate the magnitude of coupling between the structural dynamics and orbital mechanics of Solar Power Satellites;
- Quantify the potential disturbance to the orbit of Solar Power Satellites;
- Devise novel outline design guidelines for the structure of Solar Power Satellites to minimise the disturbance to their orbits;
- Identify trends in the structural response for a range of design parameters.

The first part of this study has considered the use of established finite element methods to quantify the structural response of a typical sparse flexible structure in the frequency domain. This follows a well-recognised analytical approach to determine the mode shapes and modal frequencies for an SPS structure. The key challenge being the analysis of such a vast spacecraft which lacks a traditional support frame/structure.

The second part of this activity has made use of a numerical perturbation analysis to investigate the effect of the

SPS structural dynamics on the orbital mechanics. This has been coupled with a ray tracing study, to assess the effectiveness of the deformed SPS structure.

The combination of these analytical methods has been instrumental in enhancing our understanding of the potential coupling between the structural response and orbital mechanics, and the impact this has on the design of such a SPS.

1.3 Project Structure

The project is structured as a number of discrete Work Packages (WPS), as follows:

- **Work Package 1: Structural Modelling** – Characterise the structure of the SPS and development of a Finite Element (FE) representation of the CASSIOPeiA SPS, which forms the basis of the study.
- **Work Package 2: Dynamic Structural Response** – Analysis of the FE model in the frequency domain to determine the fundamental low frequency modes of the SPS.
- **Work Package 3: Orbital Mechanics** – A review of the orbital mechanics for the SPS, focused on the excitation of modes and the interaction of the modes with the SPS orbital position and control.
- **Work Package 4: Design Requirements** – Draw together the over-arching conclusions from the study and outline a set of design requirements.

These linked work packages have been managed in a project workflow, as shown in Figure 1.1. This workflow progresses from the characterisation of the SPS structure and an understanding of the orbital loads to the development of two analytical tools. The benefit of these two toolsets is that they can be used to assess the response of the SPS, ranging from the vibration modes of the SPS, to the dynamic response of a structure that exhibits interactions between the structural dynamics and orbital mechanics. Together these analytical tools have been used to investigate the interaction between the orbital mechanics and structural dynamics of a SPS and derive a set of outline design requirements.

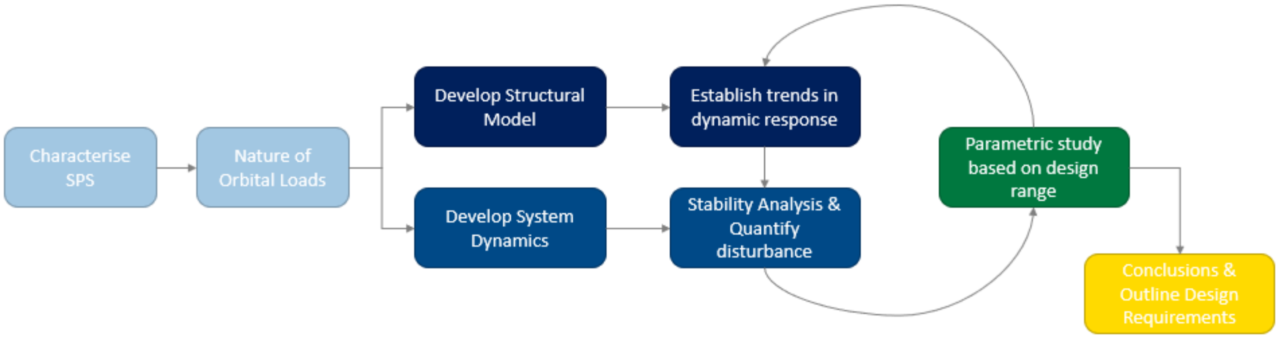

Figure 1.1: Project workflow.

The characterisation of the SPS concept used as the basis of this study is outlined in Section 2 of this report. The range of orbital loads considered are detailed in Section 3, whilst the attitude and orbital dynamics are detailed in Section 4. The development of the finite element and ray tracing analysis toolsets is outlined in Sections 5 and 6 respectively. The parametric study is outlined in Section 7 and the perturbation analysis is outlined in Section 8. Final conclusions from this study are presented in Section 9 and recommendations for future work are outlined in Section 10.

Appendix A outlines a range of definitions used throughout this report, including variables, reference frames, and a definition of the orbits considered for this work.

2 Characterisation of the Solar Power Satellite

2.1 CASSIOPeiA

The CASSIOPeiA SPS consists of a helical structure with high concentration solar Photovoltaic (PV) panels orientated to face solar North and South. These panels collect light reflected by large reflectors positioned at either end of the structure. The design uses an integrated sandwich panel which incorporates the photovoltaic and microwave elements forming an orientable phased array into a single element. This phased array allows the microwave beam to be steered through $360°$ resulting in a design where the mirrors can be orientated to face the Sun at all times and allow the beam to rotate to target rectennas on the ground. A key feature of the CASSIOPeiA design is that it seeks to utilise as much solid-state functionality as possible to eliminate moving parts and increase reliability.

There are three main configurations of CASSIOPeiA, which are illustrated in Figure 2.1. The main differences between these configurations are the size, number and position of the reflectors.

For the purpose of this study, we focus on the 2GW "2 Sun" variant of the system operating in geostationary orbit. The other variants of CASSIOPeiA operate in a highly elliptical orbit and will be discussed, but are not the primary focus of the project.

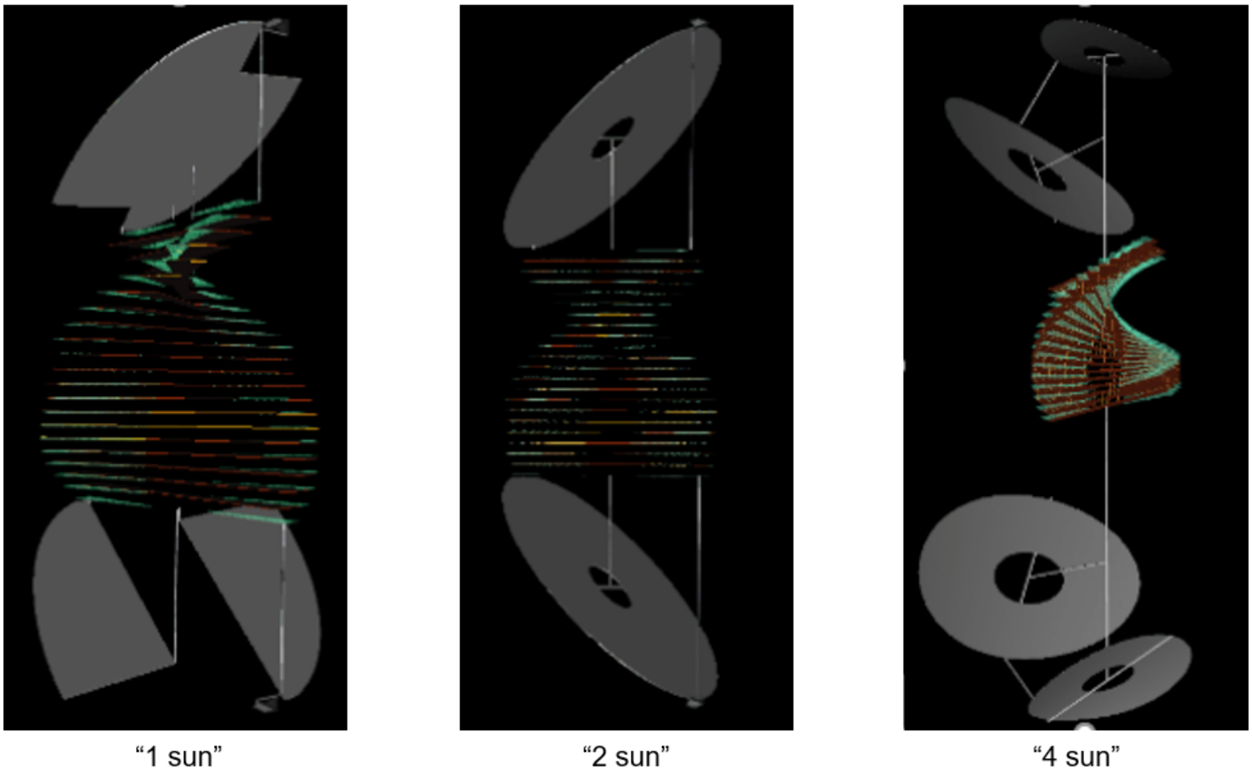
“1 sun” “2 sun” “4 sun”

Figure 2.1: Possible configurations of the CASSOPeiA design

The known aspects of the design are illustrated in Figure 2.2. These are:

- Two solar reflectors, angled at $45°$ to the incident sunlight

- A stepped helix of PV panels which comprises multiple layers of Solar PV panels (see inset of Figure 2.2), rotated relative to one another to form the “steps” of the stepped helical shape
- The microwave antennae span the gap between (and are orthogonal to) the layers of PV panels (as shown in Figure 2.2)

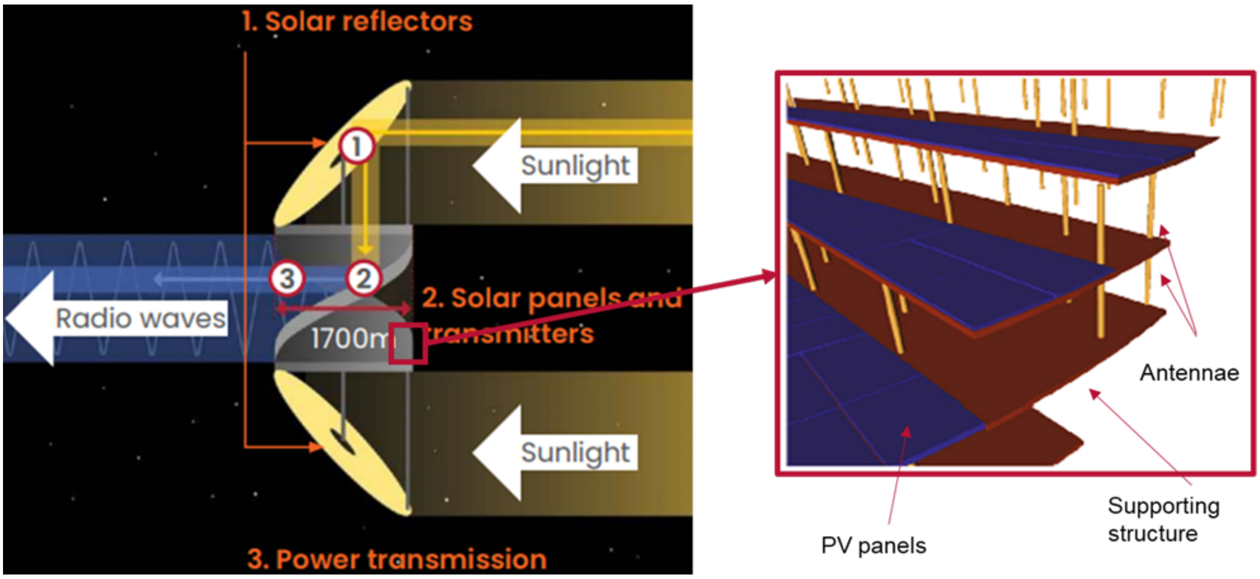

Figure 2.2: Overview of CASSIOPeiA design

This arrangement allows the CASSIOPeiA design to operate as follows:

- Solar reflectors are used to direct sunlight onto the layers of solar panels. For each reflector, the projected area of the solar panels is equal to the area of a circle with the same diameter as the helix.
- The energy received by the PV panels is transmitted to a rectenna on Earth as radio waves.
- Each antenna comprises three separate dipole elements. The direction of the radio waves emitted from each antenna can be controlled electronically by controlling the relative magnitudes and phase of the current in each of the dipoles. This neatly solves the “angular mismatch” problem which faces all SPS concepts (i.e. the idea that the structure must have separate Sun-pointing and ground-pointing components, which need to rotate relative to one another), and therefore enables the design to be “solid state”.

The helical shape means that all PV panels participate in receiving insolation, and all antennae participate in transmitting the energy to the rectenna.

2.2 Definition of the SPS

Much of the CASSIOPeiA research to date has focussed on the overall geometry, the distribution of PV panels, antennae and reflectors, the infrastructure required on the Earth, and estimates of yield. There is very little information available that describes the supporting structures and, as such, no detailed drawings or CAD upon which to base the FE model.

The following sections outline what is known about the structural aspects of the design (particularly stiffness and mass) from [4] and [5].

2.2.0.1 Helix

Based on previous discussions between Frazer-Nash and International Electric Company Limited (IECL) [4], it is understood that the helix has a diameter of approximately 2km.

The dimensions of the helix layers (width and separation) are understood to be of the order of the wavelength of the radio waves transmitted by the antennae. The assumed transmission frequency of 2.45 GHz gives a wavelength of approximately 120mm. As such, the dimensions of the helix layers are assumed to be of the order of 100mm. The number of layers is therefore likely to be of the order of 10,000.

The extent of any supporting structure for the helix is largely unknown. The following information has been gathered during discussions between Frazer-Nash Consultancy and IECL [4]:

- The helix is likely to be constructed from horizontal layers of Kapton film separated by vertical walls (also made of Kapton film), to provide a self-supporting microwave transparent structure. This structure will support a large number of additional discrete components (PV panels, antennae, etc.).
- The total mass of the helix is expected to be approximately 1500 tonnes.

Due to a lack of structural design maturity it has been assumed that the antennae, which span the gaps between layers of the helix, are not structural components.

2.2.0.2 Solar Reflectors

The solar reflectors are assumed to be elliptical in shape with a minor axis dimension of approximately 2km (i.e. the diameter of the helix) and major axis dimension of 2.8km (i.e 2km x $\sqrt{2}$km). These are angled at $45°$ to the incident sunlight [4].

Images of the design appear to show a hole in the centre of each reflector and it has been assumed to have major and minor axis dimensions of 0.5km and 0.7km respectively (i.e. 25% of the outer dimensions).

The extent of any supporting structure for the solar reflectors is currently unknown. The following information has been gathered during discussions between Frazer-Nash Consultancy and IECL [4]:

- The mirrors are assumed to be a thin film stretched over an oval frame. It is assumed that the frame is manufactured from thin wall carbon fibre tube.
- The total mass of the mirrors and frame is expected to be 150 tonnes (per reflector).

2.2.0.3 Additional Structural Supports

The following information has been gathered during discussions between Frazer-Nash Consultancy and IECL [4]:

- Some form of structural support to link the edges of each reflector and fix them relative to one another is required. This will attach to the helix.
- The geometry of this support structure is unknown, however it is likely to be constructed from thin wall carbon fibre tube.
- It is expected that this structure will weigh approximately 200 tonnes.

2.3 Concept Definition

Using the inputs and data outlined in Section 2.2 , the concept has been defined for the purpose of developing an SPS model that forms the basis of the analysis and calculations. This comprises the helix, two reflectors, and a series of structural beams. The sizes and positions of these structural beams have been assumed in the absence of detailed design information.

2.3.1 Component Details

Figure 2.3 provides an overview of the assumed SPS structure, including the density (ρ), Young's Modulus (E) and Poisson's (ν) of the modelled components. Text on this figure has been colour coded to highlight whether data has been assumed, supplied, or has been calculated from supplied/assumed values. A summary of this data is provided below.

The reflectors:

- Each reflector is an ellipse with a major diameter of approximately 2,800m and a minor diameter of 2,000m. These are positioned at 45 degrees relative to the central axis of the SPS.
- The hole at the centre of each reflector has a major diameter of 700m and a minor diameter of 500m.
- In the absence of detailed information about the construction of the reflectors, they have been assumed to be a single surface with a thickness of 1m. This thickness has been chosen to reflect the fact that a significant supporting space frame will be required to ensure the reflectors remain planar.
- The mass, surface area, and thickness of the modelled reflectors have been either assumed or supplied. A density to achieve the correct mass has been back calculated from these values.
- The reflector will likely have a reasonably high stiffness due to its support frame (the details of which are unknown). An isotropic Young's Modulus equivalent to steel (200GPa) has therefore been assumed.

The helix:

- A helical surface based on a width of 2,000m rotated through 180 degrees, over a length of 2,000m.
- The top and bottom edges of the helix are aligned with the major diameter of the reflectors.
- The helix has been idealised as a single surface with a thickness of 1mm. This thickness has been chosen to reflect the approximate thickness of each "step" of the helix.
- The mass, surface area, and thickness of the modelled helix surface have been either assumed or supplied. A density to achieve the correct mass has been back calculated from these values.
- Given the sparse nature of the helix design, it is assumed that the isotropic Young's Modulus is several orders of magnitude less than that of the reflectors (i.e. 0.02GPa).

The structural beams:

- As a starting point, it has been assumed that the two reflectors are joined with a set of four structural beams (between four corresponding points on the two reflectors). This will ensure the reflectors are aligned with each other, and will provide a frame which will attach directly to the helix.
- It is assumed that these structural beams are 1m diameter hollow carbon fibre tubes with a wall thickness of 2mm.

- A density of 1,900 $\mathrm{kg/m^3}$ has been assumed, representative of a typical carbon fibre.
- The overall stiffness of the structural beams is assumed to be roughly equivalent to steel – a Young's modulus of 200 GPa will therefore be used.

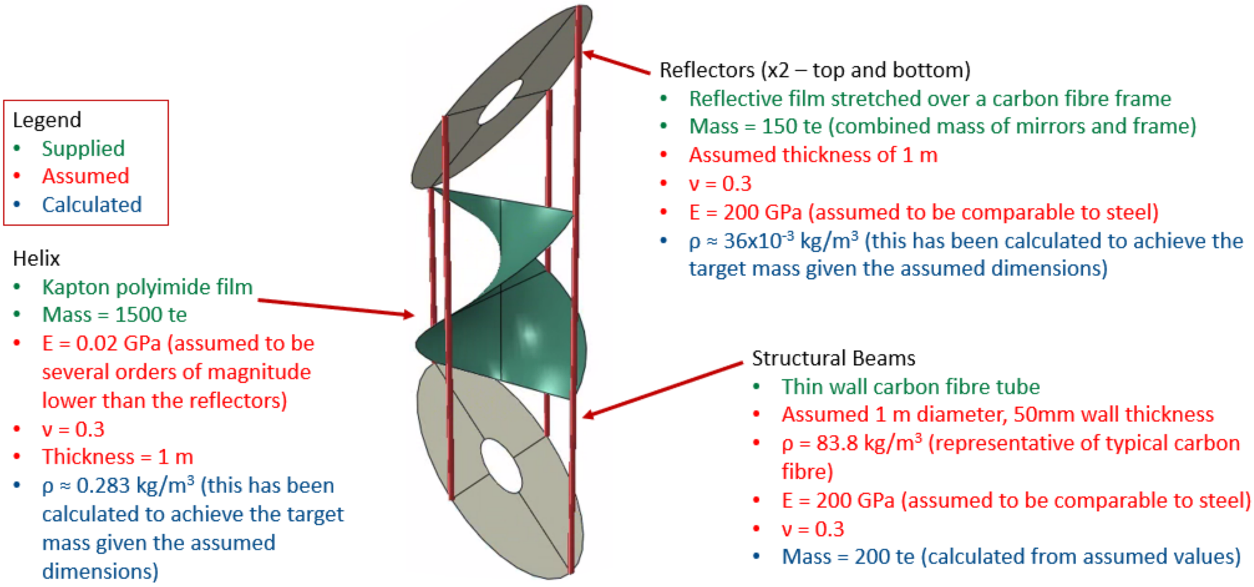

Figure 2.3: Overview of CASSIOPeiA Concept

The diagram in Figure 2.4 shows some dimensions of the SPS. These dimensions will be varied in the Parametric Study, as detailed in Section 7, but for the baseline scenario, it has been assumed that $b = c = 1$ km. and therefore, $d = \sqrt{b^2 + c^2} = \sqrt{2}$km.

2.3.2 Relative Stiffnesses

As mentioned in previous sections, the reflectors and stiffeners are intended to form a stiff structure which fixes the position of the reflectors relative to one another, and which also provides additional stiffness to the helix. It is therefore important that the structural supports in the concept definitions are stiffer than the helix. This has been confirmed using a simplified FE model to calculate the axial stiffness of the idealised helix surface (8.2×10^5 N/m), and hand calculations to calculate the axial stiffness of the four structural supports over the length of the helix (1.3×10^6 N/m).

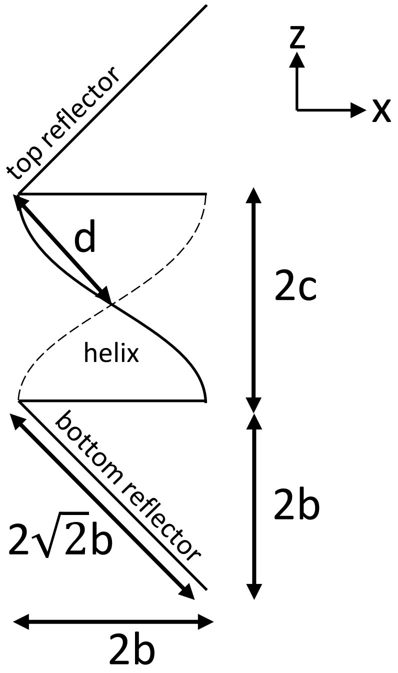

Figure 2.4: Diagram of the SPS seen from its side, showing dimensions and body reference frame. At the top and bottom are the reflectors, and in the middle is the helix. During nominal operations, the Sun is towards the right.

3 Orbital Loads

This section presents the loads that the SPS is subjected to. These can cause a deformation of the structure and/or a variation of the orbital parameters.

3.1 Earth Gravity

As a first approximation, the Earth's gravity field can be written as the potential of a uniformly distributed spherical mass, which is:

$$U = -\frac{\mu}{R_C} \tag{3.1}$$

To account for the aspherical distribution of the Earth's mass, however, it is common to use a spherical harmonics expression, leading to the following expression [6]:

$$U = \frac{\mu}{R_C}\left[1 - \sum_{l=2}^{\infty} J_l \left(\frac{R_\oplus}{R_C}\right)^l P_l\left(\sin\phi\right) + \sum_{l=2}^{\infty}\sum_{m=1}^{l}\left(\frac{R_\oplus}{R_C}\right)^l P_l\left(\sin\phi\right)\left\{C_{lm}\cos m\lambda + S_{lm}\sin m\lambda\right\}\right] \tag{3.2}$$

Where the first term on the right hand side is the point-mass gravity, next is the sum of the zonal effects, followed by the tesseral and sectoral effects. Of these, it's well known that J_2 is the largest effect, being approximately 1000 times stronger than the next zonal term. Of note, as well, is the C_{22} term, since for geosynchronous orbits (GSO) this term produces a resonance. In the orbital simulations that were produced, only the zonal terms up to J_4 were included. An upper bound for the propellant cost required to compensate for the C_{22} term, if the SPS is placed in a non-equilibrium position, was also calculated as detailed in Section 4.4.4.

3.2 Third Body Effect

The Sun and the Moon have a considerable influence on the orbit of a spacecraft, due to the difference in acceleration caused on the satellite and the Earth. This effect can be approximated as [6]:

$$a_3 \approx \frac{\mu_3}{R_3^3}\left(\mathbf{R}_C - 3\mathbf{R}_3\frac{\mathbf{R}_C\cdot\mathbf{R}_3}{R_3^2}\right) \tag{3.3}$$

Where a_3, μ_3 and $\mathbf{R}_3$ are the semi-major axis, the standard gravitational parameter, and the position vector of the third body relative to the Earth, and $\mathbf{R}_C$ is the SPS's position vector relative to the Earth.

3.3 Gravity Gradient

The gravitational acceleration for a point mass is given as:

$$\mathbf{g} = -\frac{\mu}{{R_C}^2}\hat{\mathbf{R}}_C \tag{3.4}$$

This acceleration varies spatially and, for a large structure, can lead to a structure deforming effect due to different accelerations being applied at different elements of the structure. To analyse this effect, a Taylor series is written around the center of mass of the structure, such that $\mathbf{g} = \mathbf{g}_0 + \mathbf{g}_1 + \mathbf{g}_2$. In the Radial-Transverse-Normal (RTN) frame of reference, these are [7]:

$$\mathbf{g}_1 = \frac{\mu}{R_C^3}[2r, -t, -n]^T \tag{3.5}$$

and

$$\mathbf{g}_2 = \frac{3\mu}{R_C^4}\left[\frac{1}{2}t^2 + \frac{1}{2}n^2 - r^2, rt, rn\right]^T \tag{3.6}$$

The first term, $\mathbf{g}_1$, clearly integrates to zero across the whole structure, if the expansion is done around the center of mass of the object. The second term, however, does not integrate to zero, but instead produces a force $\mathbf{G}_2$ that varies according to the orientation of the body in the RTN frame, as follows:

$$\mathbf{G}_2 = \int_M \mathbf{g}_2 dm = -\frac{3\mu}{R_C^4}\left[\frac{1}{2}I_{tt} + \frac{1}{2}I_{nn} - I_{rr}, I_{rt}, I_{rn}\right]^T \tag{3.7}$$

Where the inertia tensor values are written in the RTN frame (not in the principal body axis frame, or “body frame”, where by definition the products of inertia are zero, i.e. $I_{xy} = I_{xz} = I_{yz} = 0$). For the SPS in orbit, with $I_{xx} = I_{yy}$ in the body frame and having its Z axis constantly aligned with the normal to the ecliptic plane, the force is as follows:

$$\mathbf{G}_2 = \frac{3(I_{xx} - I_{zz})}{8mR_C^2} g_0 \begin{bmatrix} 6\sin^2(\theta)\cos(2i) + 3\cos(2\theta) + 1 \\ 8\sin(\theta)\cos(\theta)\sin^2(i) \\ 8\sin(\theta)\sin(i)\cos(i) \end{bmatrix} \tag{3.8}$$

In addition to the variation of this force along an orbit, due to its dependency on θ, i and R_C, deformations in the structure can also cause additional variations by causing I_{xx} and I_{zz} to vary. However, both analytical and numerical simulations have found this effect to be negligible.

It is convenient to write $\mathbf{g}_1$ in the body frame of reference,

$$\mathbf{g}_1 = \frac{\mu}{R_C^3}\left(3\left(\mathbf{R}_C \cdot \mathbf{r}\right)\mathbf{R}_C - \mathbf{r}\right) \tag{3.9}$$

Whilst $\mathbf{g}_1$ does not produce a resultant force, it does produce a torque that can be highly significant, as is explored in Section 4.1.

All other gravitational forces can also produce gradients, such as the third body and the aspherical potential terms, but these are much smaller as will be shown in Section 3.9.

3.4 Solar Radiation Pressure

Assuming a perfect specular reflection, if $\mathbf{n}$ is the vector normal to the reflector and $\hat{\beta}$ is the angle between this normal and the Sun vector, the Solar Radiation Pressure (SRP) force on each reflector will be [6]:

$$\mathbf{F}_{\text{reflector}} = -2\, p_{\text{SR}} A\, c_{\text{RS}} \cos^2\left(\hat{\beta}\right)\mathbf{n} \tag{3.10}$$

where A is the area of the reflector and $\hat{\beta}$ is the incidence angle, i.e. the angle between the surface normal and the incident sunlight. For perfect specular reflection $c_{RS} = 1$. Figure 3.1 illustrates the geometry. The angle β represented in that figure is defined as zero under nominal conditions, i.e., when the SPS is facing the Sun. Therefore, for the top reflector $\hat{\beta} = \pi/4 - \beta$, while for the bottom reflector $\hat{\beta} = \pi/4 + \beta$.

At the mean distance between the Sun and the Earth, $p_{\mathrm{SR}} = 4.57 \times 10^{-6}\mathrm{N/m^2}$. The resultant force when $\alpha = \beta = 0$ evaluates to:

$$F_{\mathrm{SRP}} = \sqrt{2}\, p_{\mathrm{SR}}\, A\, c_{\mathrm{RS}} \approx 28.7\mathrm{N} \tag{3.11}$$

This force naturally varies with α and β, but not with γ as that is a rotation about the Sun vector. The variation of the force with α and β is not of much interest since, during normal operations, they will both be equal to zero. However, there is a positive feedback effect due to the moment about the Y axis:

$$M^{y}_{\mathrm{SRP}} = \sqrt{2}(b+c)\, p_{\mathrm{SR}} A\, c_{\mathrm{RS}} \cos(\alpha)\sin(\beta)\cos(\beta) \tag{3.12}$$

As the angle β increases, M^{y}_{SRP} also increases, introducing positive feedback. Linearizing and dividing by I_{yy} produces the following:

$$\ddot{\beta} \approx \sqrt{2}(b+c)\, p_{\mathrm{SR}} A\, c_{\mathrm{RS}} \beta = A_{\beta}\beta \tag{3.13}$$

where $A_{\beta} \approx 3.2 \times 10^{-8}\mathrm{s}^{-2} = 239\mathrm{day}^{-2}$ which is equivalent to approximately 2 kN·m/°. This torque is much smaller than the gravitational torque (of approximately 20 kN·m) for small deviations in β. If the spacecraft becomes completely uncontrolled and $\beta = \pm 45°$, this torque can reach 57 kN·m, which is of similar magnitude to the gravitational torque. However, this is not a situation that can be expected during a nominal mission. When considering the idea, proposed in [5], of using reflectors to passively control the SPS, one must consider that the control force would have to, at least, counter this positive feedback effect. This is discussed in more detail in Section 4.2.

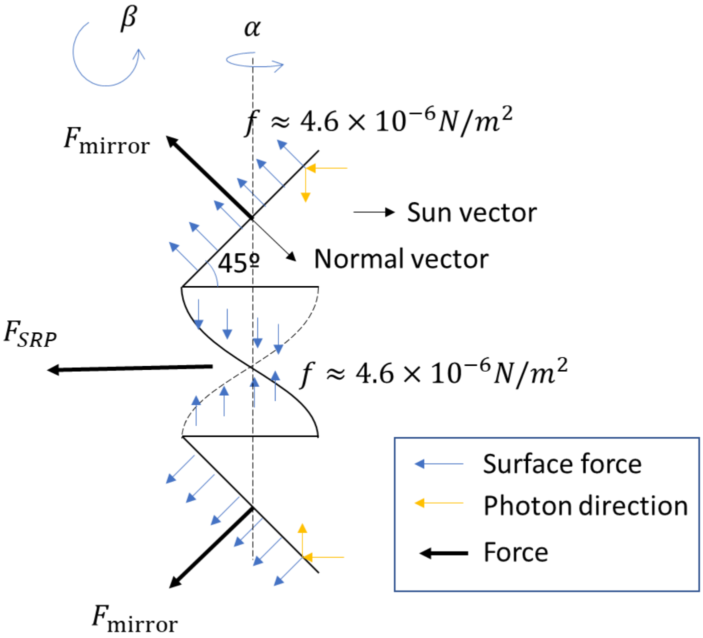

Figure 3.1: SRP forces

3.5 Earthshine and Earth's IR emissions

The Earth also emits radiative power, in the form of reflected solar light (Earthshine or albedo) and of emitted IR radiation. Wertz [8] (Table 17-1) gives an estimate of 12 W/m^2 and 3 W/m^2 for the Earthshine and IR radiation at an altitude of 30000 km, which is below GEO mean altitude (35786 km). This gives a total of around 15 W/m^2, which is much smaller compared to direct sunlight of 1367 W/m^2.

3.6 Thrusters

For attitude and orbital control, it is necessary to have thrusters in the SPS, see Chapter 4. The attitude can be controlled using thrusters placed away from the center of mass of the structure, and applying thrust in such a way as to cancel $\mathbf{M}_{g1}$. Looking at the structure, the only locations at which to place them are the four corners of the SPS, see Figure 3.2, as these are where beams have already been placed to ensure structural stability of the spacecraft, besides being a location that allows any combination of resultant torque and force to be applied on the structure.

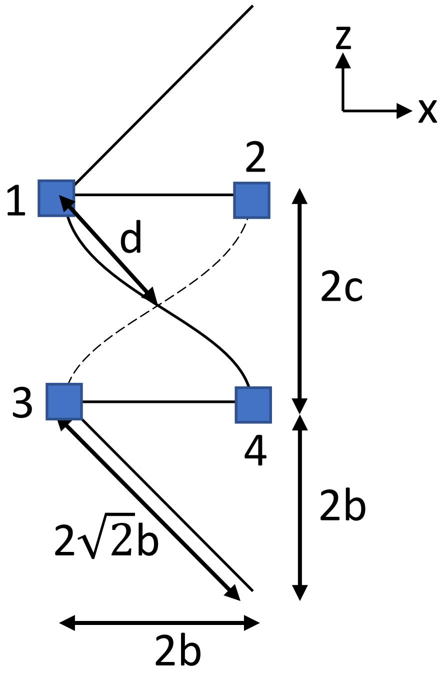

Figure 3.2: Repetition of Fig. 2.4, with numbered squares representing the locations of the thrusters. The xz component of the thrust force produced by the thruster 1 is also represented. In this representation, this force is producing a negative moment around the Y axis, which goes into the page.

These thrusters will also deform the SPS. The need for attitude control will drive the requirements for the thrusters to provide torque about the X and Y axis, but not about the Z axis, as the inertia tensor has a symmetry about this axis. Let b and c be the horizontal and vertical dimensions of the SPS as also shown in Fig. 3.2, and $\mathbf{F}^i$ be the force applied by the i-th thruster in the body frame. The resultant force is simply $\sum_i \mathbf{F}^i$. To achieve torques M_T^x and M_T^y, the force vectors are given by:

$$\begin{aligned} \mathbf{F}_1 &= \left[-ck_{mx}, k_{my}, -bk_{mx}\right]^T \\ \mathbf{F}_2 &= \left[-ck_{mx}, k_{my}, bk_{mx}\right]^T \\ \mathbf{F}_3 &= \left[ck_{mx}, -k_{my}, -bk_{mx}\right]^T \\ \mathbf{F}_4 &= \left[ck_{mx}, -k_{my}, bk_{mx}\right]^T \end{aligned} \tag{3.14}$$

where,

$$\begin{aligned} k_{mx} &= -\frac{M_T^x}{4d^2} \\ k_{my} &= -\frac{M_T^y}{4c} \end{aligned} \tag{3.15}$$

and $d = \sqrt{b^2 + c^2}$. The minus signs in k_{mx} and k_{my} are for convenience, since to cancel torques $\mathbf{M}_g$ applied to the structure, so we will want to make $\mathbf{M}_T = -\mathbf{M}_g$.

3.7 Microwave Beam

The microwave beam also produces a force similar in nature to the SRP, i.e. it is caused by moment transfers mediated by photons. The microwave photons being emitted by the SPS towards the rectenna on the Earth carry with them linear momentum and, as such, a force is applied on the SPS in the opposite direction. If it is assumed that the microwave beam is always pointing towards the centre of the Earth, this force rotates around the body during an orbit. The exact modelling of the microwave beam force distribution across the helix would require greater detail on the design than is currently available, as well as more time to properly simulate the electromagnetic field and its interactions with the structure. Therefore, for this analysis, it was considered to be uniformly distributed across the helix's surface.

With the current configuration, 8.6 GW of power is captured by the spacecraft. To obtain 2GW of power, the total conversion efficiency is 0.23. It has been assumed that the efficiency of the conversion to microwaves is 0.5, and the rest of the losses come from the transmission through atmosphere and conversion in the rectenna. The resulting total microwave force is of the order of 14N. Assuming this force is uniformly distributed gives a pressure of 2.3×10^{-6} N/m^2 distributed over the reflectors, similar to the SRP.

3.8 Earth's Magnetic Field

The magnetic field strength in GEO, from the GEOS mission results, can reach values of approximately $B = 120$ nT [9]. Discussions of space tethers [7], which are examples of large structures in space such as the ones under consideration, mention the Lorentz force as a potentially significant force applied on a tether, and even suggest using it for orbital control. A straight wire with length and direction given by the magnitude and direction of $\mathbf{L}$, current I, and under a magnetic field $\mathbf{B}$, is subject to the Lorentz force:

$$F_{\text{Lorentz}} = I\mathbf{L} \times \mathbf{B} \tag{3.16}$$

Calculating this force would require a complete definition of the electrical system in the SPS, which is not available at the moment. To get a worst case estimate, suppose that there is a wire running the entire length (2km) of the helix carrying the entire power of the SPS, resulting in a current of 20kA at 100kV (typical for high voltage DC lines), and that this wire is orthogonal to the magnetic field. This results in a force of approximately 5N, which would be significant, at approximately 20% of the SRP force. However, there is no reason to believe there would be such a wire. The information available suggests that each panel can work independently, and that current is going from the solar panels directly to the antenna in each panel. Furthermore, given that each panel is in a different orientation, so would the currents generated, leading to the Lorentz forces applied on each of them cancelling out. However, a structural load could result from this, which should be studied when the electrical system is defined.

3.9 Comparisons

The loads described in this chapter can produce changes in the orbital dynamics, which are measured by the resultant forces from these loads, when added up across the entire mass of the SPS. When the loads apply with different magnitude across the structure, they can deform it. These loads can be split into body forces and surface forces. Body forces are those that are distributed across the volume of a structure, and can be measured in N/m^3 or N/kg = m/s^2. Since the body forces are the gravitational gradients, which are accelerations, they are more convenient to measure in N/kg. They are compared in Table 3.1. The surface forces, such as the SRP and the microwave beam force, are those that are distributed over a surface of the structure, and as such can be measured in N/m^2. These are compared in Table 3.2. Both of these tables show the magnitude of the resultant force as well as the maximum force applied to elements of the structure. The more significant values are in bold.

Table 3.1: Comparison of the orders of magnitude of the body forces. F/W is the resultant of the force divided by the spacecraft's weight, producing a non-dimensional force.

	F/W [non-dimensional]	Maximum body force [N/kg]
$\mathbf{g}_1$		$\mathbf{2 \times 10^{-5}}$
$\mathbf{g}_2$	2×10^{-9}	2×10^{-9}
J_2	$\mathbf{4 \times 10^{-5}}$	1×10^{-9}
J_3	1.3×10^{-8}	2×10^{-13}
C_{22}	5×10^{-8}	1×10^{-9}
3rd body - Moon	$\mathbf{1.6 \times 10^{-5}}$	10^{-10}
3rd body - Sun	$\mathbf{7.4 \times 10^{-6}}$	10^{-10}

Table 3.2: Comparison of the orders of magnitude of the surface forces. F/W is the resultant of the force divided by the spacecraft's weight, producing a non-dimensional force.

	F/W [non-dimensional]	Maximum surface force [N/kg]
SRP	$\mathbf{6.4 \times 10^{-5}}$	$\mathbf{4.6 \times 10^{-6}}$
Earthshine + Earth IR	6.4×10^{-7}	4.6×10^{-8}
Microwave beam	$\mathbf{3.2 \times 10^{-5}}$	$\mathbf{3.6 \times 10^{-6}}$

4 Attitude and Orbital Dynamics

4.1 Attitude Stability

The requirement that the Z axis be perpendicular to the Sun, thus putting the SPS away from an equilibrium position, may appear to be unnecessary. As discussed in Appendix B, this requirement is not necessary, and removing it can reduce the propellant requirements, but not eliminate them altogether. This is because it is not possible to have the SPS in this equilibrium attitude and with its X axis pointing towards the Sun at all times. This geometrical fact is best understood by considering that when the Sun in not in the orbital plane, the X axis must be pointing out of plane. Since the Z axis is by definition normal to the X axis, it is then impossible for Z to be normal to the orbital plane as that can only happen if X is in the orbital plane. When the Sun is in the orbital plane, which is when $\Omega_{\odot} = 0$ or π, the X axis is too, and therefore the SPS can be in equilibrium. This fact is confirmed by the numerical optimization analysis in Appendix B.

4.1.1 Gravity Gradient Torque

As written in Section 3.3, the gravity gradient $\mathbf{g}_1$ produces a torque, which, written in the body frame, is given by:

$$M_{g1} = -3\frac{\mu}{R_C^3}\begin{bmatrix}(I_{yy} - I_{zz})\,\hat{R}_y\hat{R}_z \\ (I_{zz} - I_{xx})\,\hat{R}_x\hat{R}_z \\ (I_{xx} - I_{yy})\,\hat{R}_x\hat{R}_y\end{bmatrix} \tag{4.1}$$

where $\hat{R}$ are the components of the normalized position vector of the Centre of Mass (CoM) in the body frame (i.e. a frame aligned with the principal axis of inertia). This torque is highly significant. If the principal axes of the body are not aligned with the RTN frame, the resultant torque can cause rotational accelerations of the order of n^2, n being the mean motion of the satellite.

The alignment that is closest to an equilibrium orientation is when the Z axis of the SPS is perpendicular to the orbital plane (as opposed to the ecliptic plane), the N direction in the RTN frame. The work in [1] provides a basis for analysing the stability of these equilibrium conditions, based on the values of the quantities:

$$k_R = \frac{I_{nn} - I_{tt}}{I_{rr}} \tag{4.2}$$

$$k_Y = \frac{I_{nn} - I_{rr}}{I_{tt}} \tag{4.3}$$

For the baseline SPS and in this alignment (where $I_{nn} = I_{zz}$ and $I_{rr} = I_{tt} = I_{xx} = I_{yy}$, both of these quantities are around -0.8. The map in Figure 4.1, taken from [1], shows the regions of stability and instability, as a function of K_R and K_Y, with the values for the baseline SPS design overlaid. Clearly, this equilibrium attitude is an unstable one.

The order of magnitude of the angular acceleration, together with this instability, would mean that in a time scale of days the SPS would be completely out of alignment with the Sun frame. For the body frame, with the current assumptions on the mass distribution, x is the direction we want pointing at the Sun, z is the vertical axis, and y completes the triad (horizontal axis orthogonal to x). The gravity gradient torque has an order of magnitude of around 2×10^4N.m, resulting in angular accelerations of the order of 2400º/day^2 for GEO or Geosynchronous Laplace Plane Orbit (GLPO). Therefore, attitude control is an indispensable requirement for this design.

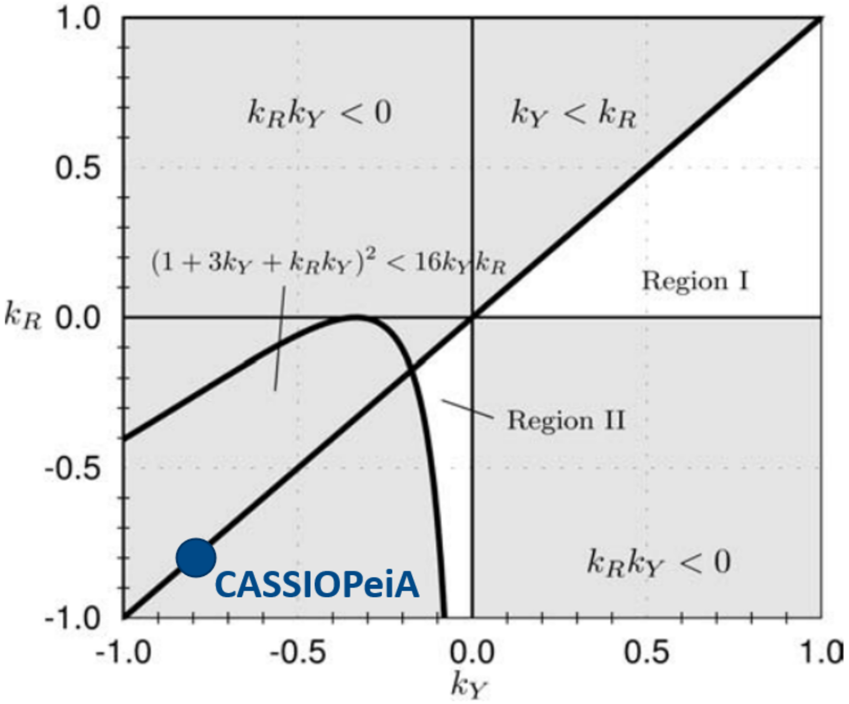

Figure 4.1: Attitude stability of equilibrium orientations, with the case of CASSIOPEIA marked. Shaded areas mark unstable regions, while white areas mark stable regions. Underlying graph was sourced from [1].

4.1.2 Other sources of torque

The SRP and microwave forces, under nominal conditions, do not produce a torque on the structure, due to the symmetry of the system. However, this symmetry can be broken by the SPS deforming, or by an imbalance in propellant mass storage. The results of the ray tracing analysis on the deformed structure of the SPS, as presented in Section 6, produced a torque that reaches 32 Nm, around 3 orders of magnitude smaller than M_{g1}, and corresponds to a distance between the CoM and Centre of Pressure (CoP) of around 1 metre. Since at this point we do not know exactly how the microwave force is distributed along the structure, the resulting torques cannot be provided for this force. The SRP and microwave forces are around 30N and 15N respectively. If the CoM varies due to a mass imbalance in propellant mass storage, however, this too can result in torques.

If D is the distance between the CoM and CoP for a force of magnitude F, the torque produced is FD. For $D = 100m$, we get 3 kN.m for SRP, which is around one order of magnitude below the gravity gradient torque. Therefore, if this distance stays below 100 m, the torques produced do not significantly alter the rest of our calculations. If at one of the corners of the helix we have an excess mass of 8 tonnes (estimated propellant cost per year, see Section 4.2), the CoM would move by approximately 6 metres. This would lead to a torque of around 255 Nm, which is very small when compared to M_{g1}. Note, however, that a mass imbalance in propellant storage is not expected, since the assumed thruster configuration is such that all thrusters will have the same propellant consumption at all times.

4.2 Attitude Control

Attitude control is required to keep the structure stable. Any method of attitude control, from reaction wheels, thrusters, etc. could be capable of causing distortions to the structure of the SPS, which can interact with the gravitational and SPS loads as previously mentioned for other distortions. In [5] there is mention of using reflectors, which, with the SRP force, could allow stabilizing the angle α. However, as mentioned in Section 3.4, there is a positive feedback with the SRP force. To counter this force would require reflectors of a similar size to the existing reflectors, which is completely unfeasible. If reflectors are placed at angle β_c and at coordinates $z = \pm(c + 2b)$, so just above the reflectors as shown in [5], the restoring torque they produce is, after linearizing around $\beta = 0$:

$$M_2^y \approx 3p_{\mathrm{SRP}}\, c_{\mathrm{RS}}\, A_2(b + 2b)\cos\beta_c \sin^2\beta_c\beta \tag{4.4}$$

This value has a maximum at $\beta_c \approx 54.7°$, and to counter the effect in Eq. (3.13) these passive control reflectors would have to have an area of:

$$A_2 = \frac{\sqrt{2}(b + c)}{3(c + 2b)\cos\beta_c \sin^2\beta_c} A \tag{4.5}$$

which results in $A_2 \approx 3.6\mathrm{km}^2$, which is 82% of the area of the existing reflectors, a very significant area which is much greater than implied by the figures in [5]. This area requirement is to counter the positive feedback effect on β, additional mirror area would be needed to also control for other disturbances such as the gravity gradient torque. Furthermore, as the SRP forces are not sensitive to angle γ, it is not possible to control for this rotation with passive reflectors alone. Therefore, controlling the SPS's attitude with reflectors alone is not feasible, and alternative methods need to be considered.

4.2.1 Mass Distribution

Given that the moments produced by the gravity gradient torque are proportional to $I_{xx} - I_{zz}$, a change in design so that we have $I_{xx} = I_{zz}$ would greatly reduce the need for attitude control, apart for requirements to stabilize the SPS in case its attitude is perturbed. A naive way to achieve this would be to add extra mass to the system. If one were to add a ring of mass in the xy plane with radius $c = 1$ km, would necessitate an additional mass of approximately $\frac{2(I_{xx}-I_{zz})}{c^2} \approx 5900$ tonnes, making such an approach unfeasible. That said, reducing the magnitude of $I_{xx} - I_{zz}$ should still be a design consideration, as it dictates the attitude control requirements.

4.2.2 Attitude Control Thrusters

In order to actively control the attitude of the structure, there must be at least a torque of the form $\mathbf{M}_T = -\mathbf{M}_g$, and as such the forces are given by Eq. (3.14), but with the constants now given by:

$$\begin{aligned} k_{mx} &= \frac{M_{g1}^x}{4c} \\ k_{my} &= \frac{M_{g1}^y}{4d^2} \end{aligned} \tag{4.6}$$

It is useful to write M_{g1} as a function of the orbital elements:

$$\mathbf{M}_{g1} = -k_{g1} \sin i \begin{bmatrix} -\left(\cos i \cos \Omega_{\odot} \left(1 - \cos 2\theta\right) + \sin \Omega_{\odot} \sin 2\theta\right) \\ \cos \Omega_{\odot} \sin 2\theta - \cos i \sin \Omega_{\odot} \left(1 - \cos 2\theta\right) \\ 0 \end{bmatrix} \tag{4.7}$$

where,

$$k_{g1} = \frac{3}{2} \frac{\mu}{R_C^3} \left(I_{xx} - I_{zz}\right) \tag{4.8}$$

We can now estimate the required forces from the thrusters. The quantities inside the vector part of Eq. (4.7) can be shown analytically to never exceed $1+\cos i$. This can be done by writing them in the form of $A(\Omega_{\odot})\cos(2\theta+\Phi(\Omega_{\odot}))+B(\Omega_{\odot})$ and looking for an upper bound on $A+B$. This shows that the maximum magnitude of both M_{g1}^x and M_{g1}^y never exceeds:

$$|M_{g1}^x|, |M_{g1}^y| \leq k_{g1} \left(\sin i + \cos i \sin i\right) = k_{g1} \left(\sin i + \frac{1}{2} \sin 2i\right) \tag{4.9}$$

where in k_{g1}, we use $R_C = a(1-e)$, which is the pericentre distance, using the values from Section A.4. The second equality is obtained using the double angle formula, to obtain an expression where it is clearer what the magnitude will be. In the XZ plane, the maximum force, perpendicular to the moment arm, required from each of the thrusters is:

$$\|\mathbf{F}_{i,\max}^{xz}\| = k_{g1} \frac{\left(\sin i + \frac{1}{2} \sin 2i\right)}{4d} \tag{4.10}$$

For the force in the $\pm Y$ axis, its maximum magnitude is:

$$F_{i,\max}^{y} = k_{g1} \frac{\left(\sin i + \frac{1}{2} \sin 2i\right)}{4c} \tag{4.11}$$

Using $b = c = 1$ km and $d = \sqrt{2}$ km, results in $F_{i,\max}^{xz} \approx 3.6$ N and $F_{i,\max}^{y} \approx 5$ N. From [3], in the design of a control system for Abaqus, a set of 1N thrusters with specific impulse $I_{\text{sp}} = 5000$ s, a mass/power ratio of 5 kg/kW, and a power/thrust ratio of 30 kW/N has been considered. This gives a mass estimate for the propulsion system of $30 \times 5 \times 8(F_{i,\max}^{xz} + F_{i,\max}^{y}) \approx 10$ tonnes of dry mass, where the 8 comes from the 4 locations multiplied by two due the fact that thrusters are needed in both directions.

The propellant cost can be estimated using Eq. (3.14) and (4.7). First it is observed that:

$$m_{\text{prop}} = \int \dot{m}_{\text{prop}} \, dt = \int \sum_i \frac{\|\mathbf{F}_i^{xz}\| + F_i^y}{I_{\text{sp}} g_0} \, dt = \frac{1}{I_{\text{sp}} g_0} \int \left(\frac{|M_{g1}^y|}{c} + \frac{|M_{g1}^z|}{d} \right) dt \tag{4.12}$$

where g_0 is the sea-level gravitational acceleration, as the definition of the specific impulse I_{sp} is such that $I_{\text{sp}} g_0$ is the effective exhaust velocity. Here it was assumed that the thrusters in the XZ plane are pointing in the directions normal to the moment arms of each thruster, in addition to thrusters pointing in the $\pm Y$ directions. Introducing the spent momentum H_s^x and H_s^y:

$$H_s^{(\cdot)} = \int |M_{g1}^{(\cdot)}| \, dt \tag{4.13}$$

which gives,

$$m_{\text{prop}} = \frac{1}{I_{\text{sp}} g_0} \left(\frac{H_s^y}{c} + \frac{H_s^x}{d} \right) \tag{4.14}$$

Using Eq. (4.7) the torque can be split into a twice-daily $\mathbf{M}_{g1,2\theta}$ and a yearly $\mathbf{M}_{g1,\odot}$ component, remembering that $\Omega_\odot = \Omega - L_\odot$ (see Fig. A.2):

$$\begin{aligned}\mathbf{M}_{g1,2\theta} &= -\,k_{g1}\sin i\begin{bmatrix}\cos i\cos\Omega_\odot\cos 2\theta+\sin\Omega_\odot\sin 2\theta\\ \cos\Omega_\odot\sin 2\theta+\cos i\sin\Omega_\odot\cos 2\theta\\ 0\end{bmatrix}\\ \mathbf{M}_{g1,\odot} &= k_{g1}\sin(2i)/2\begin{bmatrix}\cos\Omega_\odot\\ \sin\Omega_\odot\\ 0\end{bmatrix}\end{aligned} \tag{4.15}$$

It is easily seen that $\mathbf{M}_{g1,2\theta}$ varies with an angular frequency of approximately $2n$, while $\mathbf{M}_{g1,\odot}$ varies with angular frequency $\dot{L}_\odot$, the time derivative of $L_\odot$, which also corresponds to the Earth's mean motion. Analytical expressions for $\mathbf{H}_{s,2\theta}$ and $\mathbf{H}_{s,\odot}$ can be easily estimated by averaging:

$$\mathbf{H}_{s,\odot} = \int_0^t \|\mathbf{M}_{g1,\odot}(\tau)\|\,\mathrm{d}\tau \approx \frac{t}{T_\odot}\int_0^{T_\odot}\|\mathbf{M}_{g1,\odot}(\tau)\|\,\mathrm{d}\tau = \frac{k_{g1}\sin 2i}{\pi}\begin{bmatrix}t\\ t\\ 0\end{bmatrix} \tag{4.16}$$

and, following the same approach,

$$\mathbf{H}_{s,2\theta} \approx \frac{k_{g1}\sin i}{\pi}\begin{bmatrix}t\\ t\\ 0\end{bmatrix} \tag{4.17}$$

using $\int_0^T |\sin(2\pi t/T+\phi)|\,\mathrm{d}t/T = 2/\pi$. This leads to $9.4\times10^{10}\mathrm{N.m.s/year}$ for $\mathbf{H}_{s,2\theta}$, and $1.7\times10^{11}\mathrm{N.m.s/year}$ for $\mathbf{H}_{s,\odot}$. Inserting into Eq. (4.14) leads to a propellant mass estimate of 3.3 tonnes/year for $\mathbf{H}_{s,2\theta}$ and 6 tonnes/year for $\mathbf{H}_{s,\odot}$, using $b = c = 1$ km, and $I_{\mathrm{sp}} = 5000$ s. If these are added up, we'd get an estimate of 9.3 tonnes/year of total propellant cost, but this would be a pessimistic assumption, since at some points during the orbit, the two components would be acting in opposite directions. Furthermore, i and Ω are not constant. Given the difficulty in analytically integrating the absolute value of the expressions in Eq. (4.7) without these approximations, the results of the numerical simulations in Section 4.1 were used instead, producing the results in Figure 4.2. These results give $\dot{H}_s^x \approx \dot{H}_s^y \approx 1.58{\times}10^{11}\mathrm{N.m.s/year}$, which, when inserted into Eq. (4.14), result in a propellant cost of $5.5\ \mathrm{tonnes/year}$. This is lower than even the estimate for $\mathbf{H}_{s,\odot}$, because during this orbit, the orbital plane gets closer to the ecliptic plane, lowering the propellant requirements, while the estimate was produced using $i = \epsilon$. To discount the effect of the precession of the orbital plane, $|M_{g1,2\theta} + M_{g1,\odot}|$ can be integrated numerically over a year while keeping i and Ω constant, resulting in $H_s^x = H_s^y \approx 2.3\times10^{11}$ N.m.s/year, meaning 8 tonnes/year of propellant consumed while in GEO orbit.

4.2.3 Momentum wheels or Control Moment Gyros

Given the high propellant costs associated with using thrusters for attitude control, propellantless options ought to be considered. One approach considered in [3] is to use momentum storage devices, such as control moment gyroscopes (CMG) or momentum wheels. The angular momentum storage requirement is given by:

$$\mathbf{H}(T) = \int_0^T -\mathbf{M}_{g1}(t)\,\mathrm{d}t \tag{4.18}$$

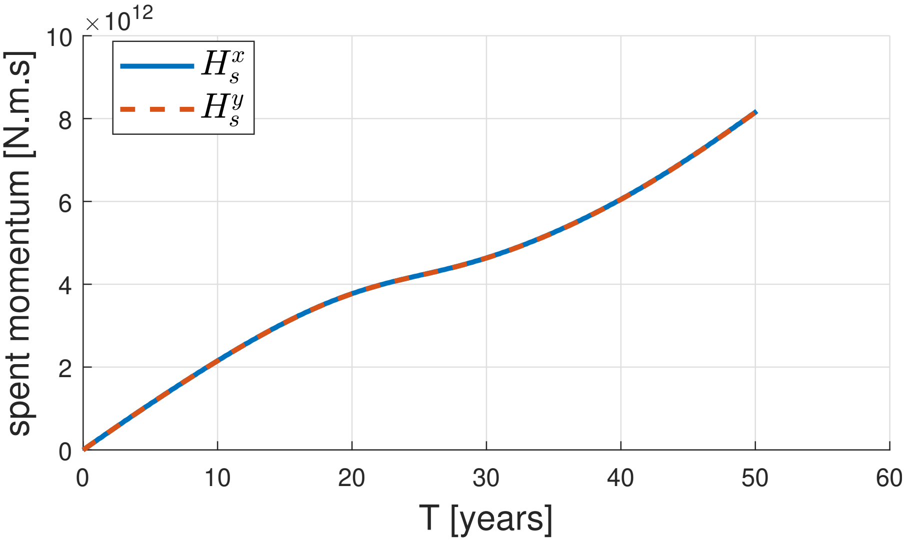

Figure 4.2: Spent angular momentum, or the integral of the absolute value of the torques in the x and y directions, from simulations for GEO orbit in Section 4.1.

Note the difference between $\mathbf{H}$ and $\mathbf{H}_s$ - the latter is an integral of the absolute value of the momentum. The momentum stored in the wheel at one point in the orbit can be used later when the torque is in the opposite direction to it.

Given that $\dot{L}_\odot \ll 2n$, $\mathbf{M}_{g1,2\theta}$ can be integrated considering $\Omega_\odot$ constant. We get for the stored moment $\mathbf{H} = \mathbf{H}_{2\theta} + \mathbf{H}_\odot$, which are sinusoidals with frequency $2n$ and $\dot{L}_\odot$, and amplitudes:

$$\begin{aligned} |H_{2\theta}^x|, |H_{2\theta}^y| &\leq \frac{k_{g1}}{2n} \sin i \sqrt{\cos^2 i \cos^2 \Omega_\odot + \sin^2 \Omega_\odot} \leq \frac{k_{g1}}{2n} \sin i \approx 6.4 \times 10^7 \text{ N.m.s} \\ |H_\odot^x|, |H_\odot^y| &\leq \frac{k_{g1}}{2\dot{L}\odot} sin 2i \approx 4.3 \times 10^{10} \text{ N.m.s} \end{aligned} \tag{4.19}$$

Clearly, the yearly effect leads to much higher momentum storage requirements. For reference, the International Space Station (ISS) has CMGs with a total capacity for storing 20,000 N.m.s [3], and so even $H_{2\theta}$ is around 6,400 times higher than this requirement. In addition, because Ω and i are also varying, there are effects with period greater than a year. The eccentricity would also have an effect that was not considered. Given that the Argument of Pericentre (AP) is varying yearly, as will be shown in Section 4.3, it would be expected to add to the yearly effect. Numerical simulations confirm our results, and also show a secular effect, shown in Figure 4.3, of around 4.5×10^8 and 2.6×10^9 N.m.s/year. The variation in amplitude of the yearly effect seen in that figure is due to the variation in inclination and Right Ascension of the Ascending Node (RAAN) that is discussed in Section 4.1 (See Appendix Section A.4 for definitions).

Given that the $\mathbf{H}_{2\theta}$ component of the momentum storage has a much smaller magnitude, besides using only thrusters or momentum wheels/CMGs for attitude control, there is also the option of using both in combination: the wheels/CMG to cancel the $2n$ frequency effect and the thrusters to cancel the rest.

Roithmayr [3] gives values for the moment control gyroscopes such as those used by the ISS, which are repeated in Table 4.1. Using these values, the momentum storage requirements for $H_{2\theta}$ lead to an estimate of 4,600 tonnes of mass, which makes this system unfeasible for our application. The same paper also mentions a concept for a momentum control wheel, with much better parameters. Table 4.1, also taken from [3], shows the parameters for this system. Using these values, the total mass requirements are clearly determined by the momentum storage. For $H_{2\theta}$, these would be around 2 tonnes, making this a much more feasible option. Controlling the yearly accumulation of angular moment, however, would require 1303 tonnes. As such, the yearly and secular components would still need to be controlled using thrusters. Numerical integration of $|M_{g1,2\theta} + M_{g1,\odot}|$ results in $H_s^x = H_s^y \approx 2.3 \times 10^{11}$ N.m.s/year, meaning the momentum wheel would only allow a saving of around 24% in propellant costs. It would also lead to a reduction in force requirements, of $\sin(i)/(\sin(i) + \sin(2i)/2) \approx 0.52$, which would lead to a reduction in the dry mass of the propellant system of around 5 tonnes, for a net reduction of 3 tonnes when accounting for the mass of the momentum wheels themselves.

Overall, while momentum storage could lead to reductions in both dry mass and propellant mass requirements, since it is a low Technology Readiness Level (TRL) concept, and the document where this system is defined [10] is not publicly available, for the rest of this work, the attitude is considered to be controlled exclusively with thrusters.

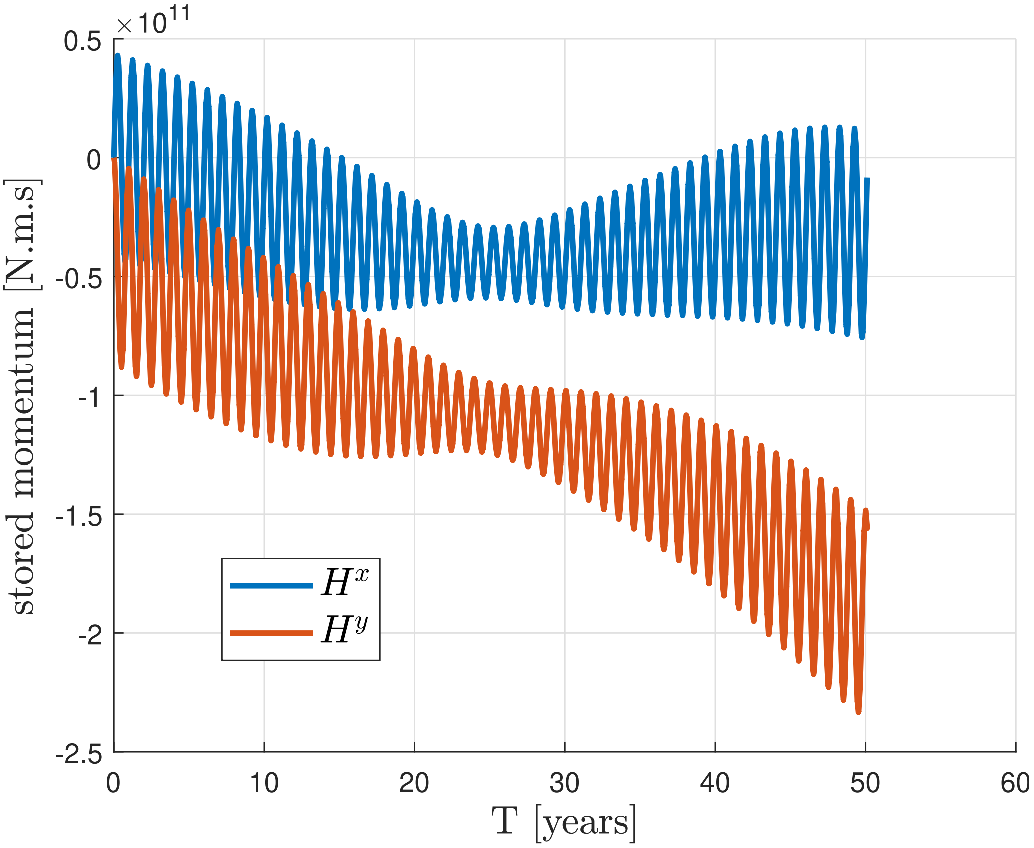

Figure 4.3: Plot of the angular momentum in the x and y directions that a momentum wheel would need to store in order to cancel the gravity gradient torque. The oscillation $H_{2\theta}$ is not noticeable due to its small magnitude compared to $H_\odot$.

Table 4.1: A large single-gimbal CMG. Table copied from [3].

Cost	$\$1\mathrm{M}$
Momentum	$7,000\ \mathrm{N \cdot m \cdot s}$
Max torque	$4,000\ \mathrm{N \cdot m}$
Peak power	$500\ \mathrm{W}$
Mass	$250\ \mathrm{kg}$
Momentum/mass	$28\ \mathrm{N \cdot m \cdot s/kg}$

Table 4.2: A space-constructed, large-diameter momentum wheel. Table copied from [3].

Momentum = 4×10^8 N · m · s	Rim radius = 350 m
Max torque = 30,000 N – m	Mass = 6000 kg
Material = aluminum	Max power = 19 kW
Natural frequency = 0.22 Hz	Max speed = 6rpm
Momentum / mass = 66,000 N · m · s/kg	cost = TBD

4.3 Orbital Stability

To maintain position over approximately the same point on Earth, CASSIOPEIA is placed in GEO. This orbit is characterized by a semimajor axis $a = 42164$ km, and by being equatorial, see Appendix A. Since the orbital elements are defined relative to the ecliptic plane, this means $i = \epsilon \approx 23.4°$, where ϵ is the obliquity of the ecliptic, i.e., the angle the ecliptic plane makes with the equatorial plane.

When considering a satellite orbiting around a point mass, where the potential is given by Eq. (3.1), the Keplerian or Equinoctial orbital elements stay constant apart from the fast variable (e.g. θ, ν, L). However, the presence of perturbative accelerations that were described in Chapter 3 causes these elements to vary. The SPS having a high area-to-mass ratio, means that its orbital dynamics are strongly affected by the SRP.

The orbital dynamics of high area-to-mass ratio spacecraft have been the subject of much discussion, of which the works by Rosengren et al [11, 12] were found to be particularly useful. McNally [2] applies the results and methodology in these references to the analysis of the orbital dynamics of SPS systems. It is not the point of this report to repeat this analysis, but a brief overview will be presented, followed by numerical simulations intended to confirm these results.

The works cited above describe in general two main effects. An in-plane variation of the eccentricity and argument of pericentre, and a precession of the orbital plane. The precession of the orbital plane contains effects coming from all perturbations under consideration, and in those works, they used Milankovitch elements to describe these effects, after averaging the variations over the periods of these perturbations (e.g. the SRP effect is averaged over a year, the Moon's effect is averaged over a Lunar month and over the precession of the Lunar nodes, etc.) Making a zero eccentricity approximation $e = 0$, their result has the form [12]:

$$\dot{\hat{\mathbf{h}}} = \boldsymbol{\omega}_{\mathbf{h}} \times \mathbf{h} = -\left(\omega_{J_2}\left(\mathbf{p} \cdot \mathbf{h}\right)\mathbf{p} + \omega_{\mathrm{ecl}}\mathbf{H}_{\odot}\right) \times \mathbf{h} \tag{4.20}$$

where

$$\omega_{\mathrm{ecl}} = \left(\omega_{\odot} + \omega_{\mathrm{Moon}}\right)\left(\hat{\mathbf{H}}_{\odot} \cdot \hat{\mathbf{h}}\right) + \omega_{\mathrm{SRP}} \tag{4.21}$$

the vectors $\hat{\mathbf{p}}$ and $\hat{\mathbf{H}}_{\odot}$ are the direction of the Earth's North pole and the angular momentum of the Earth's orbit around the Sun. The $\omega_{(\cdot)}$ quantities are the precession rates caused by each effect, and are defined as:

$$\begin{aligned} \omega_{J_2} &= \frac{3nJ_2R_{\oplus}^2}{2a^2} \\ \omega_p &= \frac{3\mu_p}{4na_p^3h_p^3} \\ \omega_{\mathrm{SRP}} &= \frac{\dot{L}_{\odot}\left(1 - \cos\Lambda\right)}{\cos\Lambda} \end{aligned} \tag{4.22}$$

where $\omega_\odot$ and ω_{Moon} are obtained by replacing p in the expression for ω_p, and μ_p, a_p, and h_p are the standard gravitational parameter, semi-major axis, and orbital angular momentum of the third body, except for $h_\odot$ which is the angular momentum of the Earth's orbit around the Sun. The angle Λ characterizes the effect of SRP on the spacecraft and is defined as:

$$\tan\Lambda = \frac{3\gamma}{2}\sqrt{\frac{a}{\mu_\oplus\mu_\odot a_\oplus\left(1-e_\oplus^2\right)}}\gamma = a_{\text{SRP}}\, d_\odot^2 \tag{4.23}$$

where $d_\odot$ is the distance to the Sun, and a_{SRP} is the SRP induced acceleration of the SPS. Table 4.3 compares the effect of SRP force on various SPS designs taken from [2] and includes CASSIOPeiA's baseline design. Clearly, CASSIOPeiA's baseline design is more susceptible to SRP than other designs. The $\omega_\cdot$ quantities have the values:

$$\begin{aligned}\omega_{J_2} &\approx 2.7\times10^{-9}\text{rad/s}\\ \omega_\odot &\approx 4.1\times10^{-10}\text{rad/s}\\ \omega_{\text{Moon}} &\approx 8.9\times10^{-10}\text{rad/s}\\ \omega_{\text{SRP}} &\approx 1.2\times10^{-10}\text{rad/s}\end{aligned} \tag{4.24}$$

Table 4.3: Area to mass ratios and values of Λ for various SPS designs. All values except for those for CASSIOPEIA are taken from [2].

SPS	A/m $[\text{m}^2/\text{kg}]$	Λ [°]
Cylindrical	0.15	0.12
Abacus	0.40	0.33
ISC	0.87	1.09
CASSIOPeiA	3.1	2.02

From Eq. (4.20), and making $\mathbf{h}$ correspond to a circular GEO orbit, we get from the magnitude of vector $\boldsymbol{\omega}_h$ that the orbital plane precesses with a period of approximately 50 years, which does match the numerical results that we obtained. This is an approximation, since it ignores the variation of $\mathbf{h}$. The Laplace plane is defined as the plane where an orbit does not precess as a result of the J_2 and third body effects. In [12], Eq. (4.20) is used to find the modified Laplace plane, which accounts also for the precession caused by the SRP effect. The higher Λ is, the closer this plane will be to the ecliptic plane. In our case, the inclination relative to the equatorial plane is of $7.87°$, which means an ecliptic inclination of $i = 15.5°$.

McNally [2] suggests placing an SPS in a GLPO. There are many advantages in placing an SPS in this plane, such as lower orbital and attitude control costs, as will be discussed. We performed some of our analyses for both GEO and GLPO, but in some cases only GEO was considered as that is usually the more pessimistic case.

For the in-plane effects, the discussions in the literature referenced above show that the SRP effect is by far the dominant one. To analyse these in-plane effects, the equinoctial elements were found to be more useful, where this effect is seen in the variation of P_1 and P_2. The SRP acceleration is written in the equinoctial frame, from which:

$$\begin{aligned}a_{\text{SRP},R} &= a^f_{\text{SRP}}\cos L + a^g_{\text{SRP}}\sin L\\ a_{\text{SRP},T} &= -a^f_{\text{SRP}}\sin L + a^g_{\text{SRP}}\cos L\\ a_{\text{SRP},N} &= a^h_{\text{SRP}}\end{aligned} \tag{4.25}$$

Note: inputting $a_{\text{SRP},N}$ into Eq. (A.4) would result in zero variation in Q_1 and Q_2 suggesting no precession. As explained in [12], this is a misleading result, as a precession does occur, due to an interaction with the in-plane effects from the

SRP.

To account for the movement of the Earth around the Sun, we write $\mathbf{a}_{\text{SRP}} = a_{\text{SRP}} \left(\mathbf{a}_{\text{SRP},C} \cos L_{\odot} + \mathbf{a}_{\text{SRP},S} \sin L_{\odot} \right)$. Introducing this into the equations for P_1 and P_2, averaging, and approximating to within $O(e^2)$, results in:

$$\begin{aligned} P_1 &\approx P_{10} + k_{\text{SRP}} \left(\mathbf{a}^{f}_{\text{SRP},S} \cos L_{\odot} - \mathbf{a}^{f}_{\text{SRP},C} \sin L_{\odot} \right) \\ P_2 &\approx P_{20} + k_{\text{SRP}} \left(-\mathbf{a}^{g}_{\text{SRP},S} \cos L_{\odot} - \mathbf{a}^{g}_{\text{SRP},C} \sin L_{\odot} \right) \\ k_{\text{SRP}} &= \frac{3}{2} \sqrt{\frac{a}{\mu}} \frac{a_{\text{SRP}}}{\dot{L}_{\odot}} \end{aligned} \tag{4.26}$$

The phase plot would show P_1 and P_2 drawing an ellipse over a year centered in the integration constants (or “mean elements") P_{10} and P_{20}. When we have an ecliptic orbit, $Q_1 = Q_2 = 0$, this becomes a circle of radius k_{SRP}. If $P_{10} = P_{20} = 0$, the eccentricity would be constant and equal to k_{SRP} while the argument of pericentre is equal to $L_{\odot}$. As such, without significant propellant costs, it is not possible to keep the eccentricity equal to zero throughout a whole year, as it will always reach at least k_{SRP} at some point in the year.

4.4 Orbital Control

The requirements driving any possible orbital control are limiting the drift in the position of the SPS above the Earth, and in keeping the elevation angle of the microwave beam from the SPS below its limits, as stipulated in [5], of ±39° for a maximum 3dB losses.

To check if orbital control really is required, we performed a numerical simulation, where the perturbations in bold in Tables 3.1 and 3.2 were included, in addition to J4. The starting point was for $e = \Omega = 0$ and $i = \epsilon$ and $a = a_{\text{GEO}}$, where:

$$a_{\text{GEO}} = \left(\frac{\mu}{\omega_{\oplus}^2} \right)^{\frac{1}{3}} \tag{4.27}$$

and $\omega_{\oplus}$ is the angular velocity of the Earth’s rotation. The simulation was carried out over 50 years as that was found to be roughly the period of the orbit precession, and is the same integration time chosen by McNally [2]. Some results are shown in Figure 4.4 for equatorial orbital parameters. These results match closely those reported in [2].

Because of the various perturbations, an orbit with Semi-Major Axis (SMA) given by Eq. (4.27) is not exactly geosynchronous, as $\dot{L}$ differs from its value for a Keplerian orbit, and the orbit does not stay equatorial even if it starts this way. This results in a drift that greatly accumulates over the years, but can be easily cancelled by adjusting the SMA. Let λ_G and ϕ_G be the Geocentric longitude and latitude respectively. On average, i.e. ignoring the effect of eccentricity and inclination, we have $\dot{\lambda}_G = \dot{L}_p + n - \omega_{\oplus}$, where $\dot{L}_p$ is the result from perturbations. We estimate $\dot{L}_p$ from our simulations and solve $\dot{\lambda}_G = 0$ for n, which gives the new semi-major axis that we call $\tilde{a}_{\text{GEO}}$. The difference $\tilde{a}_{\text{GEO}} - a_{\text{GEO}}$ is of around -3.3km. All subsequent simulations were performed with $a = \tilde{a}_{\text{GEO}}$.

For an orbit at inclination i with respect to the ecliptic, the microwave beam elevation angle will have an absolute value of at most $i + \arcsin\left(R_{\oplus}/R_c\right)$, where the first term is the maximum angle between the SPS’s nadir direction and the ecliptic plane, while the second term is the maximum angle between the nadir direction and a vector pointing from the SPS to the ground station on Earth. This represents a worst case scenario, where $\theta = \pm\pi/2$ and the SPS has drifted to the point where the ground station is just about to stop being visible from the SPS. For GEO this worst case value never exceeds $32°$ and for GLPO it never exceeds $26°$, both cases being well within the maximum of $39°$. Therefore,

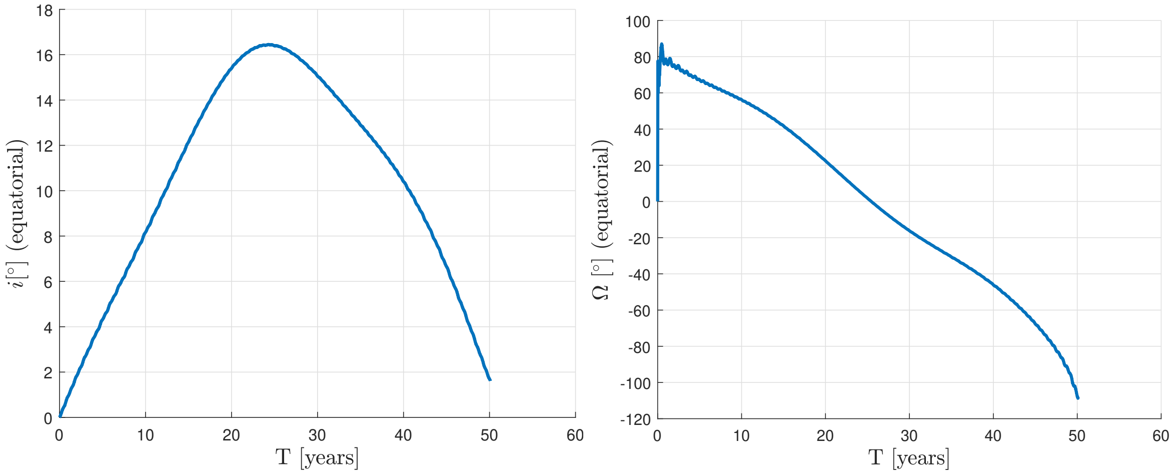

a: Inclination vs time

b: RAAN vs time

Figure 4.4: Values of equatorial i and Ω for GEO orbit shown over a period of 50 years. Results match those found in [2].

orbital control is not strictly required in order to keep the microwave beam angle within its limits, provided that the microwave beam is steerable.

4.4.1 Controlled GEO

To keep the longitude and latitude drifts close to zero, the eccentricity and equatorial inclinations would both have to be kept equal to zero by application of control thrust.

In order to maintain $e = 0$, an estimate of the propellant requirement can be made, assuming instantaneous impulses at pericenter and apocenter are made each orbit to counter the yearly eccentricity drift, resulting in 340.5 m/s/year and 13.9 tonnes/year of propellant consumed. These values are over-optimistic, since the assumption of instantaneous impulses does not hold. It would take more than 17 hours per day to perform that delta-v, which is more than half the orbit, at a thrust level of around 30 N. Instead, it is more realistic to follow Roithmayr [3] and cancel the SRP acceleration directly, which would require 452.85 m/s/year, or 18.5 tonnes/year. In either case, we have a significant increase in propellant costs and as such it is probably best to allow some longitude drift to occur.

The formula in [13] was used to find the required delta-v to cancel the variation of inclination found throughout the orbit (obtained by simulating the orbit without allowing the elements to vary). This results in a delta-v of 53 m/s/year, which is in line with the value proposed by Roithmayr [3], and a consumption of 2.4 tonnes/year of propellant. This can be partly controlled at the same time as the attitude, but not totally, since the required moment can be zero at the same time as inclination control is required. A more thorough study on the placement of the thrusters for combined attitude and inclination control could be the subject of further study. It is noted, however, that for a GLPO orbit the inclination variation would be much smaller, possibly negating the need for inclination control. However, a GLPO orbit would require a non-equatorial orbit and would therefore result in some latitude drift. Figure 4.9 shows the amount of drift that can be obtained with limited amount of control.

4.4.2 Zero mean elements

Some reduction in longitude drift and thus in beam elevation angle can be achieved by choosing initial values for P_1 and P_2 such that P_{10} and P_{20} in Eq. (4.26) are zero at the start. Figure 4.5 shows a phase plot of these variables for the case where we start with zero eccentricity, and for the case where we start with the values required to make $P_{10} = P_{20} = 0$, which are found by making:

$$\begin{aligned} P_1(t=0) &= k_{\text{SRP}}\left(\mathbf{a}^{f}_{\text{SRP},S}\cos L_{\odot,0} - \mathbf{a}^{f}_{\text{SRP},C}\sin L_{\odot,0}\right) \\ P_2(t=0) &= k_{\text{SRP}}\left(-\mathbf{a}^{g}_{\text{SRP},S}\cos L_{\odot,0} - \mathbf{a}^{g}_{\text{SRP},C}\sin L_{\odot,0}\right) \end{aligned} \tag{4.28}$$

where $L_{\odot,0}$ is $L_\odot$ at $t = 0$. A result of this is that the maximum eccentricity is much lower (see Figure 4.6) which, in turn, results in lower drift (see Figure 4.7) and a lower maximum torque, as the pericentre is at a higher altitude. Whilst making $P_{10} = P_{20} = 0$ results in a lower yearly variation of the longitude drift, the majority of this drift has a longer periodic variation (matching the precession of the orbital plane) and, as such, this on its own does not significantly reduce the overall longitude drift.

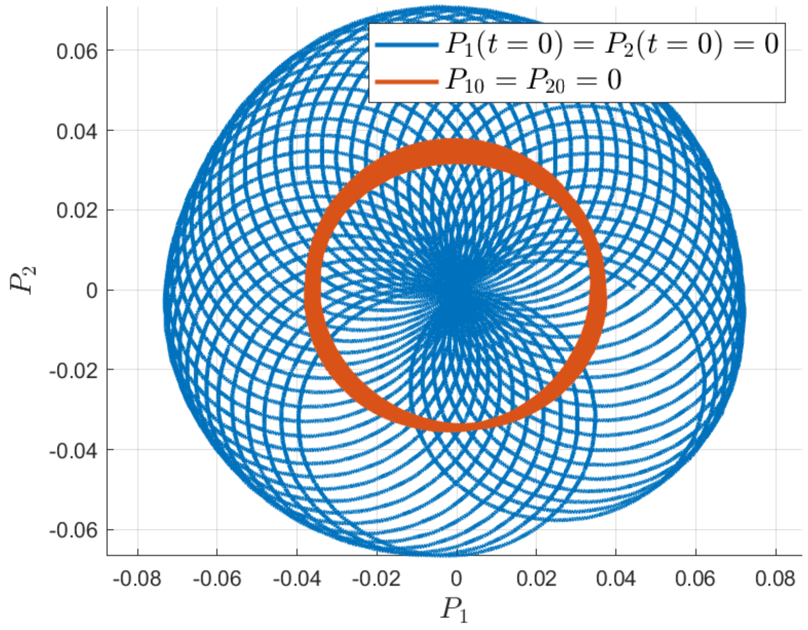

Figure 4.5: Phase diagram of P_1 and P_2 for GEO orbit, showing results of making $P_1(t = 0) = P_2(t = 0) = 0$ versus making $P_{10} = P_{20} = 0$. The latter results in much smaller maximum eccentricities, of approximately half the value.

4.4.3 Feed-back Control of Longitude Drift

The longitude drift caused by the orbital eccentricity can be estimated as $\lambda_G = 2e$ [3] (in radians), which is close to the short periodic component of λ_G shown in Figure 4.7. Bringing the longitude drift down to zero would require making the eccentricity constant and equal to zero, which, as explained previously, requires almost cancelling the SRP force with thrusters. However, by making small tangential manoeuvres to increase or decrease the SMA, it is possible to greatly reduce the longitude drift without a significant amount of propellant (at least, when compared with the requirements for attitude control). This would leave only the short periodic variation in longitude due to eccentricity, which we already

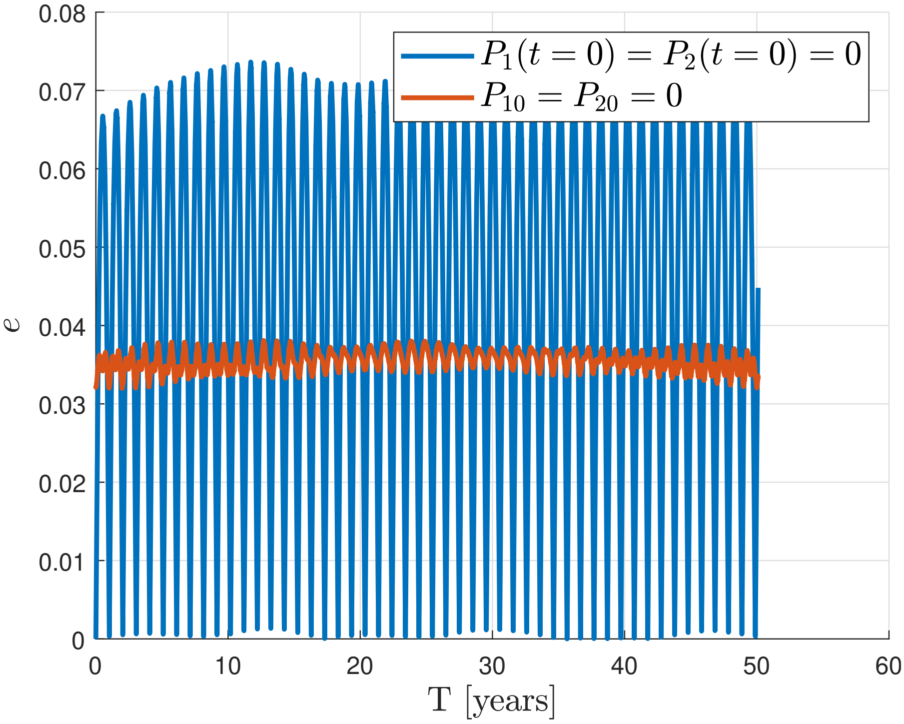

Figure 4.6: Eccentricity variation showing results of making $P_1(t = 0) = P_2(t = 0) = 0$ versus making $P_{10} = P_{20} = 0$. The latter results in smaller maximum eccentricities, of approximately half the value.

halved by making $P_{10} = P_{20} = 0$. As a simple test we define a simple linear feedback controller, such that $a_T = -k\lambda_G$, and choose k such that the linearised system acts as a high-pass filter tuned to $\omega_\lambda = 100n$, which results in:

$$k = \frac{2}{3} a \omega_\lambda^2 \tag{4.29}$$

For around 3.8 kg/year of propellant, this longitude drift can be significantly reduced as shown in Figure 4.8. Finally, Figure 4.9 shows the longitude and latitude drift for GEO and GLPO when both these techniques are in use.

4.4.4 C22 effect

The tesseral component C22 was not considered in our simulations. It tends to move satellites in GEO towards two stable longitudes of around 75 and 255 degrees. If placed outside the equilibrium locations, a satellite will be subject to tangential forces that lead to small changes in SMA, which in turn leads to longitude drift. This acceleration is at most around 8×10^{-8} m/s^2. Cancelling this acceleration directly, a worst case scenario as it is certainly possible to be more efficient, leads to a propellant cost of 103 kg/year. Using the estimate of 1.74 m/s/year reported by McNally [2] leads to 70 kg/year of propellant. In either case, these propellant requirements are very small compared with the other requirements mentioned so far, in particular those for attitude control that are unavoidable. In addition, this control could be performed simultaneously with the attitude control without extra propellant cost, as with other orbital control manoeuvres.

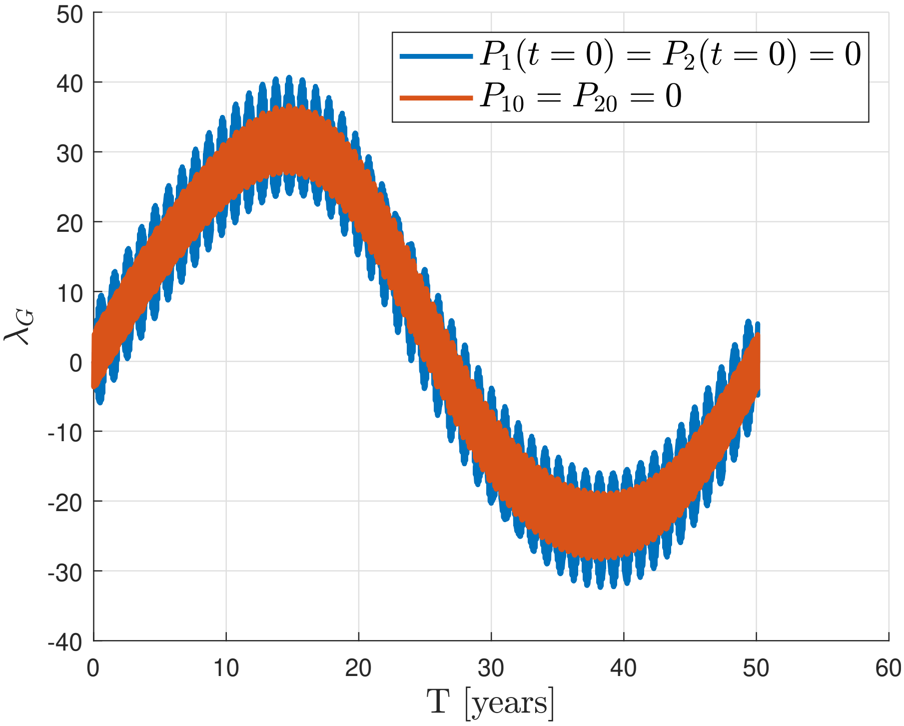

Figure 4.7: Longitude drift over time, comparing the results of having $P_1(t=0)=P_2(t=0)=0$ versus $P_{10}=P_{20}=0$.

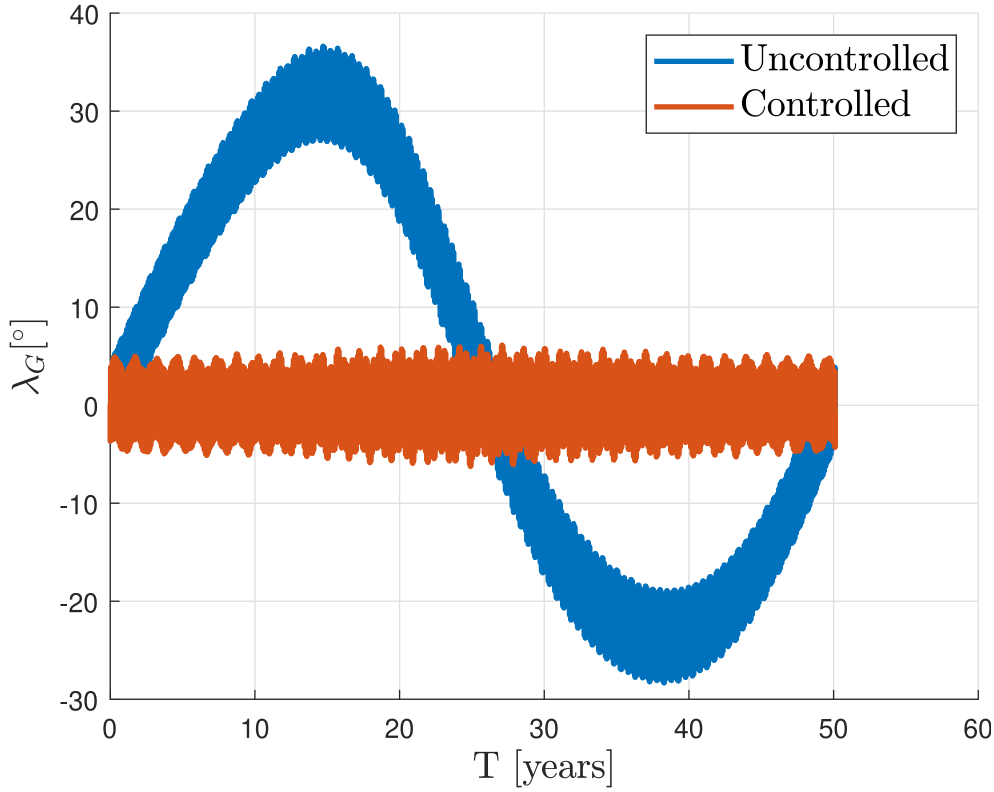

Figure 4.8: Comparison of uncontrolled vs controlled longitude drift. In both cases initial $P_{10}=P_{20}=0$.

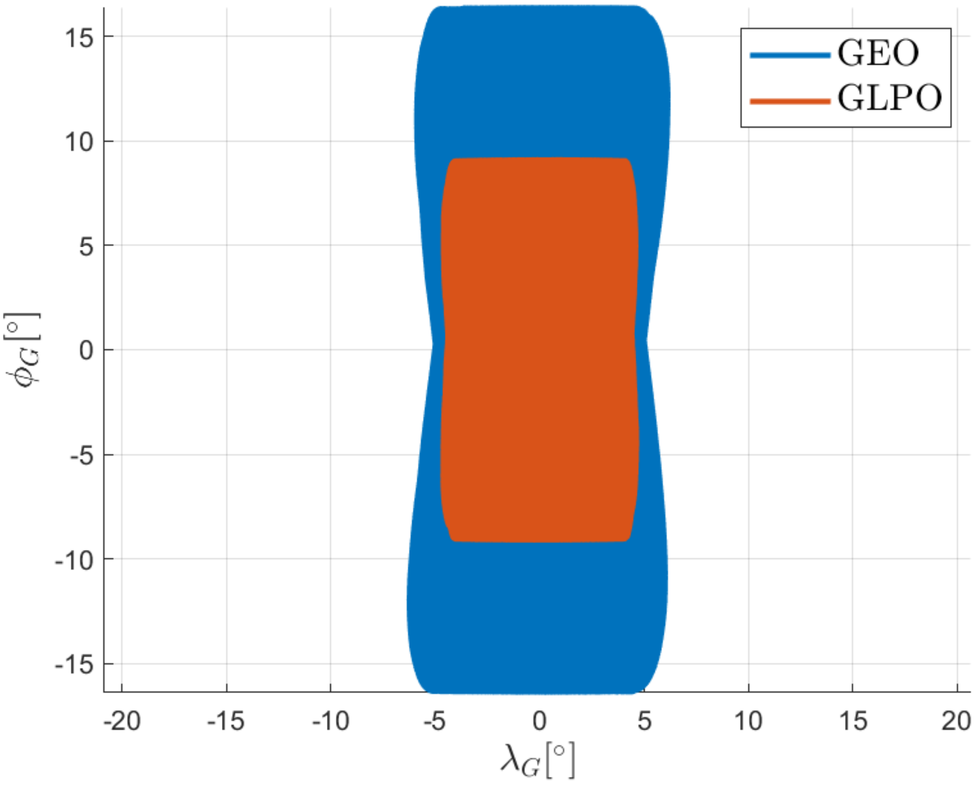

Figure 4.9: Comparison of latitude and longitude drift for GEO vs GLPO. In both cases initial $P_{10} = P_{20} = 0$ and the feedback controller is in use.

5 Finite Element Analysis

This section outlines the development of the Finite Element (FE) Model and the initial analyses performed for the baseline CASSIOPeiA configuration, as an example of a large scale SPS.

Abaqus CAE version 2017 has been used for all pre- and post-processing of the FE model. The model was solved using Abaqus Standard, version 2017.

5.1 Modelling the SPS

The intent of the FE modelling was to capture the predominant global modes of the structure. It was therefore not necessary to accurately represent small local details (such as individual layers of the helix, or individual antennae), provided the overall mass and stiffness distributions were appropriately captured.

5.1.1 Model Mesh

The FE model mesh comprises 7,026 elements and 20,951 nodes. The following sub-sections indicate the element types that were used for each component.

A mesh sensitivity study was performed during the model build process to confirm that further mesh refinement resulted in negligible change of the predicted modal frequencies.

5.1.1.1 Helix

The helix was modelled as a single surface and meshed with 8-noded quadratic shell elements (type S8 elements). Isotropic material properties were assumed and the estimated total mass was smeared uniformly across the surface.

Once design details for the helix have been confirmed, and the relative stiffness of the helix components are known, the model may be developed in the future to use orthotropic material properties that capture the axial, torsional and radial stiffnesses of the helix.

5.1.1.2 Reflectors

The reflectors were modelled as a single surface and meshed with a combination of 8-noded and 6-noded quadratic shell elements (type S8 and STRI65 elements). Isotropic material properties were assumed and the estimated total mass has been smeared uniformly across the reflector surfaces.

5.1.1.3 Structural Beams

The structural beams between the helix and the reflector are currently unknown. In lieu of detailed design information, the arrangement presented in Figure 2.3 was adopted. This support arrangement appropriately constrains all translational and rotational degrees of freedom of the reflectors.

The structural beams were modelled using beam elements (type B31 elements). Fixed joints were assumed at either end of the structural connections (i.e. both moments and forces are transferred).

5.1.2 Boundary Conditions

For the FE modal analyses, a “free-free” system (i.e. no boundary conditions) was assumed. As a result, it is noted that the modal analyses will yield six rigid body modes (i.e near zero frequency) and various flexural modes at finite frequencies. The global flexural modes of the structure are the primary focus of this study.

5.2 Modal Analysis

A modal analysis has been carried out with the objective of identifying the fundamental global modes of vibration of the baseline CASSIOPeiA model and to determine the frequency of those modes.

The frequencies for the first twenty modes are presented in Table 5.1. The first six modes are rigid body modes with a frequency less than 1×10^{-5} Hz; these non-zero frequencies are an artifact of the eigensolver and are therefore meaningless. Mode 7 is the first flexural mode shape for the SPS model with a frequency of 2.25×10^{-3} Hz. This frequency corresponds to a helix mode, where the reflectors rotate about the helix minor axis, as shown in Figure 5.1.

It should be noted that the frequency of the first flexural mode is significant higher (by two orders of magnitude) than the excitation frequency of 2.31×10^{-5} Hz. This indicates that interaction between the orbital load and the global dynamic response of the baseline configuration is not expected to occur. The frequency of the successive modes are higher and therefore they are further separated from the excitation frequency.

Table 5.1: Modal Frequency for the first 20 modes for the baseline CASSIOPeiA Configuration. * indicates rigid body modes

Mode Number	Frequency (Hz)	Time Period (s)	Mode Number	Frequency (Hz)	Time Period (s)
1*	0	/	11	7.3 E-3	137
2*	0	/	12	7.6 E-3	132
3*	0	/	13	8.6 E-3	117
4*	0	/	14	9.1 E-3	109
5*	0	/	15	9.5 E-3	105
6*	0	/	16	9.9 E-3	101
7	2.2 E-3	445	17	10.9 E-3	91
8	2.4 E-3	409	18	11.0 E-3	91
9	3.9 E-3	255	19	11.1 E-3	90
10	3.9 E-3	254	20	11.3 E-3	89

A Rayleigh-type discretisation calculation for the modal natural frequencies of the SPS has been performed, as a sanity check of the approximate correctness of the finite element frequency prediction. This is given, in Hz, by the following expression for the jth mode:

$$f_j = \frac{1}{2\pi}\sqrt{\frac{g\sum_{i=1}^{n} F_i w_i}{sum_{i=1}^{n} W_i w_i^2}} \tag{5.1}$$

Note that g is the local acceleration due to gravity, F_i is the lateral load at the ith node, and w_i is the associated lateral displacement at that node. W_i is the vertical (z) (gravity) load at the ith node. Although this calculation is strictly defined for a terrestrially located structure, it is equally applicable to orbiting structures as the natural in-vacuo frequencies of the structure do not change from the Earth’s surface to extreme orbits. The equation is founded on the relationship between static deflection due to weight (a surrogate for mass) and stiffness.

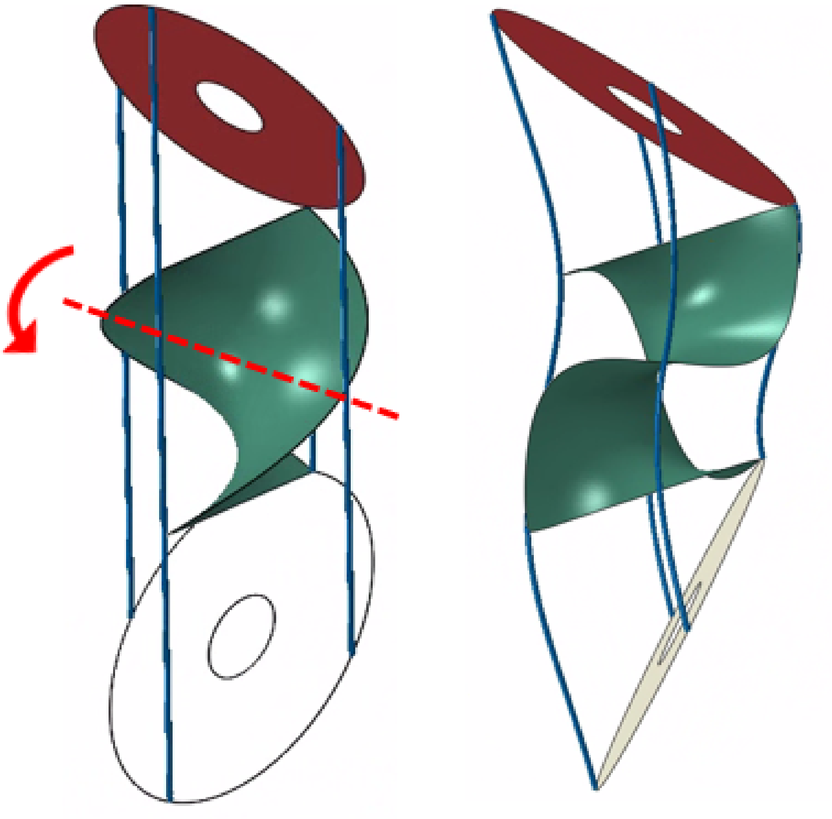

Figure 5.1: Mode shape for the first flexural mode.

This calculation generates a Rayleigh-type prediction of the Mode 7 natural frequency of 2.87x10-3 Hz against the finite element prediction of 2.25x10-3 Hz. Whilst this Rayleigh prediction is 27.5% higher than the finite element prediction, it shows that the finite element model is predicting frequencies of the correct order of magnitude.

5.3 Static Analysis

The following sub-sections summarise the use of the finite element model to assess the deformation of the CASSIOPeiA structure due to the orbital loads.

5.3.1 Forces That Do Not Vary With Orbital Position

The CASSIOPeiA concept is designed such that the reflectors always remain pointing at the Sun. Therefore, the SRP is the only significant force that does not vary with orbital position. The SRP acts on the two reflectors and therefore seeks to bend the helix and structural beams, and cause misalignment of the reflectors. The helix structure sees an equal and opposite force on the top and bottom faces and therefore the net force on the helix due to SRP is zero.

Within the finite element model, the SRP has been applied as a uniform pressure of $4.57 \times 10^{-6}\mathrm{N/m^2}$ acting normal to the surface of the reflectors. A single static analysis has been carried out to assess the deformation of the models due to the SRP.

The contour plots in Figure 5.2 show the resultant displacement and the displacement in the vertical axis $(\mathrm{U3})$ of the SPS model due to the SRP. These contour plots indicate that the maximum displacement of the SPS due to SRP is approximately 0.2 metres. This displacement represents 0.01% of the SPS diameter of 2 km, and is therefore considered negligible. The relative rotation between the two reflectors is negligible (less than 0.1 degrees) and therefore the action of the SRP is not expected to affect the function of the CASSIOPeiA design.

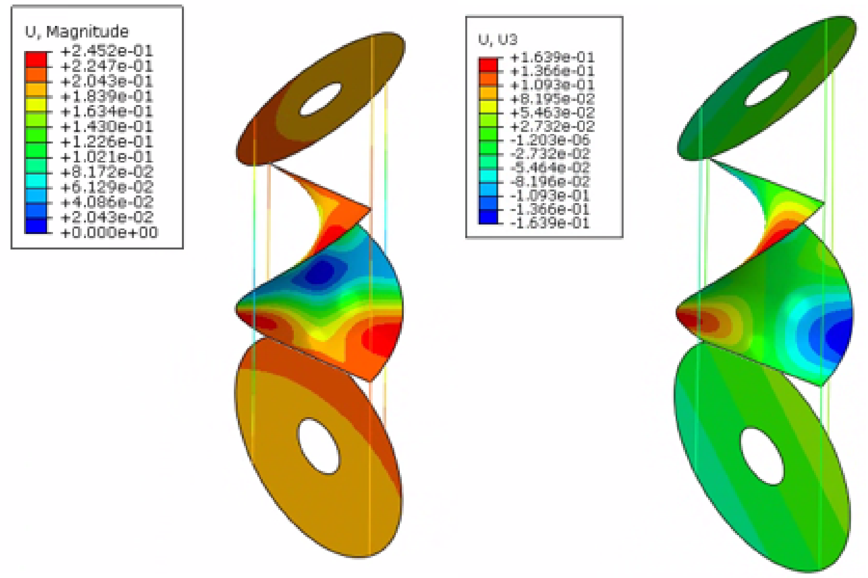

Figure 5.2: SPS deflections due to Solar Radiation Pressure (Displacement magnitude shown on the left, Vertical deflection shown on the right)

5.3.2 Forces That Do Vary With Orbital Position

The most significant forces that do vary with orbital position are gravitational gradient, the microwave force and the thruster forces. Given that the frequency of the first flexural mode differs notably from the excitation frequency, the response of the SPS model to the orbital loads that do vary with orbital position may be assessed with a static finite element analysis.

Within the finite element model, the gravitational accelerations in the three coordinate directions have been applied as a distributed gravitational load to all parts of the model.

As detailed in Section 3.7, the microwave force is the equal and opposite force to the microwaves that are beamed back to Earth. Therefore, the total microwave force of 15 N acts in the opposite direction to the Earth pointing vector and has been applied as a surface traction within the finite element model.

The thruster forces are dependent on similar expressions to the gravity gradient accelerations. For the purpose of this assessment, it has been assumed that the orbital control thrusters would be located at the four corners of the helix. Within the finite element model, the thruster forces have been applied as concentrated loads in the three coordinate directions.

Analyses of the forces that do vary with orbital position have been carried out for 2100 Earth positions (relative to the body frame). This includes 100 equally spaced positions on the local lateral plane, repeated for 21 different equally spaced declinations between -23.4° and +23.4°.

Figure 5.3 shows the relationship between the Earth position and the maximum displacement due to deformation of the SPS model, as a result of the orbital loads that vary with orbital position. The deformation of the SPS model is greatest at the maximum and minimum declinations (+/- 23.4 degrees) and when the Earth pointing vector is aligned with the local x-axis of the model, as shown in Figure 5.3. The maximum displacement predicted is 2.9 m; this maximum displacement occurs at the tip of the reflectors as shown in Figure 5.4 and is driven predominantly by the gravity gradient and thruster forces. The displacement of the reflectors due to the loads that vary with orbital position are larger than that predicted for the SRP, however the displacements represent 0.1% of the SPS diameter of 2 km and are therefore considered negligible.

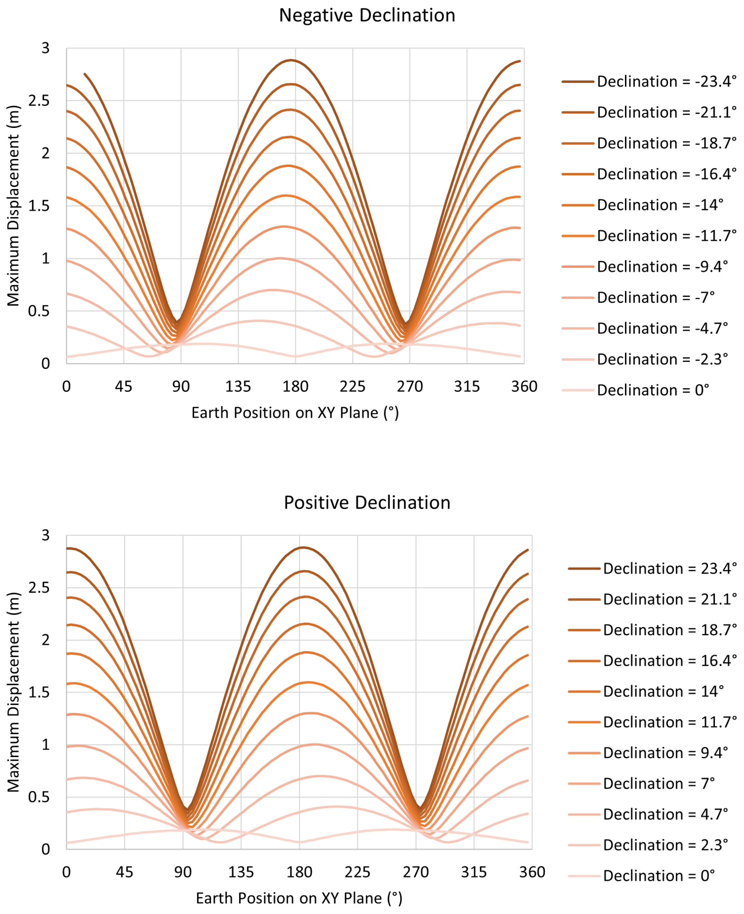

Figure 5.3: Relationship between the maximum displacement of the SPS and the Earth position on the XY plane

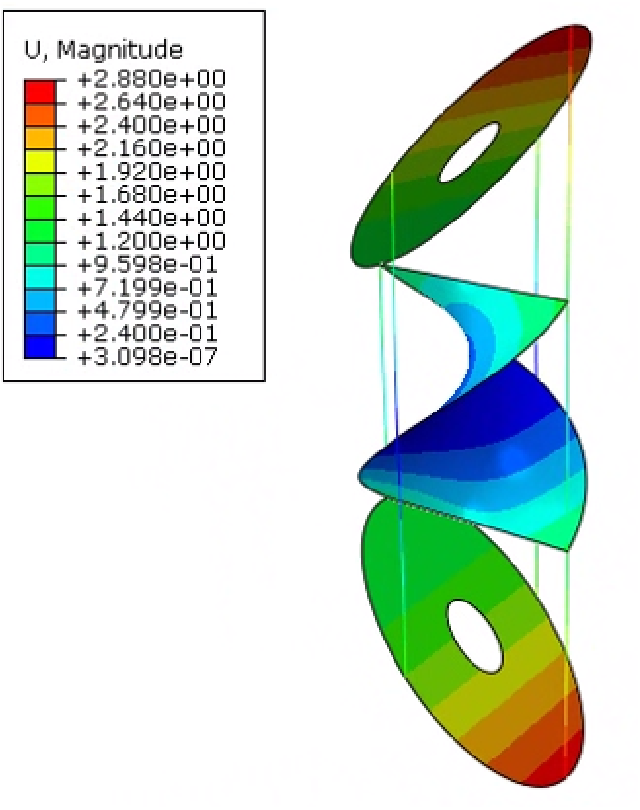

Figure 5.4: SPS deflections due to loads that vary with orbital position

6 Ray Tracing Analysis

As previously discussed, the main effect that can cause an orbital perturbation of the SPS due to structural deformations is the SRP force. As the SPS is distorted, the light rays coming from the Sun get reflected in different directions, and some may end up missing the helix structure, that they otherwise would have hit. This is best assessed by performing a ray tracing analysis, in which rays from the Sun and their reflected paths are simulated, to see whether they hit the helix, or go into free space. Furthermore, this investigation will also produce a measure of the pointing accuracy of the SPS when subject to orbital loads, by estimating the efficiency of the SPS, measured by the fraction of rays that continue to hit the helix after distortion.

6.1 Set-up

The non-deformed mesh produced by Abaqus, contained in a .inp file, is first loaded into MATLAB. It is composed of predominantly non-triangular elements, namely S8R elements. To simplify this analysis, the mesh was converted into a triangular mesh, by converting each of those elements into simple 3-noded triangles.

Then, for each static/modal analysis, the .rpt file containing the displacement of each node was read. An initial analysis of the deformed SPS from the static analysis produced two conclusions. The first was that the reflectors remain approximately flat, albeit slightly rotated. This allows a computational cost saving strategy to be used, as described in Section 6.3. The second conclusion was that the maximum angle of rotation of the reflectors was approximately 0.02 degrees. Figure 6.1 shows these results, and reinforces the belief that a harmonic model is likely to be suitable for this application, as it clearly presents a smooth periodic shape.

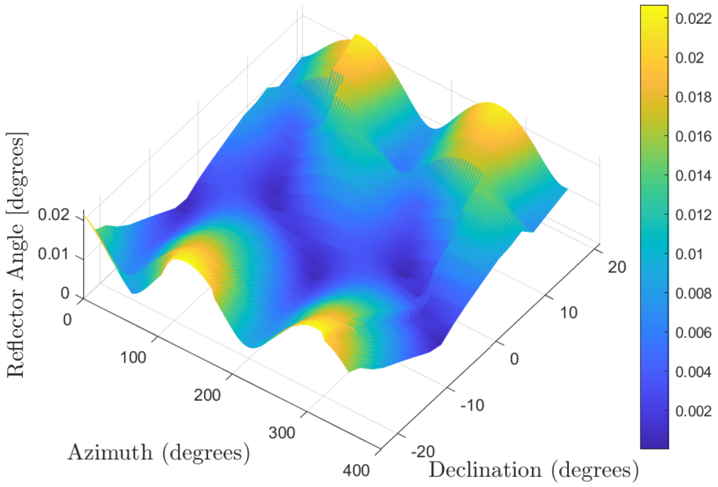

Figure 6.1: Angle of rotation of the bottom reflector plotted against the azimuth and declination of the SPS-Earth vector.

6.2 Basic Methodology

The normal vectors $\hat{\mathbf{n}}_i$ of each element i of the reflectors are then computed. The reflectors are modelled as being a perfectly specular surface, so when a ray coming from direction $\hat{\mathbf{s}}$ hits element i of the reflector, the reflected ray has direction $\hat{\mathbf{d}}_i$, which is given by:

$$\hat{\mathbf{d}}_i = \hat{\mathbf{s}} - 2\left(\hat{\mathbf{s}} - \left(\hat{\mathbf{n}}_i^T\hat{\mathbf{s}}\right)\hat{\mathbf{n}}_i\right) \tag{6.1}$$

It is assumed that the SPS always has its X axis pointing towards the Sun, as a result of the attitude control described previously, and as such $\hat{\mathbf{s}} = [1,\ 0,\ 0]^T$. Each ray is then followed along direction $\hat{\mathbf{d}}_i$ from the point where it hits the reflector, $\hat{\mathbf{p}}_i$, to check if it hits any mesh element of the helix. This is done by first finding the point where the ray intersects the plane of the mesh element, and then by checking if that point fell within the mesh element itself. Rays that hit the helix are assumed to be fully absorbed. In reality, there would be a mixture of specular and Lambertian absorption, but this would require a more detailed design. Rays that miss the helix are at present assumed to not hit the other reflector to speed up the ray tracing. This is because the initial results were showing that the rays that missed the helix were also missing the other reflector. For more extreme cases of structural deformation, this assumption should be revisited.

Following this ray tracing approach for every mesh element of the helix would be too time consuming, and also unnecessary. Instead, the mesh elements that are too far away from the ray to be hit by it are pruned using a KD-tree, as explained in Section 6.3. We first looked at a ray sampling method, described in Section 6.4. This first method, however, was not very efficient, taking too long to produce low accuracy results. This is because the majority of the perturbation γ is due to the rays that miss the helix, which are very much the minority (0.06% at most). A different approach is presented in Section 6.5 that deals with this issue more efficiently.

If the area of each mesh element is termed A_i, the amount of light that hits it is proportional to $\left(\hat{\mathbf{n}}_i^T\hat{\mathbf{s}}\right)A_i$. The force resulting from each ray depends on whether it is absorbed by the helix or not. If so, it is assumed that the momentum carried by that ray is absorbed. Otherwise, it is the difference in momentum from the departing ray to the arriving ray that is the force. The SRP force resulting from ray i, $\mathbf{f}_{\mathrm{SRP,i}}$, is given as [6]:

$$\mathbf{f}_{\mathrm{SRP,i}} = \begin{cases} -p_{\mathrm{SRP}}\left(\hat{\mathbf{n}}_i^T\hat{\mathbf{s}}\right)A_i\hat{\mathbf{s}} & \text{if ray } i \text{ absorbed} \\ -2p_{\mathrm{SRP}}\left(\hat{\mathbf{n}}_i^T\hat{\mathbf{s}}\right)^2 A_i\hat{\mathbf{n}} & \text{otherwise} \end{cases} \tag{6.2}$$

Since the nominal SRP force is given as $\mathbf{F}_{\mathrm{SRP,0}} = -p_{\mathrm{SRP}}\cos\pi/4\sum_i A_i\hat{\mathbf{s}}$, the non-dimensional perturbation from the SRP force, γ, is given as:

$$\gamma = \frac{\sum_i \mathbf{f}_{\mathrm{SRP,i}} - \mathbf{F}_{\mathrm{SRP,0}}}{|\mathbf{F}_{\mathrm{SRP,0}}|} \tag{6.3}$$

6.3 KD-Tree Based Pruning

The Solar rays are assumed to be parallel. Taking the mean value of $\hat{\mathbf{d}}_i$, $\overline{\mathbf{d}}$, the maximum angle ϵ between $\hat{\mathbf{d}}_i$ and $\overline{\mathbf{d}}$ was found to be less than $\epsilon_{\max} = 8\times10^{-5\circ}$. The distance between any ray and one departing from the same point with direction $\overline{\mathbf{d}}$ will be $\rho = \lambda\cos\epsilon_i$, and its maximum value is termed $\rho_{\max}$.

Let the length of the j-th side of the i-th mesh element be termed L_{ij}, and let L_i be the maximum of the three sides. Because the mesh elements are all triangles, L_i is also their effective diameter. If any point of a triangle, including its CoM, is further from a ray than L_i, they cannot be hit by this ray. Therefore, all triangles that are further from the mean ray than $L_{\max} + \rho_{\max}$ cannot be hit by this ray and can be safely pruned, as illustrated in Fig. 6.2.

A KD-tree is a data structure, with associated algorithms, that, given two point clouds P and Q, allows efficiently finding those points in Q that are within a threshold distance to each point in P [14]. If P contains the ray origin points and Q the CoMs of the mesh elements of the helix, both projected to a plane normal to the mean ray direction, the Eucledian distance between these points will correspond to q_i in Figure 6.2, i.e., the distance between an element's CoM and the mean ray.

Therefore, the KD-tree is generated on points P using MATLAB's *KDTreeSearcher*, followed by a maximum range search on points Q with threshold $L_{\max} + \rho_{\max}$ using MATLAB's *rangesearch*.

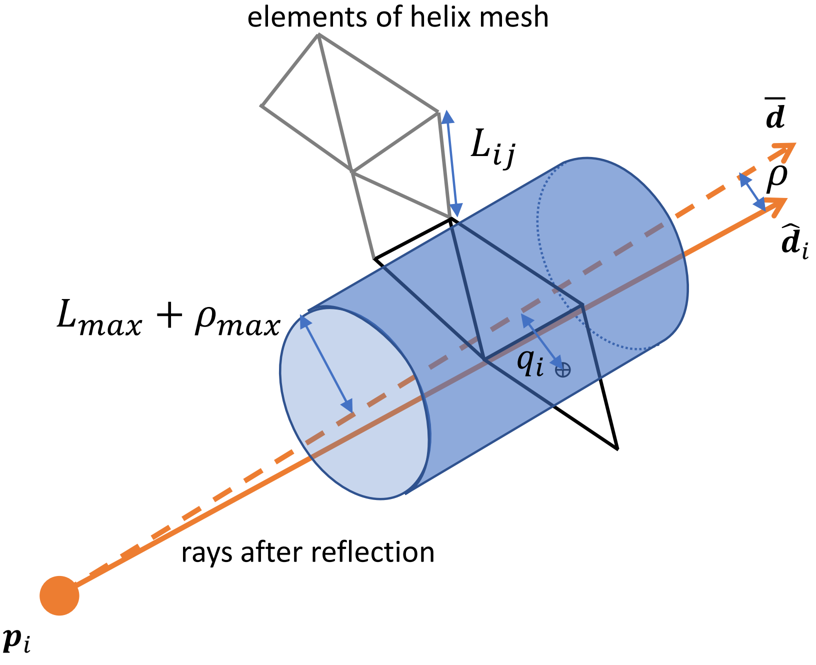

Figure 6.2: Diagram of the criteria for pruning mesh elements that cannot be hit by a ray departing from $\mathbf{p}_i$ with direction $\hat{\mathbf{d}}_i$

6.4 Ray Sampling Method

The first method tested was based on sampling the centres of each mesh element on the reflectors. However, as mentioned, the rays that miss the helix are a very small minority. Nonetheless these rays contribute the most to the value of γ, this resulted in poor quality results. An attempt to ameliorate this problem was to instead sample the rays at the vertices of the reflector meshes, and then sample more finely the mesh elements that include rays that miss the helix. However, even with a very large number of ray samples, the resulting curve was not smooth due to inaccuracies, see Figure 6.3.

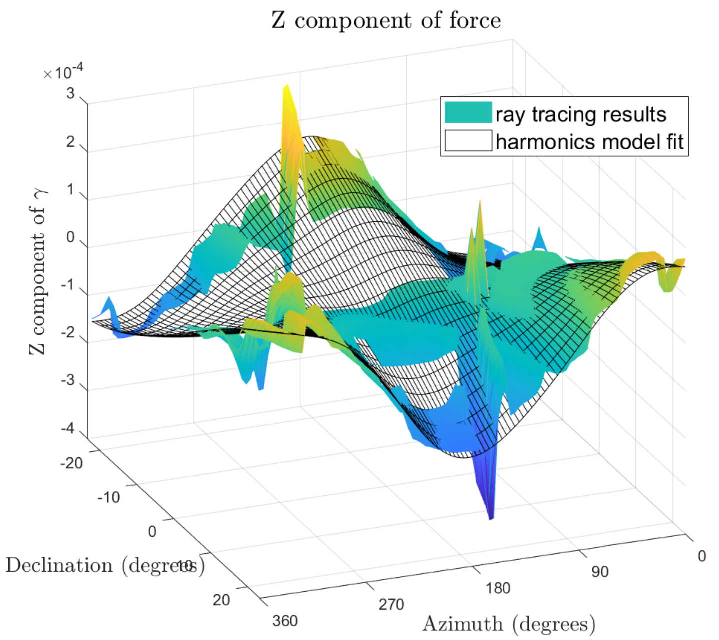

Figure 6.3: Value of γ^z plotted against the azimuth and declination of the SPS-Earth vector.

6.5 Polygon Clipping Method

To solve the problem previously mentioned, a different approach was used. Instead of ray sampling, polygon clipping algorithms were used. Each element of the reflector mesh is projected onto the plane perpendicular to the ray direction $\hat{\mathbf{d}}_i$, as well as the helix mesh elements resulting from the pruning in the previous slide. The projected mesh of helix elements is subtracted from the reflector element, producing area $A_{m,i}$, as shown in Figure 6.4. The ratio $A_{m,i}/A_i$ is the fraction of rays that miss the helix. The calculation of $\mathbf{f}_{\mathrm{SRP,i}}$ becomes:

$$\mathbf{f}_{\mathrm{SRP,i}} = -p_{\mathrm{SRP}}\left(\left(\hat{\mathbf{n}}_i^T\hat{\mathbf{s}}\left(A_i - A_{m,i}\right)\right)\hat{\mathbf{s}} + 2\left(\hat{\mathbf{n}}_i^T\hat{\mathbf{s}}\right)A_{m,i}\right) \tag{6.4}$$

Some small adjustments to the previous method are also necessary. The point cloud P used in the KD-tree pruning is now based on the CoMs of the elements of the reflector meshes, and the threshold distance becomes $2L_{\max} + \rho_{\max}$, since we are now looking at the overlaps of two triangles.

The results obtained in this way look like a smooth function, that is well approximated by the harmonic model previously introduced, as shown in Figure 6.5.

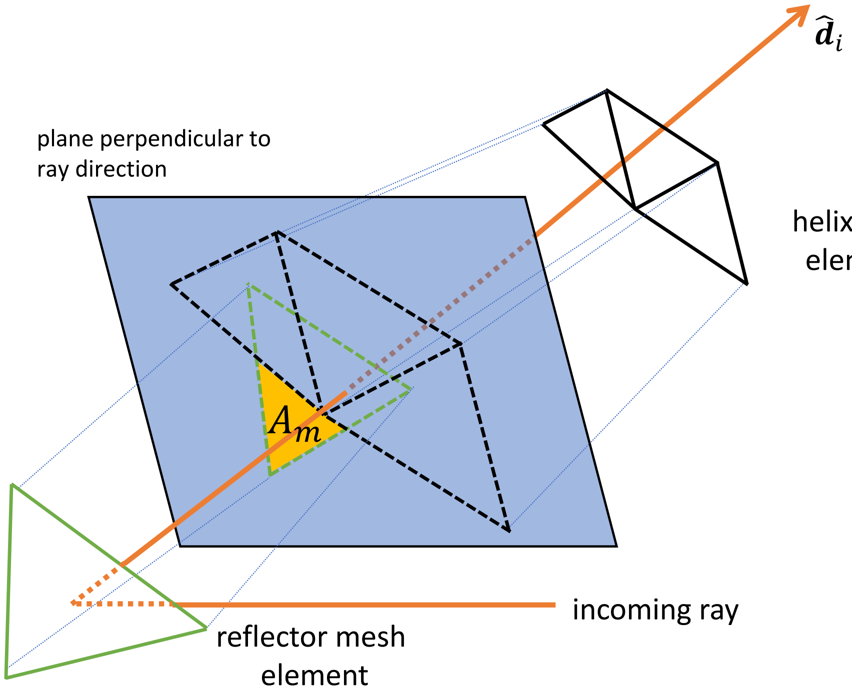

Figure 6.4: Diagram of polygon clipping ray tracing method

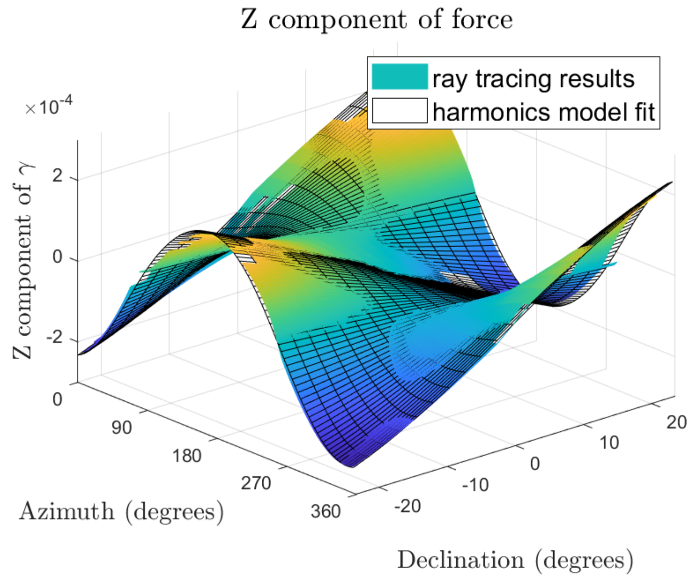

Figure 6.5: Value of γ^z plotted against the azimuth and declination of the SPS-Earth vector.

7 Parametric Study

A parametric study has been undertaken with the objective of investigating trends in the dynamic response of the SPS structure for a range of design parameters. The following sub-sections outline the process followed in selecting a range of appropriate design parameters and the corresponding trends in the dynamic modal response of the SPS structure.

7.1 Parametric Study Approach

The approach that was followed in this parametric study utilised the two analytical toolsets developed as part of this project. Initially, the finite element model of the SPS was used to run a set of modal analyses from which trends in the dynamic response were identified. The modal analysis results were used to determine what variation in the design parameters would be required to align the frequency of the first flexural mode with the excitation frequency. Secondly, the perturbation analysis toolset was used to perform a stability analysis and therefore quantify the potential disturbance to the SPS orbit.

The process by which the two analytical toolsets were used to investigate trends in the dynamic response of the SPS and then perform a stability analysis to quantify the potential disturbance to the SPS orbit is shown in Figure 7.1.

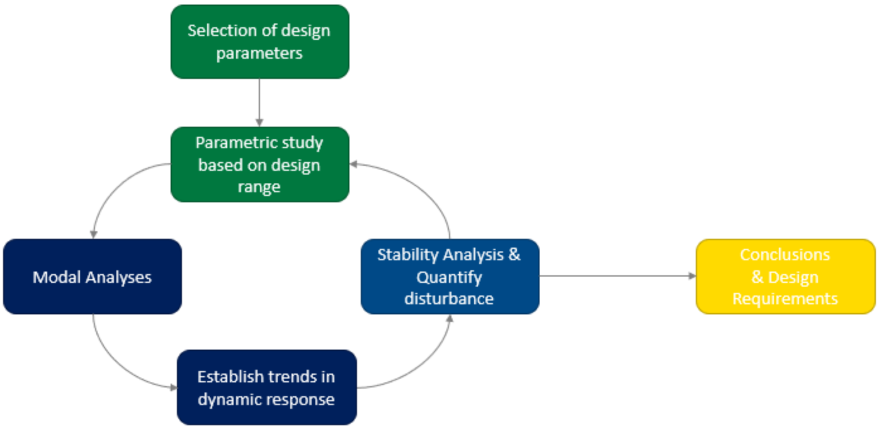

Figure 7.1: Parametric study overview.

7.2 Selection of Design Parameters

The finite element model of the CASSIOPeiA SPS concept features a simplified structural representation of the CASSIOPeiA concept, and therefore basic design parameters such as mass, mass distribution and component stiffness have been considered as part of this parametric study.

Consideration of other leading SPS concepts formed the first part of selecting the range of design parameters that should be assessed. In addition to CASSIOPeiA, the review included SPS-Alpha, MR-SPS, NASA's Sun Tower and various JAXA concepts. There are significant differences between the concepts in terms of architecture and mode of operation. However, the purpose of this review was to quantify the main structural aspects, such as mass, mass distribution and total length, to identify common aspects between the leading SPS concepts, such that the conclusions of our study may be applied to other SPS concepts.

Table 7.1: Summary of Solar Power Satellite Concepts

Concept	Mass (Tonnes)	Length (km)	Orbit	Mass Distribution
SPS-Alpha	8,000	13	GEO	Located at the ends
CASSIOPeiA	1,500	6	GEO / GLP	Focused in the centre
MR-SPS	10,000	12	GEO	Uniform
NASA Sun Tower	6,000	15	GEO	Uniform

A summary of the structural aspects is provided in Table 7.1.

CASSIOPeiA was identified as being notably smaller than the other concepts, with a total length of 6km, compared against the 15km length of the NASA Sun Tower. In addition, CASSIOPeiA has the smallest total mass of 1,500 tonnes, compared against the 10,000 tonnes mass of MR-SPS. This highlighted the need to consider increasing both the length and the mass of the SPS model in order to consider the likely behaviour of the longer and heavier concepts.

It was also noted that CASSIOPeiA presents a compact design in which the majority of the mass is located at the core of the SPS, in the helix structure. The CASSIOPeiA reflectors have a combined mass of only 300 tonnes, which accounts for approximately 15% of the total SPS mass. This is in stark contrast to a concept such as SPS-Alpha, for which the mass is located in the motorised heliostats (mirrors) and the antennae at opposite ends of the 13km long structure. Linear arrangements such as MR-SPS, represent a middle ground in terms of mass distribution, in which the mass is distributed relatively evenly along the length of the SPS structure. This highlighted the need to consider adjusting the mass distribution to have mass focused at either end of the SPS structure.

Given the lack of structural design maturity for many of the concepts, it is difficult to compare the stiffness of the various SPS concepts. As detailed in Section 2, an initial structural design and a corresponding set of component stiffnesses have been established for the purpose of this study, based upon the anticipated component construction. Given the potential for significant changes to be made to the structural arrangement of different SPSs, there is a need to consider both an increase and decrease in the stiffness of the model components.

The baseline modal analysis results were also considered when selecting the range of design parameters for assessment. As detailed in Section 5.2, for the baseline model configuration, the first flexural mode has a predicted frequency of 2.25×10^{-3} Hz. This modal frequency is two orders of magnitude higher than the known excitation frequency of 2.31×10^{-5} Hz. Therefore, in order to investigate the potential coupling between the orbital mechanics and structural dynamics of an SPS structure, it was considered preferable to vary the design parameters to target a reduction of the flexural modal frequency, and therefore bring it in line with the excitation frequency.

For example, mass is inversely proportional to the natural frequency of a system and therefore only an increase in total mass will be considered in this parametric study. Similarly, the length of a beam type structure is inversely proportional to the natural frequency of a system and therefore only an increase in the SPS length will be considered in this study.

In summary, the following parameters ranges have been considered in the set of modal analyses:

- Total Mass: varied from 2,000 to 100,000 tonnes (baseline mass of 2,000 tonnes).
- Mass Distribution: Proportion of mass in the reflectors varied from 15% to 80% (baseline proportion of 15%).
- Total Length: varied from 6 to 24 km (baseline length of 6 km)
- Helix Stiffness: varied from 0.02 GPa to 20 GPa (baseline stiffness of 0.02 GPa)
- Reflector Stiffness: varied from 0.02 GPa to 200 GPa (baseline stiffness of 200 GPa)

- Structural Beam Stiffness: varied from 2 GPa to 2000 GPa (baseline stiffness of 200 GPa)

For completion, the sets of modal analyses carried out as part of this parametric study are listed in Figure 7.2.

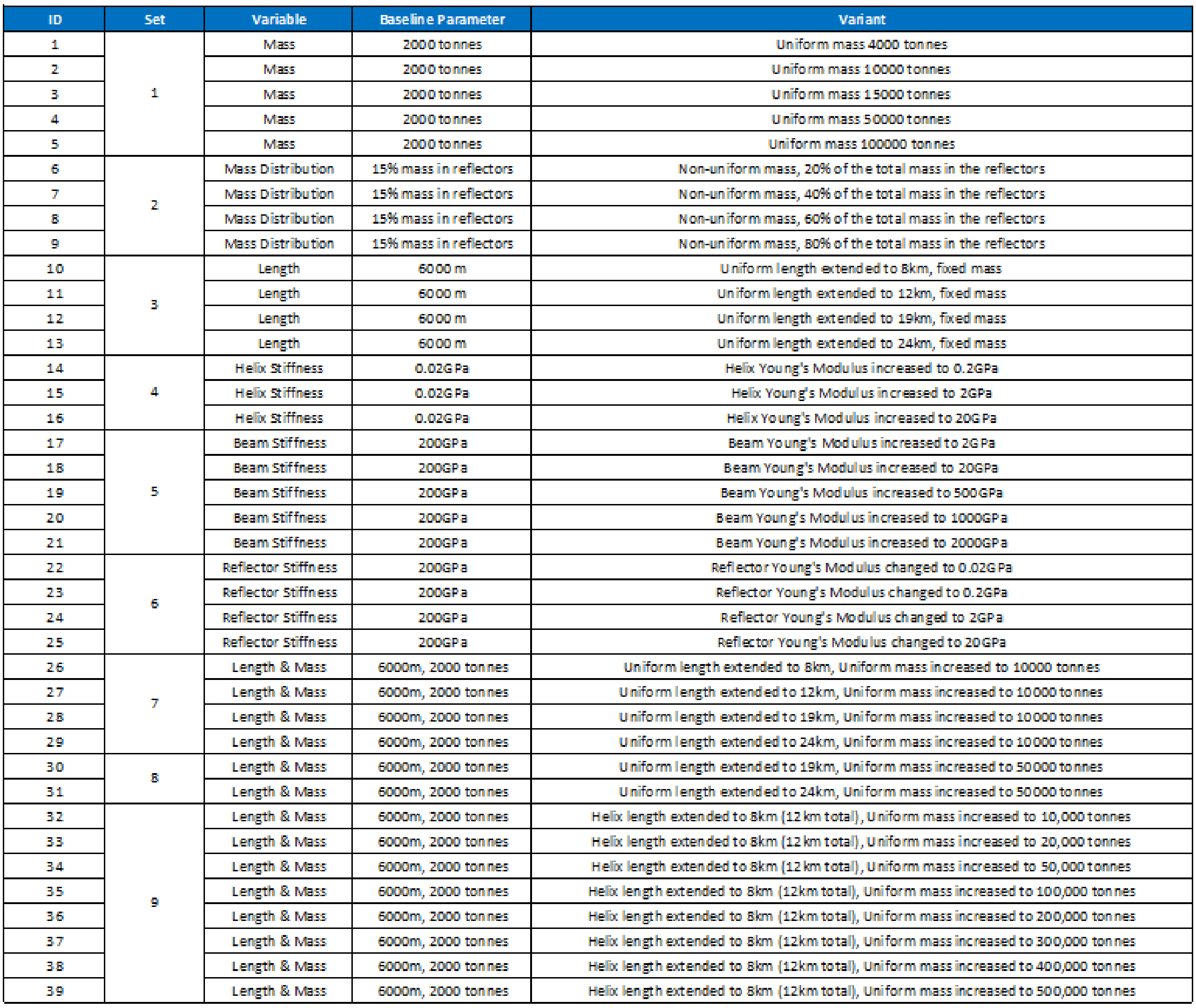

ID	Set	Variable	Baseline Parameter	Variant
1	1	Mass	2000 tonnes	Uniform mass 4000 tonnes
2		Mass	2000 tonnes	Uniform mass 10000 tonnes
3		Mass	2000 tonnes	Uniform mass 15000 tonnes
4		Mass	2000 tonnes	Uniform mass 50000 tonnes
5		Mass	2000 tonnes	Uniform mass 100000 tonnes
6	2	Mass Distribution	15% mass in reflectors	Non-uniform mass, 20% of the total mass in the reflectors
7		Mass Distribution	15% mass in reflectors	Non-uniform mass, 40% of the total mass in the reflectors
8		Mass Distribution	15% mass in reflectors	Non-uniform mass, 60% of the total mass in the reflectors
9		Mass Distribution	15% mass in reflectors	Non-uniform mass, 80% of the total mass in the reflectors
10	3	Length	6000 m	Uniform length extended to 8km, fixed mass
11		Length	6000 m	Uniform length extended to 12km, fixed mass
12		Length	6000 m	Uniform length extended to 19km, fixed mass
13		Length	6000 m	Uniform length extended to 24km, fixed mass
14	4	Helix Stiffness	0.02GPa	Helix Young's Modulus increased to 0.2GPa
15		Helix Stiffness	0.02GPa	Helix Young's Modulus increased to 2GPa
16		Helix Stiffness	0.02GPa	Helix Young's Modulus increased to 20GPa
17	5	Beam Stiffness	200GPa	Beam Young's Modulus increased to 2GPa
18		Beam Stiffness	200GPa	Beam Young's Modulus increased to 20GPa
19		Beam Stiffness	200GPa	Beam Young's Modulus increased to 500GPa
20		Beam Stiffness	200GPa	Beam Young's Modulus increased to 1000GPa
21		Beam Stiffness	200GPa	Beam Young's Modulus increased to 2000GPa
22	6	Reflector Stiffness	200GPa	Reflector Young's Modulus changed to 0.02GPa
23		Reflector Stiffness	200GPa	Reflector Young's Modulus changed to 0.2GPa
24		Reflector Stiffness	200GPa	Reflector Young's Modulus changed to 2GPa
25		Reflector Stiffness	200GPa	Reflector Young's Modulus changed to 20GPa
26	7	Length & Mass	6000m, 2000 tonnes	Uniform length extended to 8km, Uniform mass increased to 10000 tonnes
27		Length & Mass	6000m, 2000 tonnes	Uniform length extended to 12km, Uniform mass increased to 10000 tonnes
28		Length & Mass	6000m, 2000 tonnes	Uniform length extended to 19km, Uniform mass increased to 10000 tonnes
29		Length & Mass	6000m, 2000 tonnes	Uniform length extended to 24km, Uniform mass increased to 10000 tonnes
30	8	Length & Mass	6000m, 2000 tonnes	Uniform length extended to 19km, Uniform mass increased to 50000 tonnes
31		Length & Mass	6000m, 2000 tonnes	Uniform length extended to 24km, Uniform mass increased to 50000 tonnes
32	9	Length & Mass	6000m, 2000 tonnes	Helix length extended to 8km (12km total), Uniform mass increased to 10,000 tonnes
33		Length & Mass	6000m, 2000 tonnes	Helix length extended to 8km (12km total), Uniform mass increased to 20,000 tonnes
34		Length & Mass	6000m, 2000 tonnes	Helix length extended to 8km (12km total), Uniform mass increased to 50,000 tonnes
35		Length & Mass	6000m, 2000 tonnes	Helix length extended to 8km (12km total), Uniform mass increased to 100,000 tonnes
36		Length & Mass	6000m, 2000 tonnes	Helix length extended to 8km (12km total), Uniform mass increased to 200,000 tonnes
37		Length & Mass	6000m, 2000 tonnes	Helix length extended to 8km (12km total), Uniform mass increased to 300,000 tonnes
38		Length & Mass	6000m, 2000 tonnes	Helix length extended to 8km (12km total), Uniform mass increased to 400,000 tonnes
39		Length & Mass	6000m, 2000 tonnes	Helix length extended to 8km (12km total), Uniform mass increased to 500,000 tonnes

Figure 7.2: Matrix of analyses run in the parametric study.

7.3 Trends in Dynamic Response

Various sets of modal analyses have been run to determine the effect of the selected parameters on the modal response frequencies. The trends in the dynamic response are outlined in the following sub-sections.

7.3.1 Mass

Figure 7.3 shows the effect of varying the SPS mass on the frequencies for the first twenty modes. A model mass of 2,000 tonnes represents the CASSIOPeiA baseline configuration. This figure shows that an increase in the SPS total mass has a notable effect on reducing the modal frequencies. For Mode 7, the first flexural mode, the predicted modal frequency is 3.2×10^{-4} Hz for the 100,000 tonnes configuration. Whilst this modal frequency is significantly smaller than that predicted for the baseline model, it remains a factor of 14 greater than the excitation frequency.

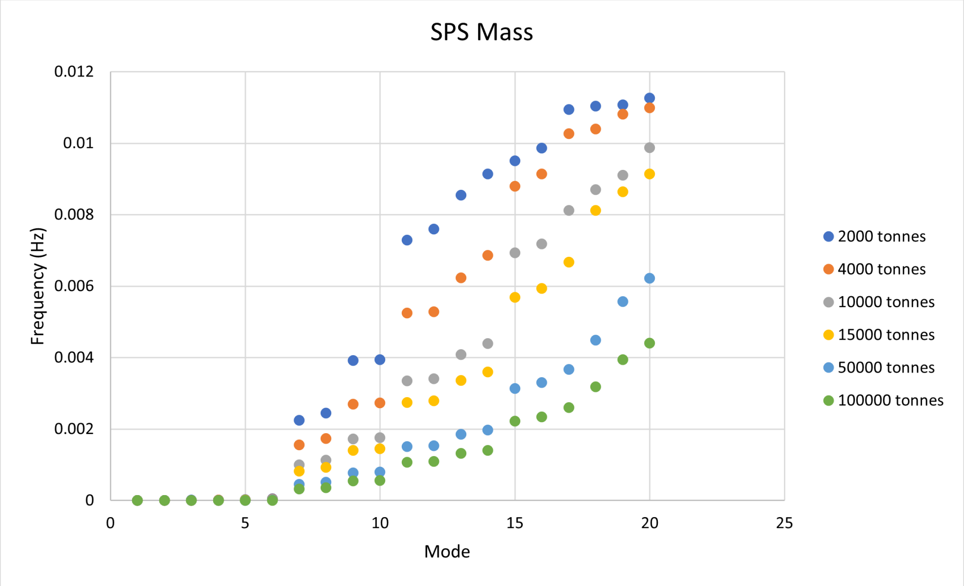

Figure 7.3: The effect of SPS mass on the modal frequencies.

7.3.2 Mass Distribution

Figure 7.4 shows the effect of varying the mass distribution on the frequencies for the first twenty modes. The case which features 15% of the SPS mass in the reflectors represents the CASSIOPeiA baseline configuration, in which the mass is focused in the central helix. This figure shows that an increase in the proportion of the mass in the reflectors, at each end of the SPS structure has relatively little effect on the modal frequencies. For Mode 7, the first flexural mode, the predicted modal frequency is 1.96×10^{-3} Hz for the configuration where 80% of the mass is focused at the ends. This presents negligible difference to the baseline frequency and is a factor of 85 greater than the excitation frequency.

7.3.3 Length

Figure 7.5 shows the effect of varying the SPS length on the frequencies for the first twenty modes. An SPS length of 6 km represents the CASSIOPeiA baseline configuration. This figure shows that an increase in the length of the SPS has a significant effect on reducing the modal frequencies. For Mode 7, the first flexural mode, the predicted modal frequency is 3.86×10^{-4} Hz for the 24 km long configuration. Whilst this modal frequency is significantly smaller than that predicted for the baseline model, it remains a factor of 17 greater than the excitation frequency.

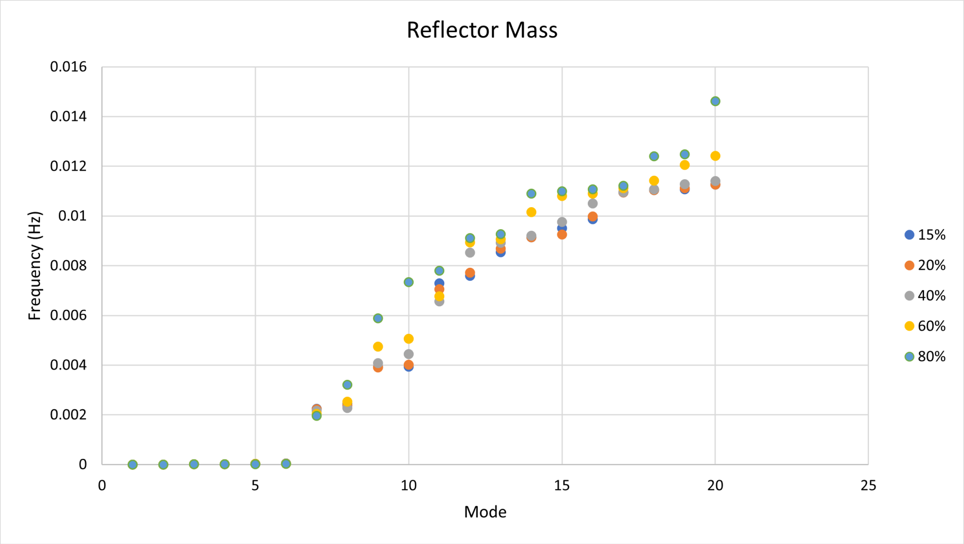

Figure 7.4: The effect of SPS mass distribution (expressed as the proportion of the mass in the Reflectors) on the modal frequencies.

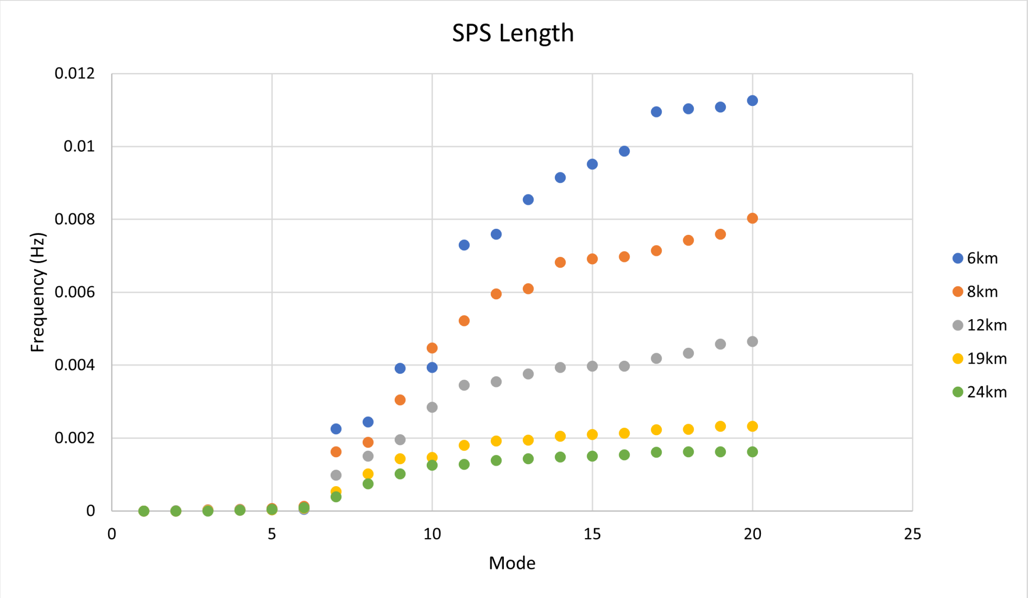

Figure 7.5: The effect of SPS length on the modal frequencies.

7.3.4 Stiffness

Figure 7.6 to Figure 7.8 show the effect of varying the stiffness of the CASSIOPeiA components on the frequencies for the first twenty modes. For the helix stiffness, a Young's Modulus of 0.02 GPa represents the CASSIOPeiA baseline configuration, and Figure 7.6 shows that an increase in stiffness increases the modal frequencies. It should be noted that a reduction in the helix stiffness from the baseline value resulted in instability issues with the finite element solver, however a reduction in the helix stiffness was considered unrealistic.

For the reflector stiffness, a Young's Modulus of 200 GPa represents the CASSIOPeiA baseline configuration and Figure 7.7 shows that a variation in the reflector stiffness results in very little change to the modal frequencies.

For the structural beam stiffness, a Young's Modulus of 200 GPa represents the CASSIOPeiA baseline configuration. Figure 7.8 shows that a reduction in the structural beam stiffness results in a reduction in the response frequency. For a beam stiffness of 2 GPa, representative of a sparse support structure, the predicted modal frequency is 8.7×10^{-4} Hz, which is a factor of 38 greater than the excitation frequency.

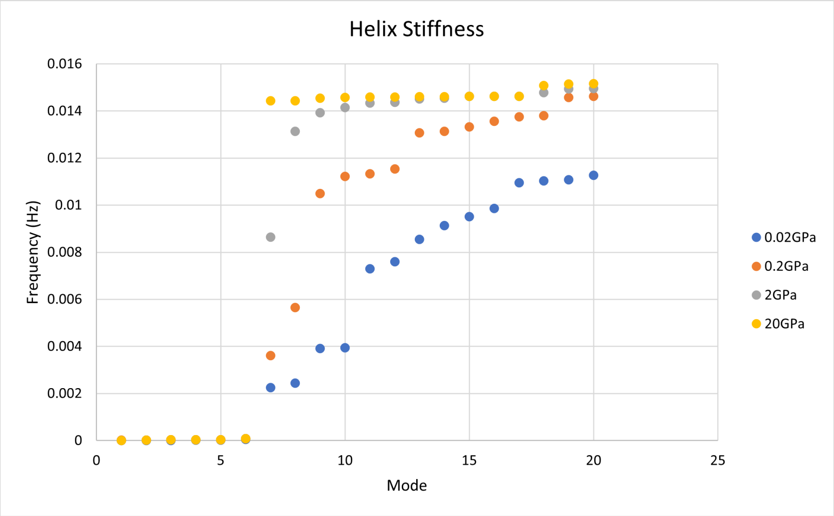

Figure 7.6: The effect of helix stiffness on the SPS modal frequencies.

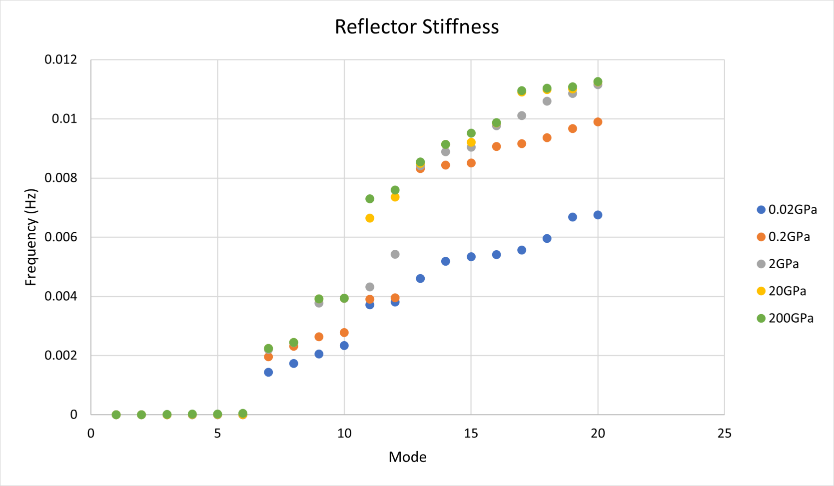

Figure 7.7: The effect of reflector stiffness on the SPS modal frequencies.

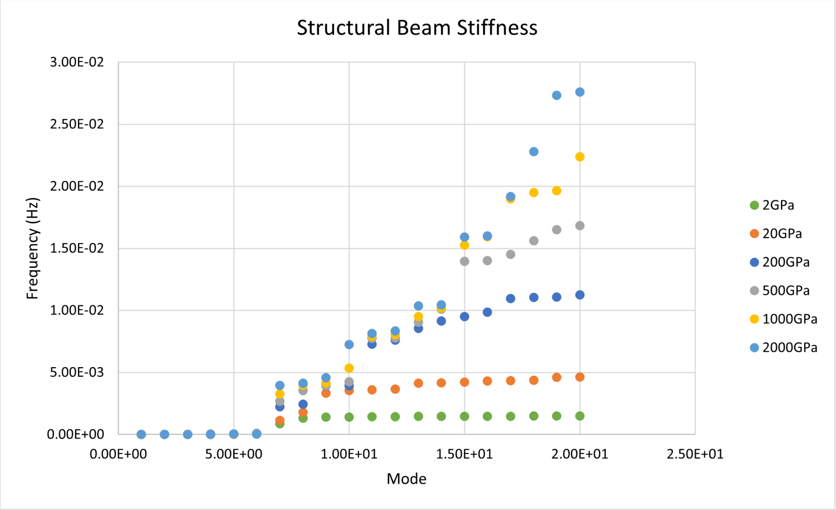

Figure 7.8: The effect of structural beam stiffness on the SPS modal frequencies.

7.3.5 Combined Mass and Length

For the range of design parameters considered, the modal analysis results have shown that the increase in SPS mass and length result in the most notable reduction in the modal frequencies. However, it is clear that whilst the ranges of masses and lengths that have been assessed bound the leading SPS concepts, it is possible that the combined effect of an increased mass and increased length may further reduce the frequency of the first flexural mode. Therefore, an additional set of modal analyses have been run for the following combinations:

- An increased mass of 10,000 tonnes and a range of lengths up to 24 km;
- An increased mass of 50,000 tonnes and a range of lengths up to 24 km;
- An increased length of 12 km and a range of masses up to 500,000 tonnes.

Figure 7.9 shows the effect of varying the SPS length and an increased mass on the frequency of the first flexural mode (Mode 7). This figure shows that for a 10,000 tonnes mass and 12 km length configuration (i.e. representative of concept MR-SPS), the modal frequency is 4.4×10^{-4} Hz; this is a factor of 19 greater than the excitation frequency. For an SPS mass of 50,000 tonnes and a length of 24 km, the modal frequency remains some margin higher than the excitation frequency.

Figure 7.10 shows the effect of varying the SPS mass and an increased length of 12 km on the frequency of the first flexural mode (Mode 7). This figure shows that an increased length of 12 km (i.e. representative of MR-SPS and SPS-Alpha), the SPS mass would need to be increased to approximately 500,000 tonnes in order to obtain a modal frequency closely aligned with the excitation frequency. Of the SPS concepts considered, MR-SPS has the largest mass of 10,000 tonnes, and therefore a mass of the order of 100,000 tonnes is considered unlikely.

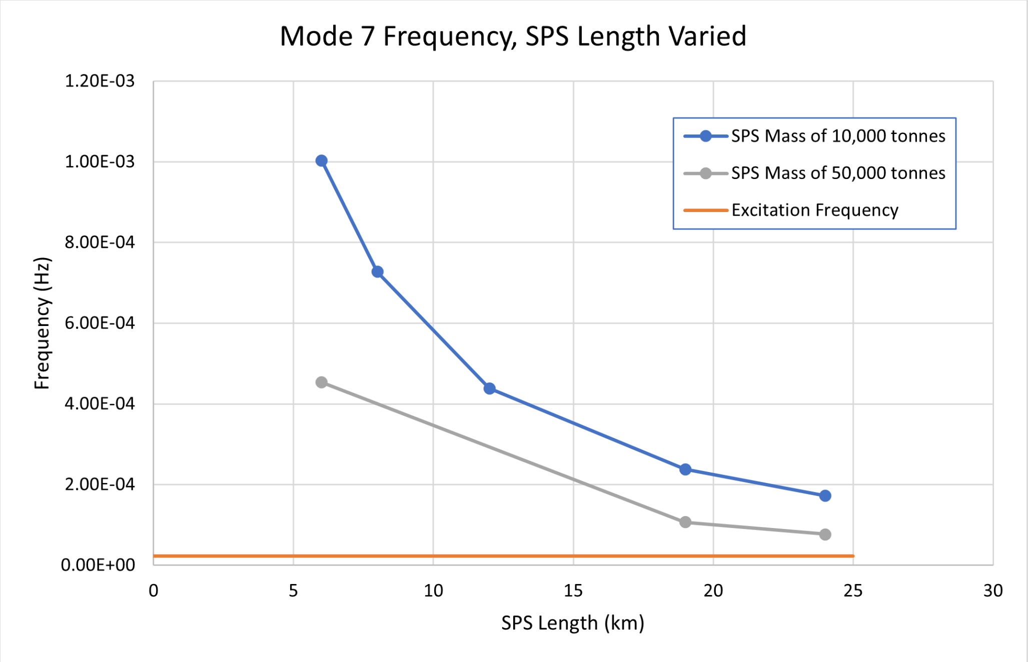

Figure 7.9: The effect of an increased mass and variation in the SPS length on the SPS modal frequencies.

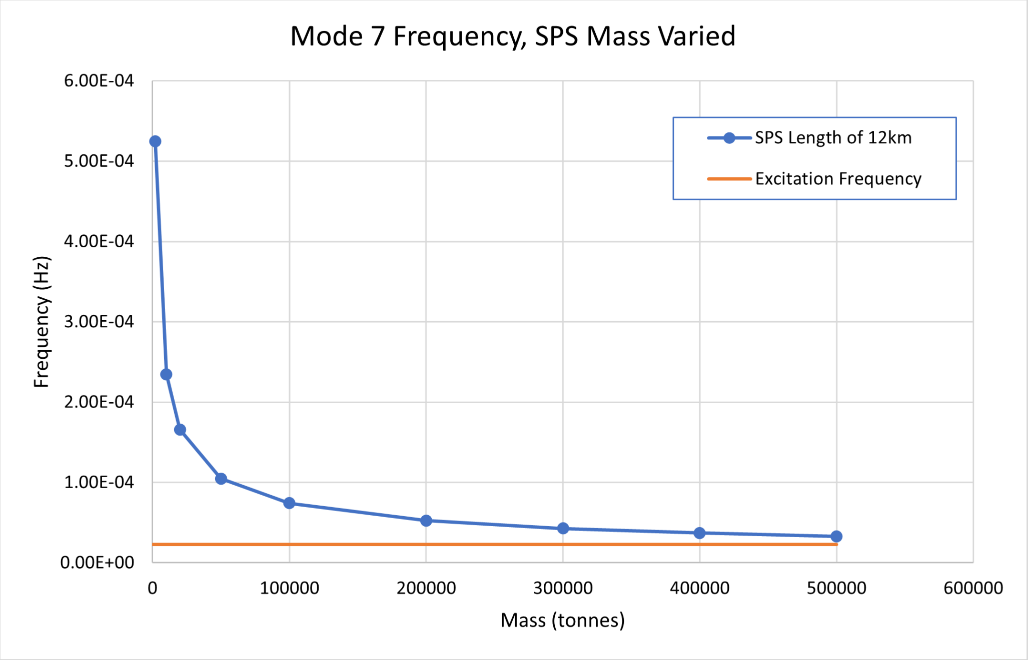

Figure 7.10: The effect of an increased length and variation in the SPS mass on the SPS modal frequencies.

7.3.6 Modal Analysis Conclusions

From the modal analyses, it is concluded that significant increases to both the SPS mass and length would be required to achieve a response frequency that is closely aligned with the excitation frequency.

In order to investigate the impact of the parameter changes on the SPS deformation and on the orbital loads, a case has been selected for further analysis. The sensitivity case features an increased SPS length of 12km and the mass varied up to 300,000 tonnes. This case has been considered as the increased length of 12km is representative of the MR-SPS and SPS-Alpha concepts. For this case a perturbation analysis for this case has been undertaken, as detailed in Section 8.

8 Analysis of Perturbation from Structural Deformation

The main aim of this project was to identify and characterize interactions between structural dynamics and orbital mechanics. This section deals with the effect structural dynamics can have on the orbital mechanics, in other words, what perturbations come as a result of the SPS deforming in a time-varying way throughout its orbit.

The following loads can deform the SPS structure:

- Gravity gradient
- Microwave beam
- Attitude control thrusters
- SRP

Assuming the SPS keeps pointing towards the Sun, the first three loads depend only on the position vector of the SPS relative to the Earth in the SPS's body frame. The SRP, during nominal operations, is a constant load, i.e. it does not vary along the orbit, given that the attitude of the spacecraft is constant towards the Sun. Its result is a constant force and a constant deformation. The constant force is already modelled in the classical way to deal with the SRP effect, while the constant deformation could be designed for.

The other three load types are ones that can cause deformation varying during the orbit. This deformation can in turn change the resultant of the SRP force, leading to an effect on the orbital dynamics. If the nominal SRP force is written as $\mathbf{F}_{\mathrm{SRP},0}$, and the SRP force on the deformed structure as $\mathbf{F}_{\mathrm{SRP}}$, we will study the effect of the difference between these two values, noting that the effect of $\mathbf{F}_{\mathrm{SRP},0}$ in creating a precession of the orbital plane and line of apsides was already covered in previous sections.

8.1 Static Analysis

During our initial analysis, it was shown that the frequencies of the non-rigid body modes were two orders of magnitude higher than the frequency of the orbital loads. As such, it is appropriate to model the loads as being static. As mentioned, the loads deforming the structure depend only on the position vector. Introducing the vector $\gamma = (\mathbf{F}_{\mathrm{SRP}} - \mathbf{F}_{\mathrm{SRP},0}) / |\mathbf{F}_{\mathrm{SRP},0}|$, we have $\gamma = \gamma(\mathbf{R}_c)$. To compute this vector, we must compute the loads at each finite element of the structure for each position of the SPS $\gamma = \gamma(\mathbf{R}_c)$, and then run the static analysis. This is a very computationally intensive process.

8.1.1 Harmonic Model

To alleviate the computational requirements, a surrogate model is proposed, based on spherical harmonics:

$$\gamma\left(R_c, \phi, \lambda\right) = \sum_{l=1}^{\infty} \sum_{m=0}^{l} P_{l,m}\left(\sin\left(\phi\right)\right) \left(\mathbf{C}_{l,m}(R_c) \cos\left(\lambda\right) + \mathbf{S}_{l,m}(R_c) \sin\left(\lambda\right)\right) \tag{8.1}$$

where R_c, ϕ, λ are the Earth centric distance, and the declination and azimuth of the Earth-SPS vector in the SPS body frame, see Figure 8.1. The $P_{l,m}$ are the associated Legendre functions. The vector coefficients $\mathbf{C}_{l,m}$ and $\mathbf{S}_{l,m}$ are found by least squares regression.

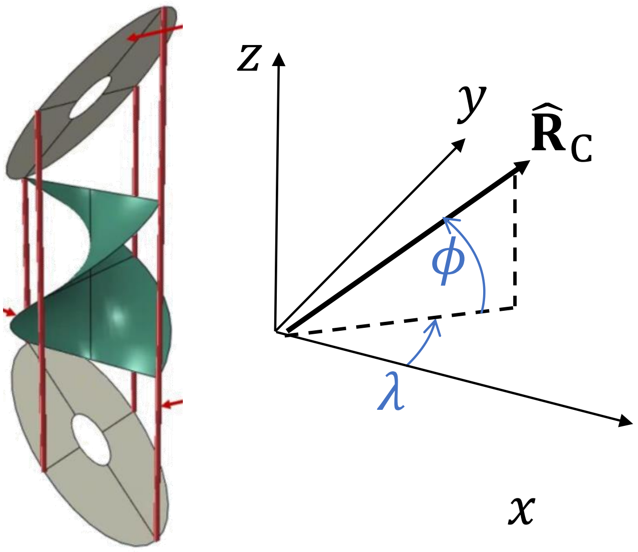

Figure 8.1: (Repeat of Fig. A.1.) Frame of the SPS with angles ϕ and λ represented. During nominal operations, the x axis points towards the Sun.

8.1.2 Symmetry

Before running simulations and performing regression, it is possible to say something about some values of these coefficients from what is known of the symmetry of the SPS. The SPS has rotational symmetry around its X axis, such that:

$$\gamma(\mathbf{R}_c) = R_X(180°)\gamma(R_X(180°)\mathbf{R}_c) \tag{8.2}$$

$$\gamma(R_c, \phi, \lambda) = R_X(180°)\gamma(R_c, -\phi, -\lambda) \tag{8.3}$$

This immediately implies that some of the coefficients are zero, namely for $l = 1$ and $l = 2$:

$$C^x_{10} = S^x_{11} = C^y_{11} = C^z_{11} = 0 \tag{8.4}$$

$$C^y_{20} = C^z_{20} = C^x_{21} = S^y_{21} = S^z_{21} = S^x_{22} = C^y_{22} = C^z_{22} = 0 \tag{8.5}$$

Table 8.1 contains the coefficients found by regression analysis in the next Section, where it is found that these coefficients are close to zero.

8.1.3 Model Regression

The vector coefficients are found by nonlinear least squares regression. The static finite element analysis is performed in Abaqus, producing the deformed structure, for various samples of ϕ_i and λ_i. This structure is then analysed following the ray-tracing method described in Chapter 6, to obtain γ_i. The coefficients up to order N_L are then found by minimizing the following equation:

$$\min_{\mathbf{C}_{l,m},\mathbf{S}_{l,m}} \sum_i \left\| \sum_{l=1}^{N_L} \sum_{m=0}^{l} P_{l,m}\left(\sin\left(\phi_i\right)\right)\left(\mathbf{C}_{l,m}(R_c)\cos\left(\lambda_i\right) + \mathbf{S}_{l,m}(R_c)\sin\left(\lambda_i\right)\right) - \gamma_i \right\|^2 \tag{8.6}$$

The dependency of the coefficients on R_c could be written by replacing each coefficient by a Taylor series. If this series was written around the semi-major axis, as $\mathbf{C}_{lm}(R_c) = \mathbf{C}_{lm,0} + \mathbf{C}_{lm,1}(R_c - a) + O\left((R_c - a)^2\right)$, it could also be written as $\mathbf{C}_{lm}(R_c) = \mathbf{C}_{lm,0} - a\mathbf{C}_{lm,1}(P_1 \sin L + P_2 \cos L) + O\left(e^2\right)$. However, given the small eccentricity, and as most of the variation in γ will be due to varying ϕ and λ, the dependency of γ on the radius R_c will be dropped, which greatly simplifies the model regression.

Table 8.1 shows the coefficients of γ^z found by optimizing Eq. (8.6). The components γ^x and γ^y were found to be negligible. Of note is that the components that are supposed to be zero due to the symmetry, as explained in Section 8.1.2, are confirmed to be zero in this table.

Table 8.1: Coefficients of γ^z. Light gray elements are those found to be most significant. Light blue elements are those that should be zero due to the symmetry of the SPS.

l	m	C^z_{lm}	S^z_{lm}
1	0	-8.37×10^{-5}	
1	1	-4.87×10^{-7}	-5.72×10^{-5}
2	0	-3.25×10^{-7}	
2	1	-1.98×10^{-4}	4.87×10^{-7}
2	2	-1.03×10^{-8}	2.58×10^{-6}
3	0	-9.31×10^{-5}	
3	1	-3.80×10^{-7}	-1.49×10^{-5}
3	2	1.74×10^{-6}	-4.09×10^{-8}
3	3	7.66×10^{-9}	2.02×10^{-7}

8.1.4 Conversion to RTN accelerations

To get the variations in the orbital elements, the acceleration is then converted into the RTN frame, before being inserted into Gauss's VoP equations, which are then integrated to get the averaged variation. Because the SPS body frame is a frame that is aligned with the Sun, it makes most sense to use elements in the Sun's frame. In the RTN frame, the vector γ can then be written as:

$$\gamma^{RTN} = \sum_m \hat{\mathbf{C}}_m^{RTN}(R_c, Q_{1,\odot}, Q_{2,\odot}) \cos(mL) + \hat{\mathbf{S}}_m^{RTN}(R_c, Q_{1,\odot}, Q_{2,\odot}) \sin(mL) \tag{8.7}$$

This conversion is done with the help of Wolfram Mathematica ®. The vectors $\mathbf{f}$, $\mathbf{g}$ and $\mathbf{h}$ are used to define the Equinoctial frame, for equinoctial elements defined in the Sun frame. The following results are then used to finalize converting Eq. (8.1) into Eq. (8.7) [15]:

$$\begin{aligned}
\hat{\mathbf{R}}_c &= \hat{\mathbf{f}} \cos(L) + \hat{\mathbf{g}} \sin(L) \tag{8.8}\\
\sin\left(\phi\right) &= \hat{f}^z \cos(L) + \hat{g}^z \sin(L) \tag{8.9}\\
\cos(\lambda) \cos\left(\phi\right) &= \hat{f}^x \cos(L) + \hat{g}^x \sin(L) \tag{8.10}\\
\sin(\lambda) \cos\left(\phi\right) &= \hat{f}^y \cos(L) + \hat{g}^y \sin(L) \tag{8.11}\\
\gamma^{\mathrm{RTN}} &= \left[\left(\hat{\mathbf{f}} \cos(L) + \hat{\mathbf{g}} \sin(L)\right) \quad \left(-\hat{\mathbf{f}} \sin(L) + \hat{\mathbf{g}} \cos(L)\right) \quad \hat{\mathbf{h}}\right]^T \gamma \tag{8.12}
\end{aligned}$$

8.1.5 Averaged Variations

The RTN accelerations are inserted into Gauss' VoP equations $\dot{X} = G(X, L)$, where X is a vector containing the slow elements, and L is the fast element, the true longitude. These equations are then averaged, which corresponds to writing $\dot{\overline{X}} = \frac{1}{T}\int_0^{2\pi} G(X, L)\,\mathrm{d}L = \overline{G}(X)$. Averaging these equations requires calculating integrals of the form:

$$\overline{I}_{cmn} = \int_0^{2\pi} \frac{\cos mL}{(1 + P_1 \sin L + P_2 \cos L)^n} \tag{8.13}$$

$$\overline{I}_{smn} = \int_0^{2\pi} \frac{\sin mL}{(1 + P_1 \sin L + P_2 \cos L)^n} \tag{8.14}$$

which have exact results [16]. However, these involve complicated expressions, that often have numerical issues around $P_1 = P_2 = 0$. Again using Wolfram Mathematica ®, the integrand is approximated with a second order Taylor series on the eccentricity, before the definite integrals are calculated, obtaining:

$$\overline{I}_{c0n} = 1 + \frac{1}{4}e^2(n(n+1)) + O(e^3) \tag{8.15}$$

$$\overline{I}_{c1n} = -\frac{1}{2}nP_2 + O(e^3) \tag{8.16}$$

$$\overline{I}_{c2n} = \frac{1}{8}n(n+1)(P_2^2 - P_1^2) + O(e^3) \tag{8.17}$$

$$\overline{I}_{s1n} = -\frac{1}{2}nP_1 + O(e^3) \tag{8.18}$$

$$\overline{I}_{s2n} = \frac{1}{4}P_1P_2n(n+1) + O(e^3) \tag{8.19}$$

The function G and its average $\overline{G}$ were derived for the elements in the Sun frame. To obtain correct results, they have to be converted into an inertial frame, such as the ecliptic frame. For these, the following formulae are used:

$$P_{1,\odot} = P_1 \cos L_\odot - P_2 \sin L_\odot \tag{8.20}$$

$$P_{2,\odot} = P_2 \cos L_\odot + P_1 \sin L_\odot \tag{8.21}$$

$$\tag{8.22}$$

with formulas for Q_1 and Q_2 being obtained by replacing P with Q in the above.

The resulting $\overline{G}$ can be written in the form of a Taylor series on $\mathbf{Q}$, and a Fourier Trig series over $L_\odot$:

$$\begin{aligned}\overline{G} = &\left(\overline{G}_0 + \nabla_{\mathbf{Q}}\overline{G}_0\mathbf{Q} + \frac{1}{2}\mathbf{Q}^T H_{\mathbf{Q},0}\mathbf{Q} + \ldots\right) \\ &+ \sum_k \left(\overline{G}_{ck} + \nabla_{\mathbf{Q}}\overline{G}_{ck}\mathbf{Q} + \frac{1}{2}\mathbf{Q}^T H_{\mathbf{Q},ck}\mathbf{Q} + \ldots\right)\cos kL_\odot \\ &+ \sum_k \left(\overline{G}_{sk} + \nabla_{\mathbf{Q}}\overline{G}_{sk}\mathbf{Q} + \frac{1}{2}\mathbf{Q}^T H_{\mathbf{Q},sk}\mathbf{Q} + \ldots\right)\sin kL_\odot\end{aligned} \tag{8.23}$$

Showing the entire resulting expressions here would be too cumbersome, but as an example, the semi-major axis constant term is, with coefficients up to order 3, written as:

$$\overline{G}_0^a = \frac{k_{SRP}}{3} a \left(-2C_{11}^y + 2S_{11}^x + 3C_{31}^y - 3S_{31}^x \right) \tag{8.24}$$

If this term is non-zero, we would have a secular variation of the semi-major axis, but as shown in Section 8.1.2, every coefficient appearing in the above expression is zero by definition. Hereafter, all elements and variations are their averaged versions, but the over-bar $\bar{\cdot}$ will be omitted.

8.1.6 Perturbation Analysis

Let X be the vector containing the orbital elements that are varying. Following the typical process of perturbation analysis, we write $X = X_0 + \epsilon X_1 + \epsilon^2 X_2 + \ldots$, where ϵ is a bookkeeping device, to keep track of the order of magnitude of each term. The orbital dynamics are written as $\dot{X} = \epsilon^2 F + \epsilon^{2+\eta} G$, where F contains the usual dynamics, i.e. aspherical potential, $\mathbf{F}_{\text{SRP},0}$, and third body perturbations, while G contains the effect caused by γ. The parameter η is defined such that terms or order $O(\epsilon^\eta)$ are of the order of γ, which was unknown at the time this expansion was carried out, but an analysis can nonetheless be performed before this data is available.

The time variable used is $L_\odot$, approximated as $L_\odot = \dot{L}_\odot t$, so all time derivatives written as $\dot{X}$ are to be seen as derivatives in $L_\odot$. The order of magnitude of F is given by the coefficient $k_{\text{SRP}} \approx 0.014$, which determines the effect of the SRP perturbation on the elements as in Eq. (4.26). The other perturbations are of similar order of magnitude or smaller, so it is reasonable to use k_{SRP} as a measure of the order of magnitude of F. Therefore, terms multiplying ϵ^n should be seen as being of the order of $k_{\text{SRP}}^{n/2}$, where $\sqrt{k_{\text{SRP}}} = 0.12$. Note, however, that since ϵ is merely a bookkeeping device to keep track of the orders of magnitude of each term, it equals 1. This form of perturbation analysis is known to be accurate up to $L_\odot \sim O(k_{\text{SRP}}^{-1/2})$ [17], which means it is accurate for around one year, allowing us to average these variations over a year, giving us doubly averaged elements.

The expansion is around the second order to allow writing $X_0 = [a_0, 0, 0, 0, 0]^T$ and $X_1 = [0, 0, 0, Q_{11}, Q_{21}]^T$. This somewhat unusual method of expanding the perturbation terms has the goal of allowing the perturbation G to be written as a series on $\mathbf{Q}_1 = [Q_{11}, Q_{21}]^T$, and can be justified by the fact that $|\mathbf{Q}| = \tan i/2 \approx 0.2 \sim \sqrt{k_{\text{SRP}}}$ for GEO orbit.

The G term is expanded around X_0, resulting in $G = G_0 + \epsilon \nabla G_0 (X_1 + \epsilon X_2 + \ldots) + \epsilon^2 \frac{1}{2} (X_1 + \epsilon X_2 + \ldots)^T H_{G_0} (X_1 + \epsilon X_2 + \ldots) + \ldots$, where G_0, ∇G_0, and H_{G_0} is the function G, its gradient, and its Hessian evaluated at X_0. We do the same with F. If we write $\dot{X}_F$ and $\dot{X}_G$ to represent the variations due to F and G respectively, such that $\dot{X} = \dot{X}_F + \dot{X}_G$, then the following can be written:

$$\dot{X}_{F2} = F_0(t) \tag{8.25}$$

$$\dot{X}_{F3} = \nabla F_0(t) X_1 \tag{8.26}$$

$$\dot{X}_{F4} = \nabla F_0(t) X_2(t) + \frac{1}{2} X_1^T H_{F_0}(t) X_1 \tag{8.27}$$

$$\dot{X}_{F5} = \nabla F_0(t) X_3(t) + X_1^T H_{F_0}(t) X_2 \tag{8.28}$$

The solution to the above equations is given by the precession of the orbital plane and line of apsides that have been discussed in Section 4.4. We are interested instead in the contribution of G.

$$\dot{X}_{G(2+\eta)} = G_0(t) \tag{8.29}$$

$$\dot{X}_{G(3+\eta)} = \nabla G_0(t) X_1 \tag{8.30}$$

$$\dot{X}_{G(4+\eta)} = \nabla G_0(t) X_2(t) + X_1^T H_{G_0}(t) X_1 \tag{8.31}$$

The term $X_2 = X_{F2}$, which includes the integration of the SRP term for a circular orbit, would consist of a rotating line of apsides of the form:

$$\begin{aligned} P_{12} &= P_{120} + e_{\mathrm{SRP}} \sin L_{\odot} \\ P_{12} &= P_{220} + e_{\mathrm{SRP}} \cos L_{\odot} \\ e_{\mathrm{SRP}} &= \frac{3}{2}\sqrt{\frac{a}{\mu}} \frac{a_{\mathrm{SRP}}}{\dot{L}_{\odot}} \end{aligned} \tag{8.32}$$

where P_{120} and P_{220} are constants of integration. For this method of perturbation to work, they must be chosen to avoid secular terms [17], which means $P_{120} = P_{220} = 0$. The term $\nabla G_0(t) X_2(t)$ could include resonances, since both have harmonic terms with frequency $\dot{L}_{\odot}$. To be completely accurate, X_2 should also include the precession of the orbital plane. However, that term would not include resonance, since it does not have the same frequency as G, and given that X_2 is only affecting $\dot{X}_{G(4+\eta)}$, a term of order $\epsilon^{4+\eta}$, we do not consider this, and limit our analysis of the effect of the term $\nabla G_0(t) X_2(t)$ to the apsidal rotation in X_2 given by Eq. (8.32). In fact, the term $\nabla G_0(t) X_2(t)$ includes the following secular term in the semi-major axis component:

$$\nabla G_0^a(t) X_2(t) = 2a \; k_{SRP} \; e_{\mathrm{SRP}} \left(-C_{22}^y + S_{22}^x \right) + \ldots \tag{8.33}$$

The symmetry conditions, however, imply that this is zero, and as such there is no need to worry about this secular term. Note also that $\nabla G_0^a(t) X_2$ is of the order of $k_{SRP}^2 \gamma$, which is coherent with $\epsilon^{4+\eta}$.

If $\eta \geq 1$, we can solve for $X_{G(2+\eta)}$, $X_{G(3+\eta)}$, and $X_{G(4+\eta)}$ using only the known X_0, X_1, and X_2. Furthermore, each of the terms in Eqs (8.29 - 8.31) can be integrated separately.

Making all coefficients zero except for those marked in gray in Table 8.1, and expanding to second order in $\mathbf{Q}$ and in $L_{\odot}$ results in:

$$\overline{G}^{\mathbf{Q}} = \frac{2C_{10}^z - 3C_{30}^z}{6} \begin{bmatrix} Q_2 \\ -Q_1 \end{bmatrix} \tag{8.34}$$

$$\overline{G}^{P_1} = C_{21}^z \left(\left(5Q_1^2 - Q_2^2 \right) \cos L_{\odot} + 6 Q_1 Q_2 \sin L_{\odot} \right) \tag{8.35}$$

$$\overline{G}^{P_2} = -C_{21}^z \left(\left(5Q_2^2 - Q_2^2 \right) \sin L_{\odot} + 6 Q_1 Q_2 \cos L_{\odot} \right) \tag{8.36}$$

all other terms being zero up to the orders that this expansion was carried out to.

Using these results to solve the terms in Eqs (8.29 - 8.31), and obtaining the yearly average $\dot{\overline{X}}_G = \frac{1}{2\pi} \int_0^{2\pi} \dot{X}_G \, \mathrm{d}L_{\odot}$, results in:

$$\dot{\overline{X}}_G = k_{SRP} \frac{2C_{10}^z - 3C_{30}^z}{6} \begin{bmatrix} 0 & 0 & 0 & Q_2 & Q_1 \end{bmatrix} \tag{8.37}$$

as all terms other than the variation in Q_1 and Q_2 disappear after averaging. As such, the secular effect of the perturbation G, with the coefficients we found, is such that $\mathrm{d}|\mathbf{Q}|/\,\mathrm{d}t = 0$, since $\dot{\overline{X}}_G^{\mathbf{Q}} \cdot \mathbf{Q} = 0$. This means that it will cause a constant variation of Ω, while keeping the inclination i constant, i.e., it will cause a precession of the orbital plane about the normal vector to the ecliptic. This has the effect of making the Laplace plane slightly closer to the ecliptic. Note, however, that this is a very small effect, since $k_{SRP}\dfrac{2C^z_{10}-3C^z_{30}}{6} \approx 1.6\times10^{-6}/\mathrm{year}$, corresponding to $\dot{\Omega} = k_{SRP}\dfrac{2C^z_{10}-3C^z_{30}}{6|\mathbf{Q}|} = 7.6\times10^{-6}\mathrm{rad}/\mathrm{year}$, a completely negligible variation.

As such, it can be concluded from this analysis that for the SPS design under consideration, the structural dynamics do not significantly affect the orbital dynamics, up to the order of the analysis carried out here. Of interest for future work would be to analyse which design variants would have a significant effect on the orbit from these effects.

8.2 Modal Analysis

As part of the parametric study, scenarios were identified where the natural frequency was close to the forcing frequency of the gravity gradient and thruster forces. In particular, set 9 of Fig. 7.2 described in Section 7.2, where the SPS's length is increased to 12km, while the mass is varied, which leads to the natural frequency approaching the frequency of the forcing term, see Figure 8.2. If the frequencies get too close to resonance, this linear analysis becomes less realistic, to the point where the deflection of the structure predicted by this method can reach magnitudes at the kilometre scale. In reality, such scenarios might lead to the destruction of the SPS, if non-linearities or damping are not enough to substantially reduce the effect of this resonance. For this test case, however, such a scenario did not occur.

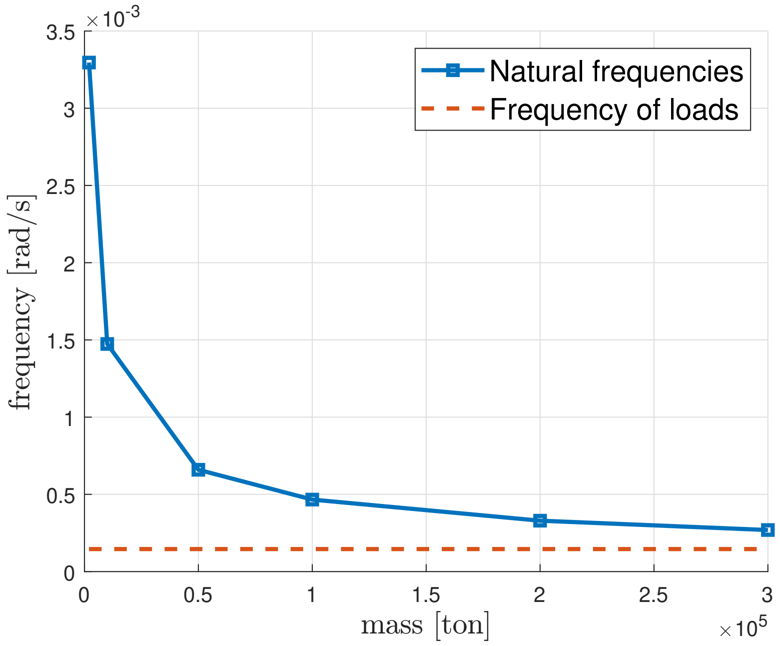

Figure 8.2: Natural frequencies plotted against the total mass for a 12km long SPS.

In this analysis, the effect these modes might have on the orbit have been studied, by the introduction of a periodic force in the form of the varying SRP force due to the deformation of the structure. Using linear vibration analysis, the vibration of the SPS may be described using the modal amplitude $q(t)$, where the mode shape is given by $\boldsymbol{\phi}$ scaled such that $\boldsymbol{\phi}^T M\boldsymbol{\phi} = 1$. A single mode has been considered, which in our case is the first non-rigid body mode. The deformation of the structure is then given by $\mathbf{x}(t) = q(t)\phi$, where the vector $\mathbf{x}$ contains the displacement of each node of the structure [18]. The generalized mode coordinate then obeys the familiar equation:

$$\ddot{q}(t) + 2\zeta\omega\dot{q}(t) + \omega^2 q(t) = \boldsymbol{\phi}^T\mathbf{f}(t) \tag{8.38}$$

where $\mathbf{f}(t)$ is the force applied in each node along the direction of the displacement represented by each node. The displacements $\mathbf{x}$ are given by the x, y, and z displacements of each node, forming a vector of the form:

$$[x_1, y_1, z_1, x_2, y_2, \dots, x_N, y_N, z_N]^T \tag{8.39}$$

and as such the force $\mathbf{f}(t)$ is the x, y, and z components of the force applied on each node.

8.2.1 Gravity gradient and Thruster forces

As shown in Section 3, the gravity gradient forces have twice the frequency of the orbital frequency, as a result of the 2θ terms that appear in their expression. In fact, with the help of Wolfram Mathematica ®, both the gravity gradient and the thruster torque terms can be written as:

$$\mathbf{f}(\mathbf{r}) = \mathbf{f_0}(\mathbf{r}) + \mathbf{f_{cc}}(\mathbf{r})\cos\boldsymbol{\Omega}_\odot\cos 2\theta + \mathbf{f_{cs}}(\mathbf{r})\cos\boldsymbol{\Omega}_\odot\sin 2\theta + \mathbf{f_{sc}}(\mathbf{r})\sin\boldsymbol{\Omega}_\odot\cos 2\theta + \mathbf{f_{ss}}(\mathbf{r})\sin\boldsymbol{\Omega}_\odot\sin 2\theta \tag{8.40}$$

It is immediately clear that, if this load is to be written in the form $A_f \cos 2\theta + \phi_f$, both the amplitude A_f and the phase ϕ_f will vary with $\Omega_\odot$ and with the position in the SPS it is applied to $\mathbf{r}$. In the literature, when analysing forced vibrations of multi-dimensional systems, one method involves finding the mode participation factors Γ_i for each mode. Typically, the loads are written by separating the spacial and temporal evolution, i.e.,

$$f(\mathbf{r}) = \overline{f}(\mathbf{r})\cos t + \phi \tag{8.41}$$

and the participation factor is:

$$\Gamma_i = \overline{f}(\mathbf{r})^T \boldsymbol{\phi}_i(\mathbf{r}) \tag{8.42}$$

turning the right hand side of Eq. (8.38) into $\Gamma_i \cos t + \phi$. This method cannot be directly applied in this form to our case, however, because the phase of the loads is different for each element. Therefore, our loads cannot be written as in Eq. (8.41). The solution is to represent the amplitude $\overline{f}(\mathbf{r})$ as a complex value. Thomson [19] goes into great detail into the use of complex numbers in linear vibration theory, but a brief explanation is presented here. Any harmonic quantity varying with frequency ω can be written as the real part of $Ae^{i\omega t}$, where A is complex. The phase of A will then be the phase of this quantity. Given the linearity of Eq. (8.38), if our right hand side is complex, where its real part is the value of the forcing term, then the real part of the solution will be the solution we seek. If our loads are represented as:

$$\tilde{\mathbf{f}} = \mathbf{f}_0 + \tilde{\mathbf{f}}_{2\theta} e^{2i\theta} \tag{8.43}$$

where $\mathbf{f}_{2\theta}$ is a complex vector, that contains information on the phase of the load applied to each element of the SPS:

$$\tilde{\mathbf{f}}_{2\theta} = (\mathbf{f}_{cc}\cos\Omega_\odot + \mathbf{f}_{sc}\sin\Omega_\odot) - i\,(\mathbf{f}_{cs}\cos\Omega_\odot + \mathbf{f}_{ss}\sin\Omega_\odot) \tag{8.44}$$

then the real part of $\tilde{\mathbf{f}}$ will be exactly given by Eq. 8.40.

Since $\Omega_\odot = \Omega - L_\odot$, there is also a dependency on the position of the Sun, represented by $L_\odot$. We can also write $\theta = nt$ for a circular orbit approximation. Given the linearity of Eq. (8.38), the principle of superposition applies, meaning the 2θ component of q may be found by inserting $\tilde{\mathbf{f}}_{2\theta}$ into Eq. (8.38), and taking the real part of the solution, to obtain:

$$q(t) = \mathrm{Re}\left(\frac{\boldsymbol{\phi}^T \mathbf{f}_{2\theta} e^{2i\theta}}{4n^2 - \omega_m^2 + 4\zeta n \omega_m i}\right) \tag{8.45}$$

This corresponds to a sinusoid with frequency $2n$, amplitude:

$$A = \frac{|\boldsymbol{\phi}^T \mathbf{f}_{2\theta}|}{\sqrt{(4n^2 - \omega_m^2)^2 + (4\zeta n \omega_m)^2}} \tag{8.46}$$

and phase given by the phase of the term multiplying $e^{2i\theta}$ in Eq. (8.45). The amplitude A in Eq. (8.46) is a non-dimensional quantity (if $\boldsymbol{\phi}$ is considered to be in units of length), and cannot be directly interpreted unless when multiplied by ϕ. The value of $A \max \boldsymbol{\phi}$, shown in Figure 8.3, represents the maximum distortion along the entire SPS, where $\max \phi$ is the maximum length of the displacement vector represented by $\boldsymbol{\phi}$.

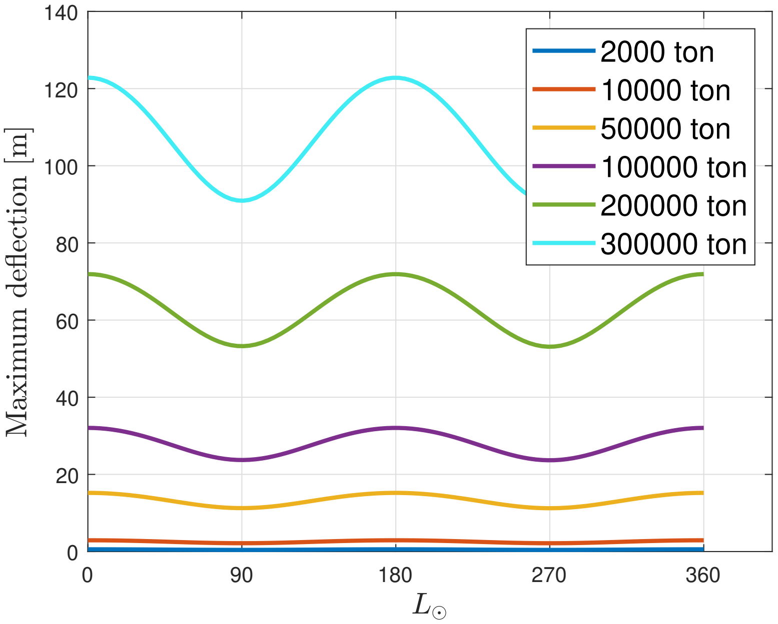

Figure 8.3: Maximum displacement as a function of the longitude of the Sun $L_\odot$, for various values of the mass.

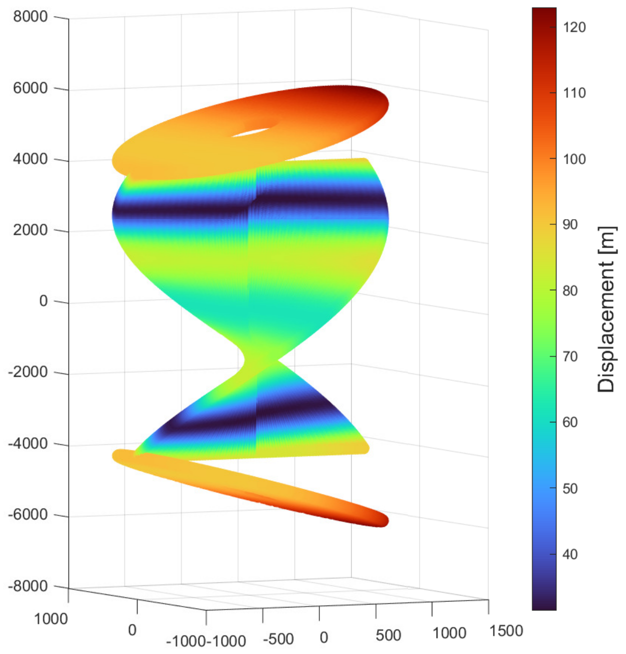

Figure 8.4: Plot of the displacement magnitude, i.e. the norm of $A\phi$, along the surface of the SPS.

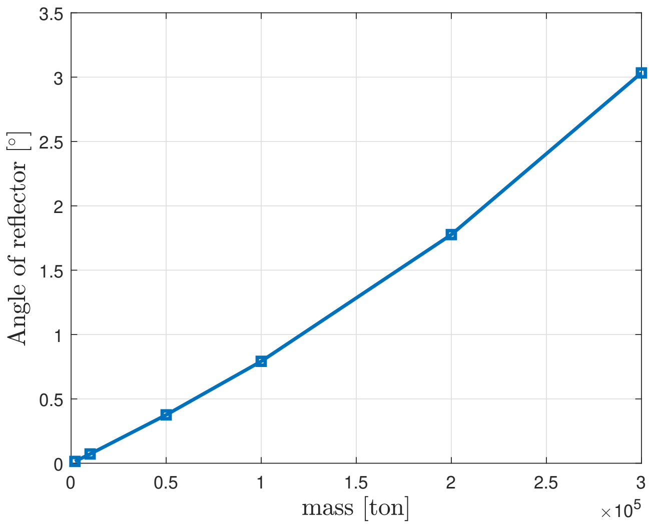

Figure 8.5: Angle of reflector with respect to its nominal position

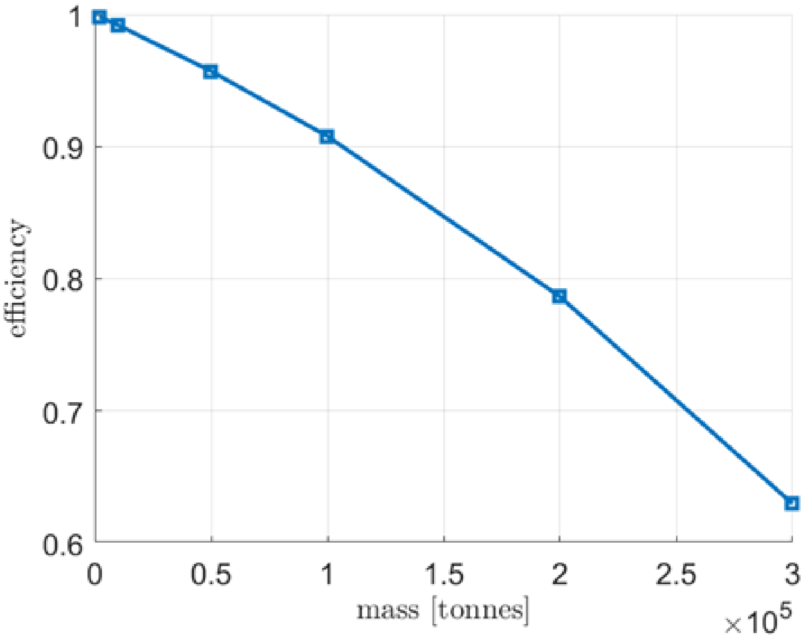

Figure 8.6: A plot of the efficiency as a function of the mass, corresponding to set 9 in Fig. 7.2. The efficiency is defined as the fraction of sunlight hitting the reflectors that hits the helix.

As shown in Figure 8.4, the maximum distortion of the SPS is seen at the farthest ends of the reflectors. As per the static analysis, the reflectors were found to remain flat, but rotated with respect to their nominal position. Figure 8.5 shows this angle as a function of the SPS mass in this parameter study. It can get to 3 degrees, which leads to a significant amount of efficiency reduction. For the highest mass case, at maximum deformation, only 63% of the sunlight continues hitting the SPS, as shown in Figure 8.6. This effect would be oscillatory with the same frequency of twice the mean motion as the gravitational gradient effect.

8.2.2 Variation of Parameters

For each SPS design being considered, the maximum value of q is calculated, and the deformed SPS at various values of q is then the input of a ray-tracing analysis, to find the value of the resultant SRP force applied on it. The difference to the nominal value is then converted into the RTN frame, which is then written in Fourier series form:

$$F^{RTN} = \sum_k \mathbf{C}_k^{RTN} \cos kL + \mathbf{S}_k^{RTN} \sin kL \tag{8.47}$$

It was found that the non-zero terms were the RT components with $k \in 1, 3$ and the N component with $k = 2$, which is a consequence of the force in the ecliptic frame being proportional to $\cos 2\theta + \alpha$. After introducing the acceleration resulting from this into Gauss's VoP equations and averaging, we obtain the following expressions, approximated to within $O(e^2)$:

$$\frac{\mathrm{d}\overline{a}}{\mathrm{d}t} = \frac{a^3B^2}{\mu}\left((S_1^R - C_1^T)P_2 - (C_1^R + S_1^T)P_1\right) + O(e^2) \tag{8.48}$$

$$\frac{\mathrm{d}\overline{P}_1}{\mathrm{d}t} = \frac{a^2B^4}{\mu}\left(-\frac{1}{2}C_1^R + S_1^T\right) + O(e^2) \tag{8.49}$$

$$\frac{\mathrm{d}\overline{P}_2}{\mathrm{d}t} = \frac{a^2B^4}{\mu}\left(-\frac{1}{2}S_1^R + C_1^T\right) + O(e^2) \tag{8.50}$$

$$\frac{\mathrm{d}\overline{Q}_1}{\mathrm{d}t} = -\frac{3a^2B^4}{8\mu}(1 + Q_1^2 + Q_2^2)\left(S_2^N P_2 - C_2^N P_1\right) + O(e^2) \tag{8.51}$$

$$\frac{\mathrm{d}\overline{Q}_2}{\mathrm{d}t} = -\frac{3a^2B^4}{8\mu}(1 + Q_1^2 + Q_2^2)\left(C_2^N P_2 - S_2^N P_1\right) + O(e^2) \tag{8.52}$$

The phase of $\mathbf{f}$, and thus of q depends on the position of the Sun, $L_\odot$, as the SPS is assumed to be continuously facing the Sun with its Z axis normal to the ecliptic plane. In the following calculations it has been assumed that $i = \Omega = 0$, and that the argument of pericentre and eccentricity follows the law in Section 4.3, which means it too depends on $L_\odot$. The results are shown in Figure 8.7 for the semi-major axis and argument of pericentre, which were the values found to vary the most. Not only are these variations very small, but they also average to zero, leading to no overall effect. The increase in mass puts the frequency closer to the forcing term, thus increasing the distortion of the SPS (Figure 8.3), and so the SRP force resulting from it. This is countered, however, by the increase in mass leading to lower accelerations.

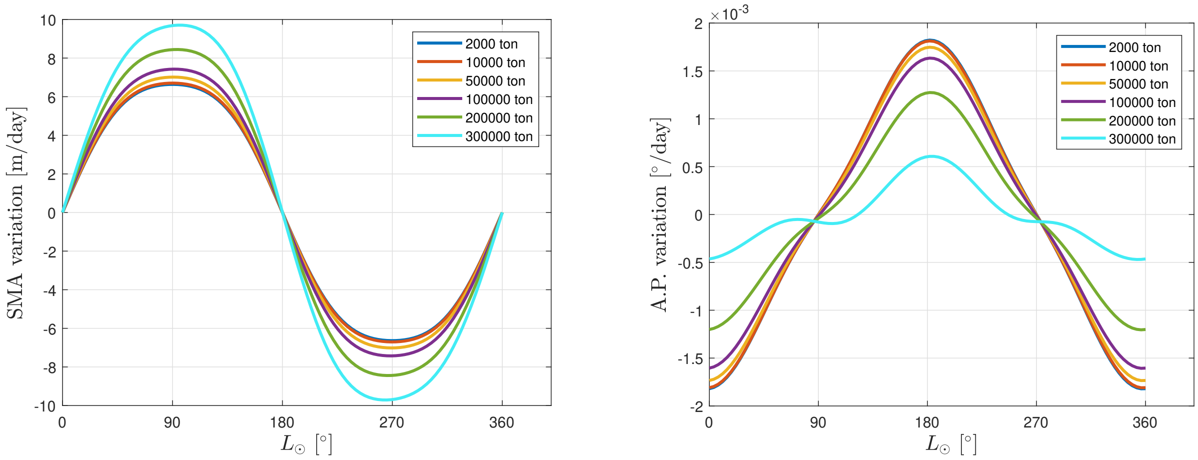

a: Variation of semi-major axis

b: Variation of argument of pericentre

Figure 8.7: Variation of orbital parameters resulting from the forced vibration due to orbital loads

9 Conclusions

A study has been carried out to investigate the magnitude of the coupling between the structural dynamics and orbital mechanics of Solar Power Satellites.

The potential interaction between the structural dynamics and the orbital mechanics for such a sparse flexible structure has been achieved through the development of a finite element model alongside a numerical analysis approach. The combination of these analytical methods has been instrumental in: quantifying the potential disturbance to the orbit of an SPS, identifying trends in the structural response for design parameters, and in devising a set of outline design guidelines.

A leading SPS design, CASSIOPeiA, has been characterised to enable an analytical model to be developed for the purpose of this study. This characterisation has shown that, alongwith many of the leading SPS designs, CASSIOPeiA currently lacks key design details such as material selection and the degree of structural support. This study has focused on CASSIOPeiA operating in GEO and therefore, it should be noted that the conclusions are specific to GEO and would likely differ for a Medium Earth Orbit (MEO) and a Low Earth Orbit (LEO).

A review of orbital loads has been conducted as part of this study, considering both loads that are constant and loads that vary with orbital position. The gravity gradient acceleration has a period of half a day, and therefore presents the lowest excitation frequency of 2.3×10^{-5} Hz. For the baseline CASSIOPeiA configuration, the response frequency of the first flexural mode is two orders of magnitude greater than the excitation frequency.

Solar radiation pressure, which for CASSIOPeiA is a load that does not vary with orbital position, results in negligible displacement between the two reflectors. In response to the loads that do vary with orbital position, the maximum displacement of the reflectors is 2.88 m; this equates to 0.14% of the SPS diameter and is therefore tolerable. Therefore, the deformation of the baseline CASSIOPeiA design that varies along the SPS orbit is not expected to cause an interaction between the structural and orbital dynamics and will have negligible effect on the SPS performance.

A parametric study has been undertaken with the objective of investigating trends in the dynamic response of the CASSIOPeiA structure for a range of design parameters. The SPS mass and SPS length were identified as the most influential parameters on reducing the modal frequencies, thus potentially bringing them inline with the excitation frequency. Adjusting the mass distribution for the CASSIOPeiA model does not have a significant impact on the response frequency, and order of magnitude changes to the stiffness of the helix, reflectors and structural beams in isolation does not have a significant impact on reducing the response frequency.

As part of the parametric study, a combination of increasing the mass and the length of the SPS model was investigated. For a 12km length model, representative of longer SPS design such as MR-SPS and SPS-Alpha, an increased total mass of 300,000 tonnes resulted in a response frequency of 4.28×10^{-5} Hz. This response frequency is much more closely aligned to the excitation frequency of the gravity gradient acceleration. For this significantly increased mass (300,000 tonnes) and length (12km) the maximum deformation is approximately 120 metres (i.e. 6% of the SPS diameter). The closer the alignment between the excitation and response frequencies, the larger the amplitude of the orbital varying displacements (i.e. the amplitude of structural vibrations).

Most notably, the effect on the orbital dynamics is small, with variations of the order of 10m in the semi-major axis and 10^{-3} degrees for the argument of pericentre. However the deformation does result in a reduction in the SPS efficiency, measured as the fraction of sunlight that is captured by the helix.

The following design guidance may be drawn:

- The structure of the SPS will need to be assessed and designed to accommodate all construction and operating loads, including constant and orbital varying loads.
- As a matter of good engineering practice, the modal frequencies of the SPS should be determined at all stages of the structural design process and compared with first and second order orbital frequencies.
- For extremes of SPS design, deformations due to orbital varying loads may become significant (relative to the SPS size) and should be assessed statically or dynamically.
- For the range of design parameters (mass and length) exhibited by the current leading SPS concepts, interaction between orbital mechanics and structural dynamics is not expected to be an issue.
- Structural vibration may become an issue for SPS performance due to potential misalignment. However, this can easily be assessed using commonly used Finite Element software. For the example of the 12km long SPS, the total SPS mass should not exceed 100,000 tonnes in order to achieve a sunlight capture efficiency of 90%.
- Structural vibration may become an issue for the structural integrity of an SPS. However, this can easily be assessed using commonly used Finite Element software. Structural integrity and misalignment can be assessed simultaneously.
- Formal assessment of satellite vibration on orbital dynamics should be undertaken at key design gates as an ongoing check. It is likely that there will be sufficient stiffness in the design, to mitigate concerns of alignment and structural integrity, thereby ensuring that deformations are relatively small in comparison to the overall size of the satellite.

10 Recommendations

Based on the conclusions of this study, the following recommendations are made for future work to further develop SBSP technology:

- **Investigate the fatigue performance of SPS designs:** It has been identified that structural vibration may become an issue for the structural integrity of large mass SPSs. A study is recommended to quantify component stresses and assess the fatigue performance over the operating life of an SPS. This may be extended to consider the fatigue performance of composites, which are likely to be used in many SPS designs.
- **Orbital Mechanics for a range of SPS concepts:** A study to research and quantify the range of orbital loads on SPS spacecraft in general, and the implications on their stability.
- **Attitude and Orbital Control Systems (AOCS) for other SPS designs:** AOCS considerations are particularly concept specific and the thruster forces that have been considered in this study are specific to CASSIOPeiA. It is recommended that a study is undertaken to consider the variation in the AOCS requirements and potential design solutions for other SPS designs.
- **SPS design development:** From the review of various SPS concepts, it has been identified that most leading concepts currently lack significant design detail. It is recommended that a study is carried out to build on the outputs from this work, focused on how the guidelines are used to develop the more detailed design for the SPS class concepts.
- **Development of an Orbital Dynamics Toolset:** A study to formulate an Orbital Dynamics toolset, which can be used throughout the SPS design process to streamline the perturbation analysis.

11 References

[1] Junkins J L, Schaub H, Analytical Mechanics of Space Systems, Second Edition: Second Edition. American Institute of Aeronautics and Astronautics, 2009, dx.doi.org/10.2514/4.867231.

[2] McNally I J, Orbital and rotational dynamics of solar power satellites in geosynchronous orbits. Ph.D. thesis, University of Glasgow, 2018.

[3] Roithmayr M, Integrated Orbit, Attitude, and Structural Control Systems Design for Space Solar Power Satellites. *Control Systems Design*, p. 137, 2001.

[4] Frazer-Nash, Space based solar power as a contributor to net zero, phase 1: Engineering feasibility report, 51057r. *BEIS*, 2021.

[5] Cash I, Cassiopeia–a new paradigm for space solar power. *Acta Astronautica*, 159, 170–178, 2019.

[6] Vallado D A, McClain W D, Fundamentals of Astrodynamics and Applications. Third edition, Microcosm Press/Springer, 2007.

[7] Beletsky V V, Levin E M, Dynamics of space tether systems. Number 83 in Advances in the astronautical sciences, Published for the American Astronautical Society by Univelt, Inc, 1993.

[8] Wertz J, Spacecraft Attitude Determination and Control (Astrophysics and Space Science Library). First edition, Springer, 1978, libgen.li/file.php?md5=02f6e900a42a194ad4b9afd24711af6d.

[9] Borovsky J E, Denton M H, Magnetic field at geosynchronous orbit during high-speed stream-driven storms: Connections to the solar wind, the plasma sheet, and the outer electron radiation belt. *Journal of Geophysical Research: Space Physics*, 115(A8), 2010, dx.doi.org/10.1029/2009JA015116, _eprint: https://onlinelibrary.wiley.com/doi/pdf/10.1029/2009JA015116.

[10] Oglevie R, Attitude control of large solar power satellites. In *Guidance and Control Conference*, 1978, AIAA PAPER 78-1266.

[11] Rosengren A J, Scheeres D J, McMahon J W, The classical Laplace plane as a stable disposal orbit for geostationary satellites. *Advances in Space Research*, 53(8), 1219–1228, 2014, dx.doi.org/10.1016/j.asr.2014.01.034.

[12] Rosengren A J, Scheeres D J, Laplace plane modifications arising from solar radiation pressure. *The Astrophysical Journal*, 786(1), 45, 2014.

[13] Di Carlo M, Vasile M, Analytical solutions for low-thrust orbit transfers. *Celestial Mechanics and Dynamical Astronomy*, 133(7), 33, 2021, dx.doi.org/10.1007/s10569-021-10033-9.

[14] Bentley J L, Multidimensional binary search trees used for associative searching. *Commun ACM*, 18(9), 509–517, 1975, dx.doi.org/10.1145/361002.361007.

[15] Cefola P, Long A, HOLLOWAY G JR, The long-term prediction of artificial satellite orbits. In *12th Aerospace Sciences Meeting*, p. 170, 1974.

[16] Zuiani F, Vasile M, Extended analytical formulas for the perturbed keplerian motion under a constant control acceleration. *Celestial Mechanics and Dynamical Astronomy*, 121(3), 275–300, 2015, dx.doi.org/10.1007/s10569-014-9600-5.

[17] Nayfeh A H, Perturbation methods. John Wiley & Sons, 2008.

[18] Thomsen J J, Vibrations and stability, volume 2. Springer, 2003.

[19] Thomson W T, Theory of vibration with applications. CrC Press, 2018.

[20] Battin R H, An Introduction to the Mathematics and Methods of Astrodynamics, Revised Edition. American Institute of Aeronautics and Astronautics, 1999, dx.doi.org/10.2514/4.861543.

[21] Broucke R A, Cefola P J, On the equinoctial orbit elements. *Celestial mechanics*, 5(3), 303–310, 1972.

[22] Cash I, Cassiopeia solar power satellite. In *2017 IEEE International Conference on Wireless for Space and Extreme Environments (WiSEE)*, pp. 144–149, IEEE, 2017.

[23] Gebhart B, Heat transfer. Second edition, McGraw-Hill, 1971.

[24] Lauzier N, View factors. https://www.mathworks.com/matlabcentral/fileexchange/5664-view-factors, MATLAB Central File Exchange, 2022, [Online; accessed December 5, 2022].

[25] Sparrow E M, A New and Simpler Formulation for Radiative Angle Factors. *Journal of Heat Transfer*, 85(2), 81–87, 1963, dx.doi.org/10.1115/1.3686058.

[26] Dupond, Dupont™ kapton® hn. https://www.dupont.com/content/dam/dupont/amer/us/en/products/ei-transformation/documents/DEC-Kapton-HN-datasheet.pdf, 2022, "[Online; accessed December 5, 2022]".

A Definitions

All variables are defined the first time they appear throughout this report. However, to make comprehension easier, some commonly used guidelines are followed in the typesetting of this document. Firstly, scalar quantities are in normal text, while vectors are in bold. If a vector is termed $\mathbf{r}$, then $r = ||\mathbf{r}||$ will be its magnitude, and $\hat{\mathbf{r}} = \mathbf{r}/r$ will be its normalized version. The x component of vector $\mathbf{r}$ will be represented with a superscript r^x, to avoid cluttering with subscripts. Its projection onto the xy plane is written as $\mathbf{r}^{xy}$. We follow the convention that $\dot{L}$ represents the time derivative of L. The astronomical symbols for the Earth $\oplus$ and for the Sun $\odot$ will also be used in subscripts throughout the work. The reference frames and coordinate systems used, as well as other definitions used throughout this report are outlined in this appendix.

A.1 SPS's Body Frame

The reference frame of the SPS, also referred to as its body frame, is aligned with with principal axis of inertia. Its X axis points towards where the Sun should be during nominal conditions, and the Z axis is coincident with the axis of the helix. The Y axis is then chosen to complete the triad. Figure A.1 shows this reference frame.

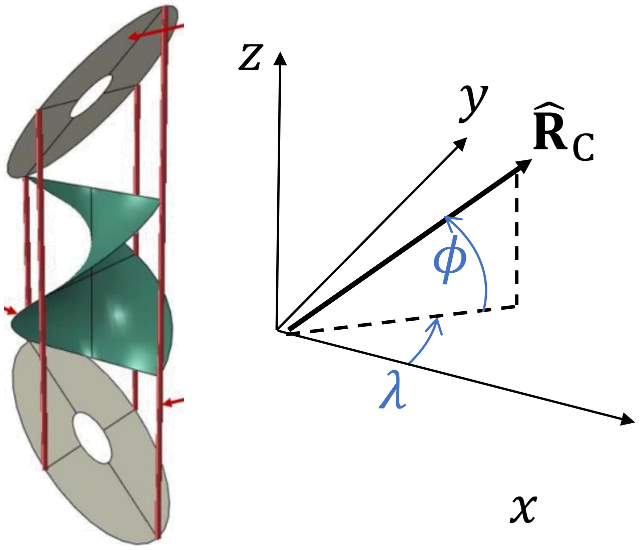

Figure A.1: Frame of the SPS with angles ϕ and λ represented. During nominal operations, the x axis points towards the Sun.

A.2 Pseudo-Inertial Reference Frames

To represent the position of objects in orbit in a pseudo-inertial reference frame, we use an Earth Centered Inertial (ECI) reference frame. This frame and the others referred to in this discussion are termed pseudo-inertial because their centre of mass is subject to acceleration, making them technically non-inertial, but this acceleration is deemed negligible [6]. Given the importance of the Earth-Sun vector in our problem, it is convenient to use as reference plane called the ecliptic plane, the plane containing the orbit of the Earth around the Sun, instead of the equatorial frame. As such, in our ECI frame, the X axis still points towards the Vernal equinox or first point of Aries [6], but the Z axis is orthogonal to the ecliptic plane. The X axis is also along the intersection of the ecliptic and equinoctial frames.

Henceforth, we will refer to this reference frame as the ecliptic frame. Another useful reference frame is the Sun frame. It also has the Z axis orthogonal to the ecliptic plane, but the X axis points towards the Sun. Figure A.2 illustrates both of these reference frames. The ecliptic frame is defined by the axes XYZ while the Sun frame is defined by $X_\odot Y_\odot Z$. These two frames differ by a rotation around the Z axis of $L_\odot$, which is the angle from the vernal equinox to the Earth-Sun vector.

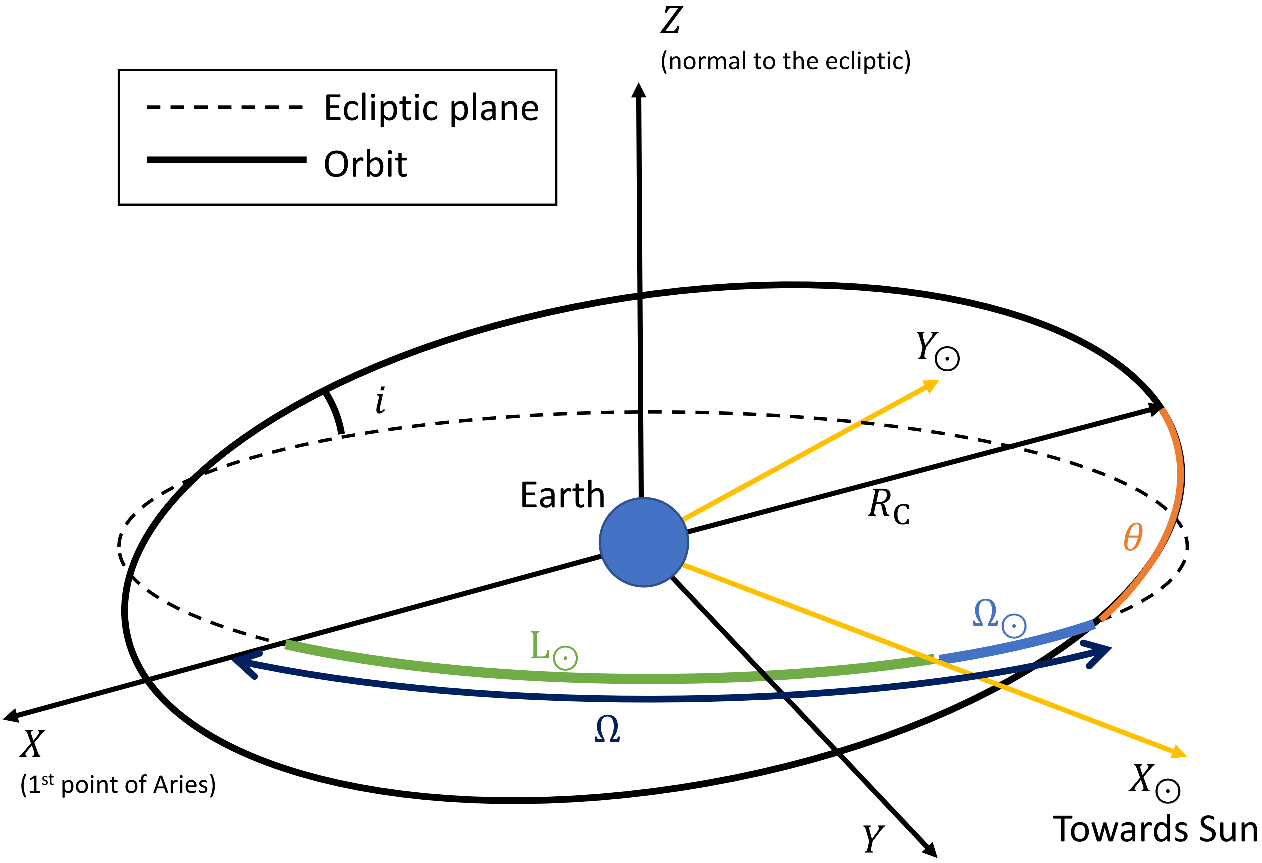

Figure A.2: Illustration of reference frames. The ecliptic frame is formed by the XYZ axes while the Sun frame is formed by the $X_\odot Y_\odot Z$ axes.

A.3 The Radial-Transverse-Normal (RTN) Frame

This frame is defined for an object in orbit, its origin coinciding with the latter's center of mass, $\mathbf{R}_C$. The X axis is along the radial direction (i.e. the vector connecting Earth's centre of mass to $\mathbf{R}_C$), the Z axis is along the orbital angular momentum vector, and y is in the transversal direction (along velocity for a circular orbit), completing the triad. This frame is used to write the acceleration in Gauss's Variation of Parameter (VoP) Equations.

A.4 Element sets

The position of the SPS along its orbit $\mathbf{R}_C$ will be written in the ecliptic frame, unless noted otherwise. This, together with its velocity vector $\dot{\mathbf{R}}_C$, fully defines the spacecraft's state in its orbit, and forms the Cartesian elements.

A commonly used element set are the Keplerian elements $(a, e, i, \Omega, \omega, \nu)$, which are respectively the semi-major axis, eccentricity, inclination, Right Ascension of the Ascending Node (RAAN), Argument of Pericenter (AP) and true anomaly. The inclination i and RAAN Ω are defined with respect to the ecliptic plane as shown in Fig. A.2. This means that for an equatorial orbit, $i = \epsilon \neq 0$, where ϵ is the obliquity of the ecliptic [6], i.e., the angle between the ecliptic and the equatorial plane, which is approximately $23.4°$.

When the Sun frame is used, the RAAN is represented as $\Omega_\odot$ instead of Ω, also represented in the same figure. We also use the argument of latitude $\theta = \omega + \nu$, also shown in Fig. A.2. Finally, the mean motion is also a useful value, which is the average variation of any of the fast variables above

$$n = \sqrt{\frac{\mu}{a^3}} \tag{A.1}$$

This element set has many singularities, for example for circular orbits ω and ν are not defined, while for ecliptic orbits Ω is not defined. An element set which has almost no singularities are the equinoctial elements [20].

$$\begin{aligned}
a &= a \\
P_1 &= e \sin(\omega + \Omega) \\
P_2 &= e \cos(\omega + \Omega) \\
Q_1 &= \tan\frac{i}{2} \sin\Omega \\
Q_2 &= \tan\frac{i}{2} \cos\Omega \\
L &= \Omega + \omega + \nu = \Omega + \theta
\end{aligned} \tag{A.2}$$

When the Sun frame is used instead of the ecliptic frame, Ω is replaced by $\Omega_\odot$ and the subscript $\odot$ is added to all variables except a which does not change.

In the study of the dynamics of high area-to-mass ratio satellites, Rosengren et al. [11, 12] have used Milankovitch orbital elements, which are defined as the scaled angular momentum vector $\tilde{\mathbf{h}}$ and eccentricity vector $\mathbf{e}$, defined as:

$$\begin{aligned}
\tilde{\mathbf{h}} &= \frac{1}{\sqrt{\mu a}} \mathbf{R}_C \times \dot{\mathbf{R}}_C \\
\mathbf{e} &= \frac{1}{\mu} \dot{\mathbf{R}}_C \times \mathbf{h} - \frac{\mathbf{R}_C}{R_C} ,
\end{aligned} \tag{A.3}$$

where $\mathbf{h} = \mathbf{R}_C \times \dot{\mathbf{R}}_C$ is the angular momentum vector. Vector $\tilde{\mathbf{h}}$ is scaled such that $\tilde{h} = \sqrt{1 - e^2}$. These elements are composed only of slow elements, and are over-determined since $\tilde{\mathbf{h}} \cdot \mathbf{e} = 0$ and $\tilde{\mathbf{h}} \cdot \tilde{\mathbf{h}} + \mathbf{e} \cdot \mathbf{e} = 1$, meaning they represent a system with 4 degrees of freedom. They do not capture the semi-major axis or the fast variable, which explains this.

The Variation of Parameters (VoP) equations give the time derivatives of these parameters as a function of some perturbation. For each set of elements mentioned in this Section (apart from Cartesian) there are Lagrange and Gauss VoP equations. We will only make use of Gauss VoP equations for the Equinoctial elements, in particular, the derivatives of the slow elements over L, neglecting the effect that the perturbations have on the variation of L [16]:

$$\begin{aligned}
\frac{\mathrm{d}a}{\mathrm{d}L} &= \frac{2a^3B^2}{\mu}\left[\frac{(P_2\sin L - P_1\cos L)}{\Phi^2(L)}a_R + \frac{1}{\Phi(L)}a_T\right] \\
\frac{dP_1}{dL} &= \frac{B^4a^2}{\mu}\Bigg[\Bigg(-\frac{\cos L}{\Phi^2(L)}a_R + \left(\frac{P_1+\sin L}{\Phi^3(L)} + \frac{\sin L}{\Phi^2(L)}\right)a_T\Bigg) \\
&\quad -P_2\frac{Q_1\cos L - Q_2\sin L}{\Phi^3(L)}a_N\Bigg] \\
&\quad +P_1\frac{Q_1\cos L - Q_2\sin L}{\Phi^3(L)}a_N\Bigg] \\
\frac{dQ_1}{dL} &= \frac{B^4a^2}{\mu}\Bigg[\Bigg(\frac{\sin L}{\Phi^2(L)}a_R + \left(\frac{P_2+\cos L}{\Phi^3(L)} + \frac{\cos L}{\Phi^2(L)}\right)a_T\Bigg) \\
\frac{dQ_2}{dL} &= \frac{B^4a^2}{2\mu}\left(1+Q_1^2+Q_2^2\right)\frac{\sin L}{\Phi^3(L)}a_N\ .
\end{aligned} \tag{A.4}$$

A.4.1 Equinoctial Reference Frame

To study the variations of the equinoctial elements, it is often useful to write accelerations in the Equinoctial frame [15]. The X,Y, and Z directions of this frame, termed $\mathbf{f}$, $\mathbf{g}$ and $\mathbf{h}$, are the columns of the following orthogonal matrix [21]:

$$R = \frac{1}{1+Q_1^2+Q_2^2}\begin{bmatrix} 1-Q_1^2+Q_2^2 & 2Q_1Q_2 & 2Q_1 \\ 2Q_1Q_2 & 1+Q_1^2-Q_2^2 & -2Q_2 \\ -2Q_1 & 2Q_2 & 1-Q_1^2-Q_2^2 \end{bmatrix} \tag{A.5}$$

In this reference frame, the position of the spacecraft can be written as $\mathbf{R}_C = R_C\left(\cos L\hat{\mathbf{f}} + \sin L\hat{\mathbf{g}}\right)$, and the angular momentum vector has direction $\mathbf{h}$.

A.5 Orbits

Throughout this report, the SPS is considered to be in a Geosynchronous Orbit (GSO). This is an orbit with a period equal to one sidereal day, which results in a repeating groundtrack that stays near some point on the Earth's surface. A sidereal day, approximately 23.93 hours, differs from the solar day, 24 hours. The sidereal day is the rotation period as measured with respect to the stars, while the solar day is measured with respect to the Sun. The orbital period must match the sidereal period for a satellite to be geosynchronous.

Under Keplerian motion, the orbital period T relates to the semi-major axis by:

$$T = 2\pi\sqrt{\frac{a^3}{\mu_\oplus}} \tag{A.6}$$

resulting in a semi-major axis a of approximately 42164 km.

When a GSO has the satellite constantly above a fixed point on the Earth's surface, it is called a Geostationary Equatorial Orbit (GEO), as achieving this requires an equatorial orbit, and the fixed point on the Earth's surface must also be on the equator.

Another useful type of GSO is the Geosynchronous Laplace Plane Orbit (GLPO) [12]. While in Keplerian dynamics, the orbital elements defined above would stay constant, in the presence of perturbations they will vary, causing the orbital plane to vary, which could be detrimental to the mission objectives. The GLPO is a GSO whose orbit is on the Laplace plane, defined as the plane for which the effect of the perturbation is minimal. The GLPO is therefore an example of a frozen orbit.

In this work we have considered the SPS to be placed in a GEO orbit, although some results are also obtained for GLPO. A GEO orbit has the desirable property of allowing a satellite to constantly beam power to a ground station with a constant beam elevation from the ground station. A disadvantage is the high orbital maintenance costs, which are reduced for the GLPO. These topics are discussed in depth in Sections 4.3 and 4.4. The thesis by McNally [2] goes into further detail on both of these orbits and the advantages and disadvantages of placing an SPS on them.

B Optimized Attitude Control by Relaxation of the Z Axis Constraint

In Ian Cash's papers [22, 5], it is implied that the SPS will have its Z axis perpendicular to the ecliptic plane, while it rotates once per year around this axis so that the reflectors, oriented along the X axis, are always pointing towards the Sun.

We kept this assumption throughout our work, as it simplifies our methodology. However, the only important constraint is that the X axis keeps pointing towards the Sun, while the elevation angle for the microwave beam never exceeds its upper limit. We can imagine, therefore, the SPS rotating in an oscillatory manner about this X axis throughout an orbit, while this X axis keeps pointing towards the Sun. This introduces a degree of freedom to our system, the angle δ about the X axis, with $\delta = 0$ corresponding to the Z axis normal to the ecliptic plane as assumed.

As part of our work we did a preliminary investigation into the optimal $\delta(t)$ and to the amount of propellant saved by optimizing it. We wish to optimize the propellant cost, which is equivalent to minimizing:

$$\min_{\delta(\theta)} \int_{\theta=0}^{2\pi} \left| I_{xx}\ddot{\delta}(\theta) - M_{gg}^{x}(\delta,\theta) \right| + \left| M_{gg}^{y}(\delta,\theta) \right| \mathrm{d}\theta \tag{B.1}$$

where θ is the argument of latitude, used in lieu of time (circular orbit), and the formula for the gravity gradient torque for a rotated SPS, $\mathbf{M}_{gg}(\delta,\theta)$, was obtained using Wolfram Mathematica. Furthermore, this optimization assumes a purely Keplerian GEO equatorial circular orbit, as a preliminary study. Future work could look into removing these approximations.

For convergence purposes, the smooth version of the previous nonlinear program is solved first, its solution being used as a starting point to the actual non-smooth problem:

$$\min_{\delta(t)} \int_{\theta=0}^{2\pi} \left(I_{xx}\ddot{\delta}(\theta) - M_{gg}^{x}(\delta,\theta) \right)^2 + \left(M_{gg}^{y}(\delta,\theta) \right)^2 \mathrm{d}\theta \tag{B.2}$$

the problem is transcribed using a finite elements approach, where $\ddot{\delta}(\theta)$ is approximated with a second order central finite difference, and it is assumed that δ is periodic, i.e. $\delta(\theta) = \delta(\theta + 2\pi)$. The optimization is done for a single orbit without considering the relatively slow precession of the X axis. This analysis is repeated for all days of the year, choosing the mean position of the Sun relative to Earth as the direction of the X axis of the SPS.

To ensure all quantities are well scaled, they are all written in distance/time/mass units (DU/TU/MU) chosen such that

$$a = 1\ \mathrm{DU} \tag{B.3}$$

$$\mu = 1\ \mathrm{DU}^3/\mathrm{TU}^2 \tag{B.4}$$

$$I_{xx} = 1\ \mathrm{MU}\cdot\mathrm{DU}^2 \tag{B.5}$$

MATLAB's *fminunc* is used to carry out the numeric optimization with the *quasi-newton* algorithm.

Figure B.1 shows the result of joining the optimized δ for each day of the year into a single curve. The detail in Fig. B.1b shows the orbital variation of δ, showing that it oscillates twice per orbit (once every 12 (sidereal) hours). Figure B.2 shows the propellant cost per day throughout the year. The equinoxes correspond to zero propellant cost times, because during the equinoxes the SPS can keep its Z axis normal to the orbital plane while continuously having its X axis pointing towards the Sun. This is because these are the only times when the Sun is in the orbital plane from the perspective of the SPS, and because for CASSIOPEIA $I_{xx} = I_{yy}$, which means this orientation is an equilibrium, albeit an unstable one as discussed previously.

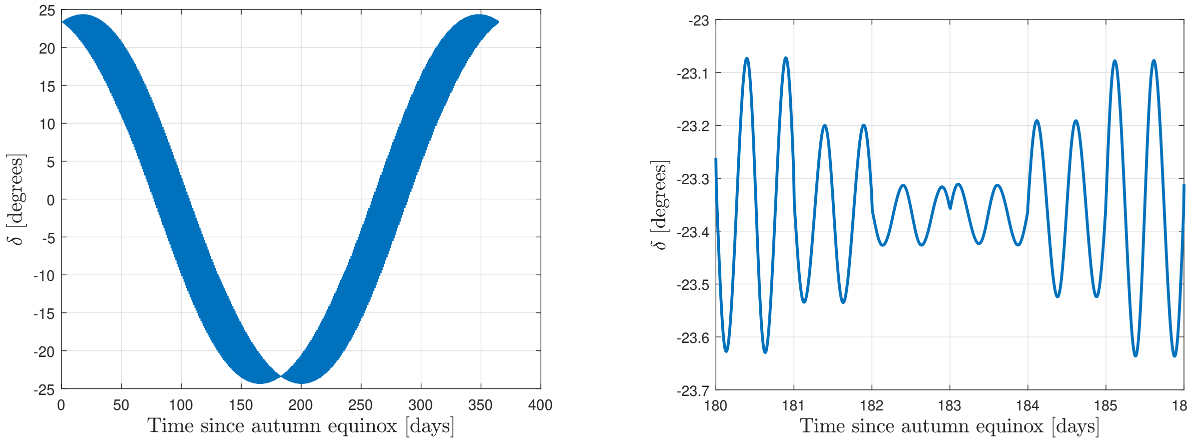

a: Entire year

b: Detail around spring equinox

Figure B.1: Oscillation of angle δ obtained from optimising Eq. (B.1)

A cursory examination of these results suggests the rotation of the SPS always puts the Z axis closer to the normal to the orbital plane, and as such it does not seem to negatively affect the requirement on the maximum elevation angle of the microwave beam. Furthermore, numerical integration of the curves in Fig. B.2 gives a 61% reduction in propellant costs from this optimization.

However, because now the torque produced by the thrusters also depends on $\ddot{\delta}$, the spherical harmonics model we have been using would no longer be apt, and a different approach would be required to handle this situation.

As a final note, the simplicity of the curves in Fig. B.1 suggests that an analytical expression is possible, and as such, it could be the subject of further work.

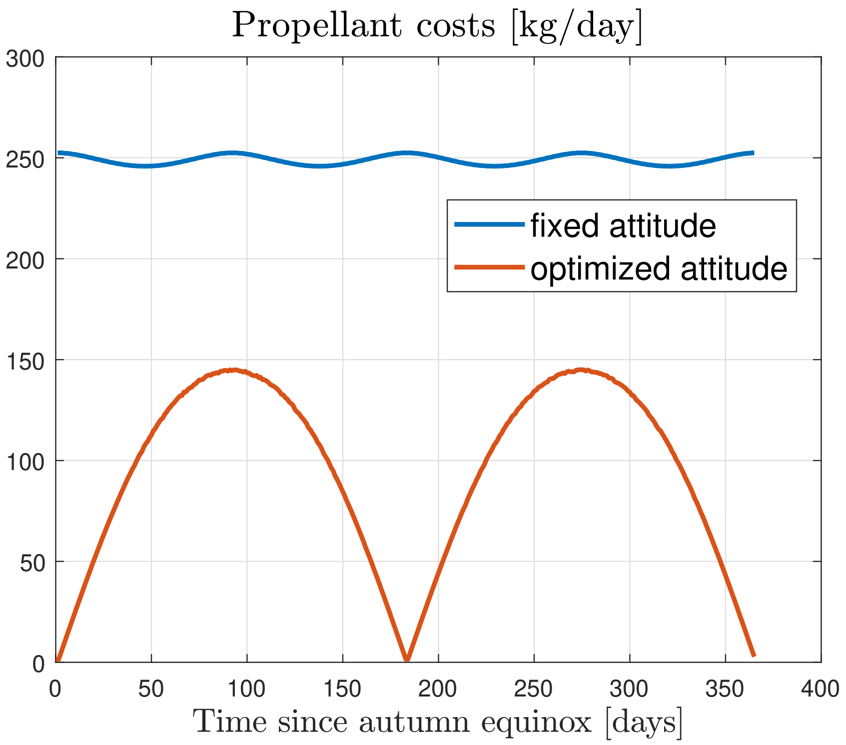

Figure B.2: Propellant cost for keeping fixed attitude versus optimized.

C Thermal Analysis

A brief and preliminary thermal analysis of the SPS was also conducted. Given the lack of information yet provided on the thermal characteristics, a number of assumptions had to be made:

- All heat transfers are radiative, thermal conduction was not considered;
- The spacing between the layers was assumed to be similar to the length of the antennas, which is a function of the wavelength of the microwave beam. This results in a spacing of $0.033m$;
- The helix is 2km long, which results in $N = 60606$ layers;
- Each layer only has direct thermal contact with the adjacent ones. Correctly modelling the fact that some radiation may also hit other layers would require handling occlusions, which would require ray tracing, and thus a lot more effort;
- All radiative energy that is not absorbed is reflected (i.e., none is transmitted through the material);
- All radiative emission and reflection is purely diffuse (i.e. follows Lambert's law);
- The effect of the Earthshine and Earth's IR radiation is negligible. Its incident power is of the order of 15W/m^2 at GEO, whereas Sunlight is around 1367W/m^2;
- Microwave power is half the received Solar power, and has a refrigerative effect [5]
- Like in [5], the solar light incident directly on the helix is considered negligible compared to that coming from the reflectors.

The layers are uniformly distributed along the length of the helix, and the angle between each of them is chosen as $\theta = 180°/N$, so as to form a helix shape. The width of each layer is then chosen to prevent gaps while minimizing occlusions, resulting in $w = \frac{L}{2}\sin\theta$. The geometry of the layers is also visually described in Fig. C.1. Due to occlusions, the top layer receives twice as much sunlight from the top reflector as all other layers, as implied by the illustration in Fig. C.1b, and confirmed by polygon subtraction algorithms. The same argument can be made about the bottom layer and the bottom reflector. The microwave power is assumed to remove heat from each layer equally. Therefore, each layer in the middle receives $P_{\odot}A/2$ from each reflector, and emits in microwaves approximately $P_{\odot}A/2$, i.e. half the total incident power, for a net received power of $P_{\odot}A/2$. The top and bottom layers, receiving an additional $P_{\odot}A/2$ due to the non-occluded area, therefore receive twice the amount of power as the other layers.

The radiative analysis was done by solving the equivalent radiative network. This process is briefly summarized here, but more information can be found in [23]. First, the view factor F_{12}, also known as angle factor [23], between adjacent layers is computed using the code in [24]. This code makes use of the formula introduced in [25], where the 4 dimensional integral is turned into a 2 dimensional contour integral by the repeated application of Stokes' theorem. From here, the Gebhart factors [23] are computed, and the radiative network is constructed. Each element emits an amount of radiative power following a grey body law, i.e. $\epsilon\sigma AT^4$, where ϵ is its emissivity for its temperature, and σ is the Stefan–Boltzmann constant. The emissivity at infra-red ϵ_{IR}, and the solar absorptivity $\alpha_{\odot}$ are properties of the coating on the structure. We do not at present have this information, so a small parameter study was done on these parameters, where they were each considered to be 0.99 or 0.5.

The amount of absorbed solar power by each layer is given by $\alpha_{\odot}AP_{\odot}$, where $P_{\odot} = 1367\mathrm{W/m^2}$. As mentioned in Section 3.5, the radiative power impinging on the SPS resulting from radiation emitted by the Earth is around 1% (15 $\mathrm{W/m^2}$) of that from direct Solar radiation for geostationary orbit, and as such, radiation coming from the Earth was

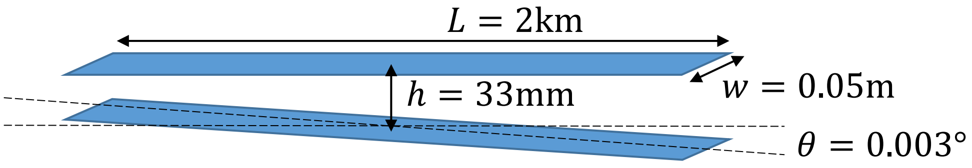

a: Two adjacent layers seen from the side

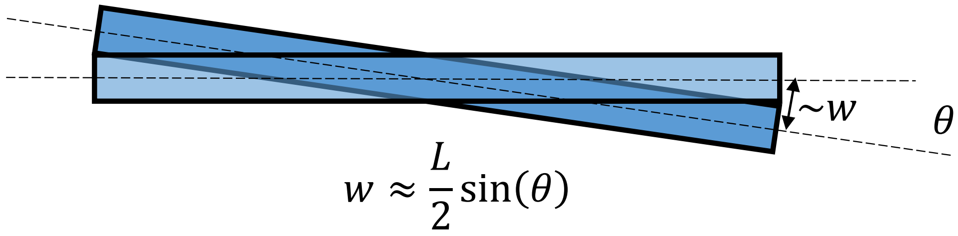

b: Two adjacent layers seen from the top

Figure C.1: Geometry of the layers that compose the SPS (not to scale).

not considered in this analysis.

The view factor F_{12} indicates what fraction of the radiation emitted by object 1 directly hits object 2. The Gebhart factor B_{12} indicates what fraction of the radiation emitted by object 1 eventually hits object 2 after a potentially infinite number of reflections. Both of these values assume purely diffuse emission and reflection, and that all objects are completely opaque. The Gebhart factors are thus defined by the solution of [23]:

$$B_{ij} = \epsilon_j F_{ij} + \sum_k (1 - \epsilon_k) F_{ik} B_{kj} \tag{C.1}$$

The view factors were found to be $F_{i,i+1} = F_{i+1,i} \approx 0.2$. Element $N + 1$ represents the vacuum, and all radiation that does not hit another layer goes into the vacuum, resulting in $F_{i,N+1} = 0.6$. All other terms of F_{ij} are zero, making it a very sparse matrix. The real solution to Eq. (C.1) results in a full matrix B_{ij}, however most of these factors are very close to zero. A finite number of reflections can be considered by first setting B_{ij} to all zeros, followed by iteratively replacing it by the right hand side of Eq. (C.1). This leads to a sparse matrix as well. We consider 5 reflections, which leads to a maximum absolute error of around 5×10^{-6}.

A radiative network is solved by constructing an analogous electrical circuit, where thermal phenomena are represented by electrical counterparts. The voltages at each node i correspond to σT_i^4, and each pair of nodes is linked by a resistor with conductance (i.e. the inverse of the resistance) given by $\epsilon_i A_i B_{ij} = \epsilon_i A_i B_{ji}$. The electrical ground represents the vacuum, which is modelled as being at absolute zero (as opposed to the true value of 3K). The incident solar power is represented by current sources linking the ground to each node. The radiative network is then solved using the same methods used to solve electric networks, which gives the power at each layer. The results are shown in Fig. C.2. The temperature is almost constant, and would be almost completely constant if each layer was receiving the same amount of solar power. However, as mentioned, the top and bottom layers receive more solar power, which leads to a very short but intense gradient near both ends of the helix. As a consequence, the fist and last panels are almost 50 degrees Celcius hotter than those in the middle.

Looking up the material properties of Kapton film [26], which is the main component of the helix, we get that its thermal expansion coefficient is 20ppm. With the temperature gradient found above, this would lead to the top and bottom panels expanding to become 2 meters longer than those in the middle. This value is in the order of magnitude of the distortions found in the static analysis. However, given that the solar incidence is constant for this design, this deformation would also be constant throughout the orbit, and thus would not lead to a perturbation on the orbit. The Earthshine and microwave beam would vary, however, introducing a temporally variant thermal effect, but one that is smaller in magnitude. Furthermore, given the typical slowness of thermal phenomena in space, it can be expected that the effect of Earthshine would average out for a particular orbit, and we would not have a periodically varying deformation coming from this effect, thus limiting its effect on the orbit parameters further.

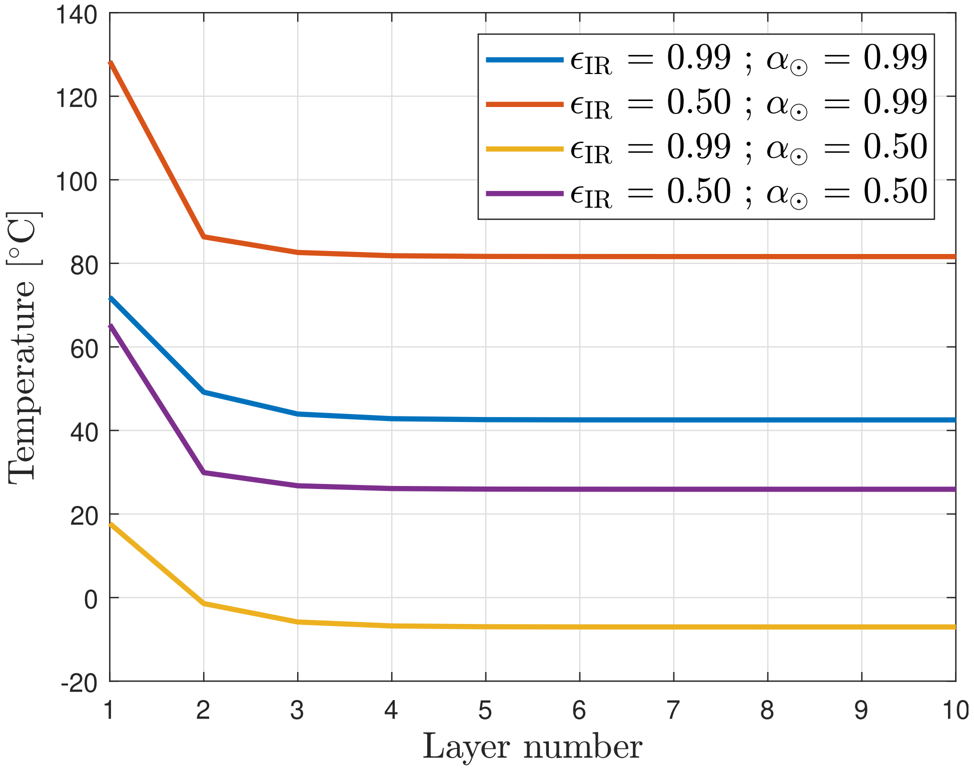

Figure C.2: Temperature as a function of layer number around the first layers. The remaining layers were at almost constant temperature.

FRAZER-NASH
CONSULTANCY
A KBR COMPANY

University of
Strathclyde
Glasgow

Hill Park South
Leatherhead, Surrey
KT22 7LH

Tel: 0333 032 9500

fnc.co.uk

Offices at:
Basingstoke, Bristol, Burton-on-Trent, Dorchester,
Dorking, Glasgow, Gloucester, Middlesbrough,
Plymouth and Warrington